UNIVERSITÀ DI PARMA

UNIVERSITÀ DEGLI STUDI DI PARMA

DOTTORATO DI RICERCA IN

"Ingegneria Industriale"

CICLO XXXV

DESIGN, PRODUCTION AND QUALIFICATION OF STRUCTURAL COMPONENTS FABRICATED BY METAL ADDITIVE MANUFACTURING: A CASE STUDY

Coordinatore:
Chiar.mo Prof. Gianni Royer Carfagni

Tutore:
Chiar.mo Prof. Gianni Nicoletto

Dottorando: Federico Uriati

Anni Accademici 2019/2020 – 2021/2022

Preface

This thesis marks the end of my Ph.D. in Industrial Engineering at the University of Parma, which began in November 2020 and ended in January 2022, with a 3-month extension due to the COVID-19 pandemic.

My research focused on the characterization of the mechanical properties of metal fabricated by additive manufacturing, particularly laser powder bed fusion (L-PBF). The activity during these years was oriented toward understanding the effect of the process on the fatigue properties of materials produced with this technology and how to implement this technology's potential in designing and producing structural components for high-performance applications. During my studies, I investigated the properties of different materials produced by L-PBF, including Inconel718, Ti6242, Al2024 and AlSi10Mg and published several scientific contributions.

I had the opportunity to spend three months at the European Space Agency (ESA) at ESTEC in the Netherlands, where I continued my research at their facilities on the characterization of IN718 manufactured by L-PBF. This experience allowed me to gain valuable insights into the potential of additive manufacturing for use in space applications.

In addition to my academic research, I also had the opportunity to collaborate with the company Beam IT, which provided samples for my studies and offered an industrial perspective on my work. This collaboration helped to give my research a practical, real-world focus and allowed me to apply my findings to the design of components for use in the industry.

The overall goal of the activity presented in this thesis is the know-how integration needed for the development of safety-critical structural parts fabricated by L-PBF and its practical validation. I explored the different aspects to consider when dealing with metal additive manufacturing, like methods and tools for the design, fabrication and testing of parts and how to apply them to a significant case study identified in the automotive sector. The present work presents a workflow to design, produce and qualify a structural component produced by L-PBF, going through the different phases that need to be considered and discussing the various stages of realization that lead to the production of actual parts and their testing.

Abstract

Additive manufacturing (AM) is an innovative and game-changing technology that, thanks to freedom that guarantees in the design of the parts, help in obtaining lightweight structure that, when applied to the automotive application, would help improve performance and reduce fuel consumption and carbon emissions. This work focused on thoroughly understanding the design, development, and qualification process for a fatigue-critical component made of L-PBF metal alloy for use in the automotive industry. In addition, the research examined how various factors, such as part geometry, loading conditions, L-PBF process parameters, post-processing, and surface roughness, impact the finished component's material properties and mechanical properties.

The main goals of this study are to outline an integrated approach for the design of metal additive manufacturing parts. Including topological optimization of the geometry, simulation of the AM process, fabrication of the components using an industrial-grade L-PBF system and AlSi10Mg alloy powder, and evaluation of the structural integrity through fatigue testing under realistic conditions. The project's goal was to establish a comprehensive workflow for creating and evaluating fatigue-critical L-PBF metal components, guiding future research efforts in AM, and aligning with current industry requirements and standards.

Acknowledgment

Completing a Ph.D. is a challenging and exceptional personal and professional growth experience. Many people have helped me during this journey by providing support throughout the years.

Above all, I want to express my gratitude to my supervisor, Prof. Gianni Nicoletto, for the continuous support and guidance throughout my Ph.D. journey. Your availability for discussions and suggestions has been invaluable, and your kind and positive attitude has been a constant source of motivation.

Thanks to Prof. Enrica Riva for the kindness and help with the needs of research activities.

Essential support was provided by Marco and Giovanni that I want to acknowledge for their assistance and help during lab activities.

Recognizing the importance of their role, I would like to express my gratitude to Beamit for providing the materials and samples necessary for my research.

I was privileged to gain a valuable experience at the European Space Agency that I want to thanks for opening their door and allowing me to learn from top-level professionals.

Numerous individuals have played a crucial role in the success of this project, and I am deeply grateful for their contributions.

All of this would not be possible without my family and friends' support, which, with their constant encouragement and trust in me, have been the primary driving forces throughout these years.

List of scientific contributions

i) **A comparison of Inconel 718 obtained with three L-PBF production systems in terms of process parameters, as-built surface quality, and fatigue performance** Uriati, Nicoletto - 2022 –International Journal of Fatigue Volume 162, September 2022 - https://doi.org/10.1016/j.ijfatigue.2022.107004

ii) **As-built surface quality and fatigue resistance of Inconel 718 obtained by additive manufacturing** Uriati F, Nicoletto G, Lutey AHA. *Mat Design Process Comm*. 2021; https://doi.org/10.1002/mdp2.228

iii) **FE Modelling of the Fatigue Behavior of L-PBF Inconel 718 with As-Built Surfaces –** Federico Uriati; Gianni Nicoletto; Radomila Konečná- 2022 https://doi.org/10.1007/978-3-030-91847-7_12

iv) **Influence of surface orientation on fatigue performance of as-built additively manufactured Inconel718 -** Uriati; Nicoletto; Riva; Varmus; Konečná – 2022 https://doi.org/10.24840/2795-5168_001-001_0007

v) **Design, production, and fatigue testing of an optimized structural component made of L-PBF AlSi10Mg** - Uriati, Zambrelli, Nicoletto, Garibaldi, Procedia Structural Integrity,2021, https://doi.org/10.1016/j.prostr.2021.12.027

vi) **Fatigue Behavior of As-Built L-PBF Inconel 718 and Surface Roughness-Based Modeling** - Nicoletto, Uriati - 2022 - Fatigue and Fracture of Materials and Structures. Structural Integrity, vol 24. Springer - https://doi.org/10.1007/978-3-030-97822-8_39

vii) **Lightweight Design and Additive Manufacturing of a Fatigue-Critical Automotive Component -** Nicoletto, Riva, Uriati – 2022 http://dx.doi.org/10.4271/2022-37-0026

viii) **Surface quality and fatigue behavior of L-PBF AlSi10Mg in as-built condition -** Konečná, Uriati, Nicoletto, Varmus-, Procedia Structural Integrity, 2021; http://dx.doi.org/10.1016/j.prostr.2021.12.020

ix) **Microstructure and Fatigue, Properties of Al2024-RAM2 Aluminum Alloy, Obtained by Laser Powder Bed Fusion -** Varmus, Konecna, Nicoletto, Uriati - Procedia Structural Integrity https://doi.org/10.1016/j.prostr.2022.12.256

x)

List of oral presentations

i) **Surface characteristics and fatigue resistance of Inconel 718 realized by additive manufacturing**
F.Uriati, G. Nicoletto, A.H.A. Lutey , E. Riva
49° Convegno Nazionale AIAS

ii) **FE modelling the fatigue behavior of L-PBF Inconel 718 with as-built surfaces**
F.Uriati, G. Nicoletto, R. Konečná
Virtual Conference On Mechanical Fatigue University of Porto (FEUP, Portugal)

iii) **Correlation between fatigue behavior and surface roughness of Inconel718 produced by additive manufacturing**
Uriati, G. Nicoletto
International conference East Europe Conference on AM materials (EECAM21)

iv) **Design, production, and fatigue testing of an optimized structural component made of L-PBF AlSi10Mg**
F. Uriati, L. Zambrelli, G. Nicoletto, M. Garibaldi
ESIAM21 - The second European Conference on the Structural Integrity of Additively Manufactured Materials

v) **FE modeling of as-built surface effect on fatigue performance of L-PBF Inconel718**
F.Uriati, G. Nicoletto
50° Convegno Nazionale AIAS

vi) **A comparison of Inconel 718 obtained with three L-PBF production systems in terms of process parameters, as-built surface quality, and fatigue performance**
F.Uriati, G. Nicoletto, M.Riccio
ASTM International Conference on Additive Manufacturing (ASTM ICAM 2021)

vii) **Influence of fabrication equipment on surface quality, mechanical properties, and fatigue performance of L-PBF Inconel 718**
F.Uriati. G.Nicoletto, L.Trombi
1st International Conference on Engineering Manufacture (EM2022)

viii) **Fatigue properties and microstructure of alloy A2024-RAM2 obtained by laser powder bed fusion for motorsport application**
F. Uriati, G. Nicoletto, T. Varmus, R. Konecna
51° Convegno Nazionale AIAS

ix) **Directional fatigue behavior of DED Inconel 625 determined via specimen miniaturization**

G.Nicoletto, F. Uriati, A. de Jesus, F. K. Fiorentin
51° Convegno Nazionale AIAS

x) **Microstructure and fatigue properties of A2024-RAM2 aluminum alloy obtained by laser powder bed fusion**
T. Varmus, F. Uriati, G. Nicoletto, R. Konecna
Materials Structure & Micromechanics of Fracture 10 (MSMF10)

xi) **The link between surface quality and fatigue properties of IN718 produced by laser powder bed fusion according to different testing configurations**
F.Uriati, G. Nicoletto, M. Meisnar
3rd International Workshop on Reliability and Design of Additively Manufactured Materials

Contents

Preface 3

Abstract 5

Acknowledgment 7

List of scientific contributions 9

List of oral presentations 11

Contents 13

Introduction 17

1 Background 19

1.1 Additive Manufacturing 21

1.2 Laser powder Bed Fusion (L-PBF) 23

1.3 Industrial applications of L-PBF 25

1.4 The L-PBF technology 27

1.4.1 AM Fabrication Systems 29

1.4.2 Process parameters 30

1.4.3 Post-processing 31

1.4.4 Materials 32

1.5 Technology-dependent factors affecting L-PBF parts 33

1.5.1 Surface morphology 34

1.5.2 Material microstructure 35

1.5.3 Defects distribution 36

1.5.4 Residual stresses 37

1.6 Static properties of L-PBF metals 38

1.7 Fatigue on L-PBF metals 39

2 Methods 45

2.1 Design, Production and Testing of an AM Component 47

2.2 Technological partner 49
2.3 Component selection for case study 50
2.4 Material selection 51
2.5 Re-Design and Optimization 52
2.6 •AM Production 56
2.6.1 Job preparation 56
2.6.2 AM Process simulation 57
2.6.3 Fabrication and post processing 59
2.7 Qualification 61
2.7.1 Components testing 61
2.7.2 Design and Development 63
2.7.3 Miniature samples 64
2.7.4 Hardness and roughness measurement 67
3 Design, production, and testing - Results 69
3.1 Structural optimization 71
3.1.1 Topology optimization 71
3.1.2 Remodeling 74
3.2 L-PBF Fabrication 75
3.2.1 Job preparation 75
3.2.2 Job Fabrication 78
3.2.3 Process simulation software calibration 81
3.3 Experimental results 82
3.3.1 Optimized L-PBF AlSi10Mg control arms 83
3.3.2 Residual stresses in the components 95
3.3.3 Miniature L-PBF AlSi10Mg specimens 99
3.4 Integrated workflow used to develop the fatigue design methodology of an L-PBF AlSi10Mg part 107

4 Fatigue design of L-PBF AlSi10Mg parts 111
4.1 Fatigue design approach 113
4.2 Integrated workflow for the fatigue design of L-PBF AlSi10Mg parts 114
4.3 Fatigue data of L-PBF AlSi10Mg specimens and components 115
4.4 Upgrade of fatigue data from miniature specimen tests 116
4.5 Assessment of the fatigue design methodology 122
5 Conclusions and outlook 125
References 127
List of Figures 135
List of Tables 140

Introduction

Additive manufacturing (AM), particularly Laser Powder bed fusion, is an innovative technology that empowers designers and industries to create high-performance parts characterized by complex geometry, with reduced material waste, increased design freedom, and at the same time, gaining faster production and improved performance. These capabilities can be beneficial for industries requiring specialized components since they can lead to cost savings, reduced environmental impact, increased competitiveness for businesses, and the exploration of innovative fields of application.

The focus of this Ph.D. project was to gain a thorough understanding of the design, development, and qualification process for fatigue-critical components made of L-PBF metal alloy for use in the automotive industry. The activity required examining how various factors such as part geometry, loading conditions, L-PBF process parameters, post-processing, microstructure, and surface roughness impact the properties of the component and how current simulation tools and prediction methods can be used to predict fatigue behavior. It is worth noting that while much of the research on fatigue in AM metals has focused on specimens, this project aimed to develop and assess the entire workflow for creating and qualifying fatigue-critical L-PBF metal parts.

The objective of this research is to fully develop an integrated workflow, starting with the identification of components, progressing through the various stages of the development of parts, and ending with the production of a set of real parts that can be tested to develop a design model to predict the fatigue behavior of parts produced by L-PBF. The current work involved the collaboration with the company Beamit, which has expertise in additive manufacturing and is a leader in the production of powder bed metal components. The dialogue with them helped identify the key steps in using this technology, such as defining component application, material selection, and optimizing the component features. It also enabled the opportunity to gain valuable insights and knowledge about the latest developments and trends in additive manufacturing, which can inform future research and development efforts and ensure that the work is relevant to current industry needs and practices.

The present thesis is organized as follows:

The first chapter will outline the context and area in which additive manufacturing technology is currently flourishing and expanding, beginning with the first application and the industrial interest that, in the past year, has drawn attention from various sectors, particularly those with a focus on high-performance applications. It includes the description of L-PBF

technology, the potential and limits of the technology, and the issues that, due to the technology's infancy and slow diffusion, still need to be resolved, particularly in terms of material characterization and standard method qualification and industrial examples.

The second chapter introduces and explains the methods used to investigate the structural optimization and fatigue behavior of additively manufactured components. It presents a specific case study and details the steps involved in producing the components, including design, optimization, numerical simulation, production, and testing. The chapter also introduces an innovative method for characterizing the mechanical properties of metal using miniature samples and describes the testing setup used to evaluate the components.

The third chapter presents the results of these procedures, including the results of numerical simulations of the structural response and fabrication process and fatigue testing at the specimen level and component level to support the part design and qualification.

The fourth chapter discusses the experimental methodology, highlighting relevant results and outlining the key points that should be addressed during part design and future development.

The fifth and final chapter presents the main conclusions drawn from the study and provides the outlook for future developments in metal AM part development.

1 Background

1.1 Additive Manufacturing

Additive manufacturing, also known as 3D printing, is a revolutionary technology that has the potential to revolutionize the way products are made, enabling the production of custom, one-of-a-kind items with unprecedented speed and precision[1], in addition to the potential of reducing waste and increasing sustainability in the manufacturing process, it is becoming an important option in a wide range of industries, from aerospace and automotive to medical and consumer products [2], [3]. Although the frequent definition uses the phrase "3D Printing" to refer to all Additive Manufacturing techniques, numerous unique procedures differ in their layer-by-layer manufacturing method[4]. 3D printing technology first appeared in the United States, with the company 3D system technology that was the pioneer in introducing photopolymerization of thermoset polymers using UV light, with subsequent stratification of the material layer by layer, allowing to build final component starting from a three-dimensional file[5]. Since then, technology has advanced dramatically, and the focus has shifted from polymers to metals as the potential of the fabrication approach was recognized[6].

Various industries, such as aerospace, automotive, and biomedical, demonstrate an increasing interest in additive manufacturing (AM) techniques, promoting its rapid development. This enthusiasm is due to the unique advantages of these processes: the ability to produce complex and customized parts in a near-net-shape, reduce the parts' weight, limited tooling, and reduced lead-time. The increasing attention being paid to AM technology in recent years is evident in the trend of industrial research and patent applications registered by the European Patent Office (EPO), reported in Figure 1, and the continuing increase in the number of industrial applications highlights the significance of the technology among numerous stakeholders[7].

3D printing offers a range of advantages over traditional manufacturing techniques, including the ability to create highly customized parts with intricate designs and integrated functions, faster time-to-market, reduced material usage and resources, and increased conformity to customer specifications. The technology also enables the creation of geometric features that would be impossible to be produced with traditional methods and allows for the design and production of lightweight components with precise control over material properties such as density and stiffness[8]. The benefits of AM techniques, such as freeform manufacturing capability, material savings, and mass customization, contribute to the growing use of AM techniques in the aerospace, automotive, biomedical, and other engineering industries[9], [10].

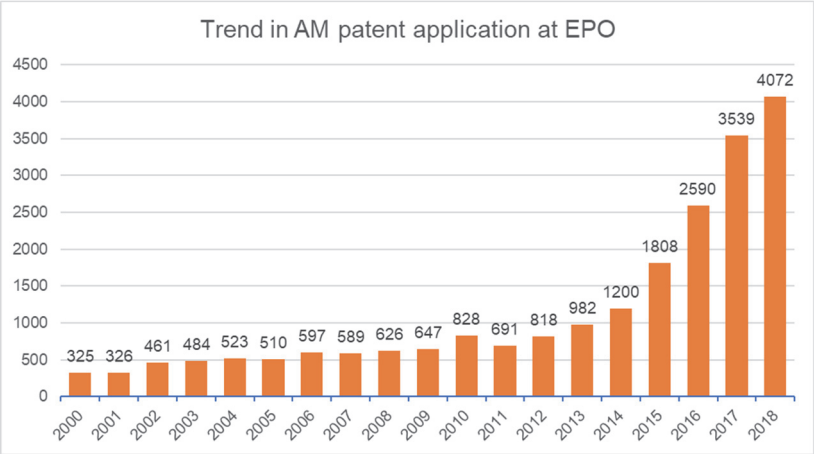

Figure 1- Additive manufacturing-related patent application in the period time from 2000 to 2018 – Source European Patent Office

In recent years, standards were formulated that classify the Additive Manufacturing processes into seven categories depending on the material and machine technology used [11], [12].

1. VAT Photopolymerization uses liquid photopolymer resin, out of which the model is constructed layer by layer.
2. Material Jetting creates objects layer by layer with material sprayed on the build platform.
3. Binder Jetting process combines powder-based material and a binder that are alternatively deposited to generate the final part.
4. Material Extrusion, defined as Fused deposition modeling (FDM), is a common material extrusion process. Material is drawn through a nozzle, heated, and deposited layer by layer.
5. Sheet Lamination processes bond together thin sheets of material layer by layer to form a single piece.
6. Directed Energy Deposition (DED) is a more complex printing process commonly used to repair or add additional material to existing components.
7. Powder Bed Fusion process includes Direct metal laser sintering (DMLS), Electron beam melting (EBM), Selective laser melting (SLM), and Selective lase sintering (SLS) that uses an energy source selectively to melt the powder of a specific material and to build a component layer by layer. SLM and EBM are now identified with the unifying acronyms L-PBF and EB-PBF, where PBF stands for Powder Bed Fusion.

L-PBF is currently the most developed metal AM technology holding a majority of the industrial market. L-PBF is the process of selectively melting metal powder layer by layer to realize high-performance parts typically characterized by complex geometries and high density. The terminology adopted by ISO/ASTM 52911-1:2019[13] is Powder Bed Fusion by Laser Beam or PBF-LB in technical documentation. Therefore, the term "Laser Powder Bed Fusion (L-PBF)" is used in this work.

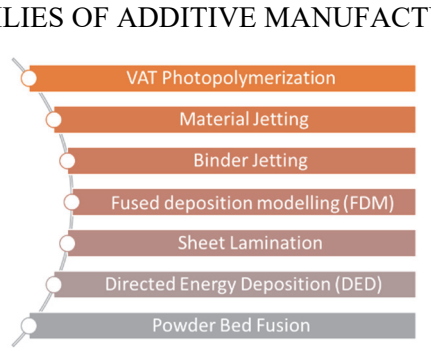

Figure 2 - Seven distinct categories of additive manufacturing technology acknowledged by ISO/ASTM standards (ISO/ASTM 52900)

1.2 Laser powder Bed Fusion (L-PBF)

The most extensively used additive manufacturing metal technology for industrial production is L-PBF, with a wide range of uses in the aerospace, medical, and automotive sectors. Moreover, this technology will be even more used in the future due to its clear advantages over conventional manufacturing techniques, including the possibility to produce high-complex parts, cost reduction, mass customization and part consolidation [8], [14], [15].

The global metal additive manufacturing market was valued at $2.6 billion in 2021 and is projected to reach $14.1 billion by 2031[16].

The projected average annual growth rate from 2021 to 2026 is predicted to be steady across various regions worldwide, with significant growth anticipated in the near future.[17]

L-PBF process has many benefits, such as increased design freedom that enable the production of complex parts, part consolidation and light-weighting, but it is a difficult process that faces several scientific and technological issues that must be resolved to make the technology more economically sustainable and to properly adopt it; a thorough scientific understanding of the technology is required and one of the key considerations in the used of L-PBF be aware of the limitations of the technology to maximize the benefits it offers.

L-PBF has several advantages but also many drawbacks that need to be considered to fully embrace the technology and allow the technology to be widely adopted.

The key benefits of this technology primarily involve streamlining the manufacturing process and the capability to create specialized components with greater efficiency:

- TOOL REDUCTION: 3D CAD model is used to directly produce improved parts without new tooling required.
- MATERIAL SAVING: Additive manufacturing creates less waste and uses less raw material compared to traditional subtractive manufacturing technologies.
- GEOMETRIC FLEXIBILITY and DESIGN FREEDOM: AM enables the production of highly complex parts that are not possible to be produced otherwise and enable the use of optimization method to improve strength-to-weight ratios of the parts.
- PART CONSOLIDATION: AM allows for the production of integrated assemblies of parts, reducing the overall number of parts and avoiding welding between different parts.
- TIME-SAVING: Time-to-market reduction and supply chain logistics simplification

Even if this technology is revolutionizing the industry, AM processes also build up some new challenges due to the intrinsic defects and peculiar surface roughness, which can lower the mechanical properties, especially fatigue performances. There are also several drawbacks that hamper the widespread adoption of this technology, particularly due to the preliminary stages and development of the technology and the need to manage many variables that affect the final output:

- POST PROCESSING: is often required and resource intensive post-processing, including support removal and machining, may be required for improved surface finish and accuracy
- SIZE LIMITED: The dimension of the manufacturing chamber is limited; small parts can be efficiently produced using AM, but the overall size is usually limited for L-PBF.
- PROCESS CONTROL: The finished part is affected by a wide range of variables, including build speed and component orientation, and this variation changes the part's material properties.
- SURFACE FINISH: The precision and finishes provided by machining cannot be matched by AM techniques. As a result, depending on their intended purpose, items created through additive fabrication can need additional processing.
- LACK OF PROCESS STANDARDS: Lack of industry-wide adoption also contributes to the lack of standards, but as the technology becomes more prevalent, standards will likely be developed for consistent, high-quality production.

- COST: the process is recognized as particularly expensive because of the high cost of the metal powder, the energy for the manufacturing equipment and the workforce for preparation and post-process activities on the job.

1.3 Industrial applications of L-PBF

The evolution and advancement of the Laser powder bed technology have attracted the attention of many industrial sectors that, during recent years, were positively convinced by the AM technology potential and started introducing L-PBF manufacturing as a consistent production technology used for the fabrication of components[18].

AM finds application in the automotive and aerospace sectors, where light, resistant components with a high degree of customization are required. Recently an increasing use of this technique was registered because it can respond to structural optimization problems, thanks to the ability to create very complex geometries, with high flexibility and customization, without giving up excellent mechanical properties.

Wohlers associates surveyed service providers, machine manufacturers, and producers of materials and desktop 3D printers to determine which industries they serve and the approximate revenue in percent they receive. According to the findings, the top four industries for AM are automotive (16.4%), consumer products/electronics (15.4%), aerospace (14.7%), and medical/dental (13.9%)[19].

a) b)

Figure 3 – a) AMOS-17 command horn antenna BOEING; b) GE Aviation additively-produced fuel nozzle tips for the LEAP engine

The aerospace industry was the pioneer in the use of L-PBF. Boeing has been engaged in additive manufacturing research with a number of components already created (Figure 3a) and integrated into space launch systems[20], [21]. One of the first important applications

demonstrating that L-PBF is a serial manufacturing technology is the fuel nozzle for GE Aviation LEAP jet engine (Figure 3b) [22].

Moving to the automotive sector, Bugatti has designed and built one of the largest topology-optimized titanium parts with L-PBF (Figure 4a). The new titanium brake caliper weighs just 2.9 kg resulting in a weight saving of over 40% compared to a conventional brake caliper[23]. Divergent developed a completed new approach for high-performance manufacturing cars called Divergent Adaptive Production System (DAPS) involving the use of 3D printed metal nodes that would use intelligent robotics to create a lightweight, high-performance car (Figure 4b) with a completely optimized structure[24].

Motorsport is eagerly interested in AM since traditional production cycles and processes are unable to keep up with the demands of the motor racing industry. Formula 1 teams, for example, are required to develop and produce complex parts between races, sometimes even overnight. Additive Manufacturing (AM) has the potential to transform the manufacturing process[25].

a) b)

Figure 4 –a) Bugatti 3D-printed brake caliper; b) view inside the engine bay of Czinger 21C.

The capacity to highly customize products and the compatibility of biological structure and material made it possible to apply the technology for dental implants and articulation prosthetics, making the medical sector one of the most consolidated. PBF technologies offer economic advantages for individualized patient-specific and low-cost production of medical device products and are already extensively used for many applications[26], [27].

The sports equipment sector shows recent important L-PBF applications. In 2022 the bike company Pinarello designed and produced with L-PBF the frame of a high-performance road bike (Figure 5). The bike embraced the potential of the AM technology to create the customized shape specifically designed on the anatomical position and body of the rider Filippo Ganna, who, with the innovative bike, was able to beat the world record on the distance covered in one hour. The frame material was Scalmalloy [28], [29] an innovative Aluminum-scandium alloy specifically

developed for AM application. The design freedom also allowed to embody some aerodynamical features and graded volume to optimize the shape and the performance of the bike[30].

Figure 5 –Pinarello's Bolide F HR 3D features an additively manufactured Scalmalloy frame

Additive manufacturing was also implemented by Bastion Cycles in manufacturing the bike frames for Australian Cycling Team for the 2020 Olympics; however, the AM handlebar failed, causing an athlete to fall onto the track. This prompted a thorough investigation into the failure helping in recognizing the reason and learning an important lesson in design part manufactured by L-PBF [31]. This example illustrates the importance of following a standardized workflow when producing additively manufactured parts. By focusing on the most important steps and striving to achieve the best and most reliable solution, it is possible to produce high-quality parts.

1.4 The L-PBF technology

Laser powder bed fusion (L-PBF) is the most advanced additive manufacturing process. It produces near-net-shape metal components of high geometrical accuracy unmatched by traditional forming technologies, such as casting and forging. Casting can produce complex shapes, but the surface roughness and defect content are higher than L-PBF. Forging is limited in geometrical complexity. Further, they both require important tooling investments.

The main reason of interest for the L-PBF technology for various industrial sectors is its process reliability and repeatability. However, a distinctive aspect of the L-PBF process is the complex interaction among many factors that determine various interrelated physical processes influencing the final part quality. A successful part production by L-PBF is the result of the fundamental process qualification phase

The L-PBF process can be interpreted as the result of the superposition of more than 130 input parameters[32] and the interaction of many subprocesses, including the absorption and reflection of laser radiation, heat and mass transfer, phase transformation, moving interface between phases, gas and fluid dynamics, chemical reaction solidification and evaporation,

shrinkage, deformation. The laser beam interacts with a layer of metal powder that has been redeposited on the base plate generating the single-track that represents the fundamental structural building block; when many single tracks are integrated into one layer, a three-dimensional object is produced. A detail representation of the interaction between the laser and the material powder substrate is represented in Figure 6, reproducing the localized melting of the material by the energy source.

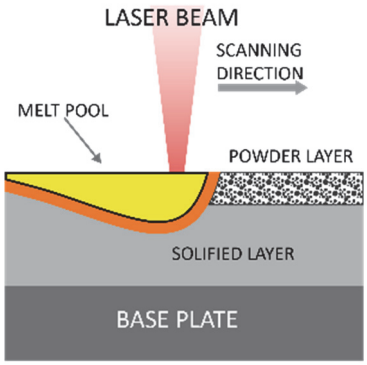

Figure 6 - Interaction between the source of energy and the powder material in the L-PBF process

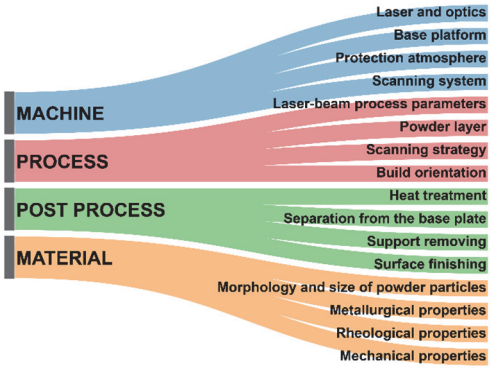

Figure 7 – Four main factors that are responsible for the final quality of an L-PBF part and related properties

The final quality of components fabricated by L-PBF is affected by four major sets of parameters: material-dependent parameters, machine parameters, process parameters, and post-process parameters. All these elements need to be considered because they control the effectiveness and quality of the final part description, and their role is evaluated and qualified by testing and inspecting the produced parts.

Figure 7 graphically shows the links between the four parameter sets and the specific influencing factors that are to be optimized for effective L-PBF processing. The main aspects of each group are discussed in the following sections.

1.4.1 AM Fabrication Systems

The good operability of the hardware is a key element for the technology to guarantee a high quality of the final part as well as the control of the conditions under which fabrication methods operate. The central elements of the L-PBF systems are the laser scanning system, the powder delivery system and powder deposition system, the build platform movement system, the powder removal system, the gas supply system and the filtration system.

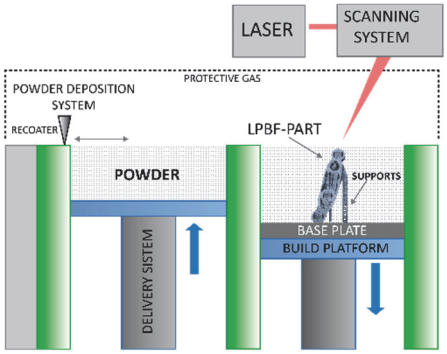

Figure 8 – L-PBF process: laser-material interaction and representation of a L-PBF fabrication system

Figure 8 shows the schematic representation of the Laser Powder Bed Fusion process with the illustration of the interaction between the source of energy, the laser, that selectively melts the metal powder to produce the final object layer-by-layer.

One to four laser sources are used in modern L-PBF systems to selectively melts regions of a powder bed. The powder deposition system applies a uniform layer of powder to the base plate on which the objects are manufactured; the substrate material must ideally correspond to the powder material or be similar in chemical composition to match each other in weldability. Soft blade recoaters are used to spread the powder layer to not experience process failures. The L-PBF process is carried out in an inert gas atmosphere to protect the metal material from oxidation and to prevent contamination of the powder layer, which can negatively affect the quality of the manufactured parts, a filtration system is used, and an inert gas flow is used to remove spatter particles from laser-powder interaction zone that can lead to defects in L-PBF parts.

1.4.2 Process parameters

To create high-quality 3D L-PBF parts that have a high density, good surface finish, and strong mechanical properties, it is important to carefully select and adjust the process parameters for each type of alloy being used in the manufacturing process. In the L-PBF process, many parameters affect the quality and performance of the final part, like the layer thickness that represents the height of each substrate and the hatch distance, that is the distance between each scanning line; the laser beam moves over the build plate with a specific scanning speed, and defined laser power. Different scanning strategies can be selected to control the material properties and uniform the microstructure of the material between the different layers. The qualification of the process and the identification of the best combination of process parameters is the central activity in research activities on additive manufacturing. Components characterized by surface produced with a critical angle with respect to the build platform require supports structures that are necessary to consolidate the part to the built plate and dissipate the heat; support structures help in avoiding deformation during manufacturing and guarantee a convenient and straightforward separation of the finished part from the base plate[33].

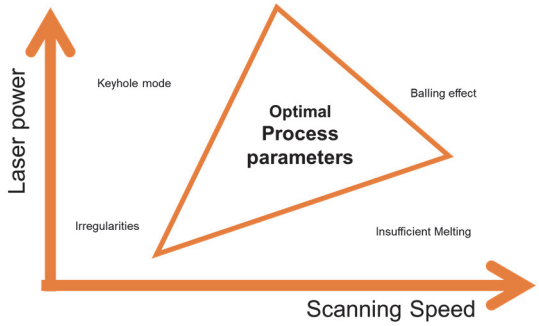

Figure 9- Example of a qualitative representation of optimal processing map and list of undesirable printed features and defects

The optimal window of process parameters combination for every type of material is the main goal of the development and qualification of the L-PBF process for serial production in the industry. Sub-optimal process parameters can lead to a multitude of defects and unwanted features, such as poor surface finish, dimensional inaccuracies, and flawed material properties, which can all lead to structural failure or result in the product not meeting quality requirements. Optimal process maps, as the qualitative example of Figure 9, support process qualification and ensure consistent and high-quality part production.

1.4.3 Post-processing

Parts manufactured using the L-PBF process may not meet all product requirements directly in the "as-built" state; therefore, post-processing is often required to achieve the final condition. One of the biggest obstacles to the adoption of additive manufacturing in many industrial sectors is the cost of the entire cycle, from powder to post-processing. Different analyses found that pre- and post-manufacturing processes can account for up to 40% of the cost of additive manufacturing products [34]. The definition of efficient post treatments is receiving more attention, and postprocessing techniques for parts made using additive manufacturing, which are frequently customized, are developing quickly. Post-processing can primarily aid in reducing the overall porosity, undesirable residual stresses, microstructural directionality, and irregular surface morphology induced by the removal of the support structures[35].

One of the main advantages of additive manufacturing is the ability to create parts with little to no need for post-processing, but sometimes the final surface may require some intervention, especially when it comes to support removal and surface uniformization. Poor quality and high roughness can have a negative impact on performance, particularly in terms of fatigue behavior[36]. Surface morphology is mainly described by the layer-by-layer deposition process, the presence of partially melted powders particles, spatters during the localized melting, or imprecise support removal; all these factors can lead to an irregular surface that can hinder the functionality of L-PBF parts and their interaction with the environment[37]. Improvements in microstructure to obtain isotropic mechanical properties and tensile residual stress relaxation can be expected by performing specific heat treatment on the additively manufactured part. Material-specific heat treatments and highly effective surface finishing are employed to reach the best part quality.

An investigation of the effect of surface post-treatments aimed at efficiently removing the support structure from a component was performed during my study stay at European Space Agency ESA in Noordwijk (NL). The focus of the study was the assessment of an electrochemical surface post-treatment capability to remove the typical L-PBF building supports and to reduce the overall surface roughness from Inconel 718 specimens. Fatigue tests, tensile tests and roughness measurements were performed to determine the different responses of the L-PBF Inconel 718 alloy in the presence of the as-built surface state, a jet-blasted surface, and the electrochemically processed surface condition (Figure 10). The main outcomes of this activity are being included in a manuscript to be submitted for publication.

a) b) c)

Figure 10 – View of surfaces after support removal according to different methods: a) reference condition due to manual support removal; b) support removal by jet-blasting; c)support removal by the electrochemical process

1.4.4 Materials

Powder bed technologies are based on the use of gas-atomized metal powder that must have the right chemical composition, particle form, size distribution, and flowability since these properties of the material have a direct impact on the L-PBF process and final result. The morphology of dust particles influences two important properties: packing capacity and sliding ability determining the quality of the final component, the packing capacity of the powders is related to per part porosity, and the sliding capacity of the particles determines the quality of the powder layer that is spread before being melted by the laser [38]–[40].

Many alloys are usually used for the fabrication of parts using L-PBF, and new materials are continuously studied to be introduced for production and answer the request of high-performance applications [41].

The more common alloys for the fabrication by in laser powder bed fusion (L-PBF) are:

1. Aluminum alloys are widely used in L-PBF due to their low density and high strength-to-weight ratio. They are commonly used in the aerospace, automotive, and defense industries, as well as in consumer products and sporting goods[42].
2. Stainless steel: Stainless steel alloys are popular in L-PBF due to their corrosion resistance and mechanical properties[43].
3. Cobalt chrome: Cobalt chrome alloys are known for their high strength and wear resistance, making them useful in L-PBF in the aerospace and medical industries[44].
4. Titanium: Titanium alloys are widely used in L-PBF due to their high strength-to-weight ratio, corrosion resistance, and biocompatibility. They are commonly used in the aerospace, defense, and medical industries, as well as in the oil and gas sector[45].

5. Inconel: Inconel alloys are known for their high-temperature strength and corrosion resistance, making them useful in L-PBF for applications in the aerospace, defense, and energy industries[46].
6. Other alloys that are used in L-PBF include copper, brass, and bronze. These alloys may be used in applications such as electrical and thermal management.

The research activity of this Ph.D. study period has been devoted to different L-PBF metals and their fatigue behavior. While the focus of this dissertation is on L-PBF AlSi10Mg, a widely used alloy for lightweight applications, investigation of other metal alloys provided a valuable overall picture of the current evolution of L-PBF technology. Fatigue samples of Inconel 718, an established Nickel-based superalloy widely used in the aerospace industry for high-temperature applications, were produced using different L-PBF systems with optimized process parameters. The relationships among process parameters, as-built surface quality, build direction and fatigue strength were investigated in detail and the main results were reported in [47]–[49]. More recently, the innovative Al2024- RAM2 aluminum alloy was also investigated and the test results describe the dependence of the fatigue properties on the surface roughness, material microstructure, and directional fabrication[50]. Similarly, the fatigue strength of Ti6242, a titanium alloy commonly used in high-pressure compressors of jet engines and recently qualified for serial L-PBF production by Beam-It, was investigated in dependence on the surface roughness, material microstructure, and directional fabrication. Results are going to be published shortly.

1.5 Technology-dependent factors affecting L-PBF parts

When designing and producing parts via L-PBF, it is essential to ensure that components can fulfill the functional objectives and design standards, which calls for rigorous evaluation of the various production process phases, material properties, and component characteristics. The components' resilience to keep their structural integrity over time is crucial to confirm that the parts are created and constructed to withstand the environment for which they are intended[18]. To completely comprehend and regulate the behavior of these materials, it is essential to characterize the mechanical properties of L-PBF materials. This is crucial in sectors like aviation, energy, and aerospace, where accurate validation of components and procedures is necessary. To ensure the safety and dependability of materials used in these industries, tight rules frequently call for careful control over their mechanical qualities.

To ensure that metals manufactured using L-PBF meet the necessary performance requirements, it is important to evaluate their properties. Material testing involves conducting standardized tests, such as tensile and compression tests, to determine the strength, stiffness, and ductility of L-PBF parts. When designing a part for use in a specific environment, it is important to consider the several types of loads that the part may be subjected to, including static and dynamic, that can have an impact on the behavior and properties of the concerning structural application. Fatigue occurs because of repeated loading and unloading cycles, can affect the durability and reliability of the part, especially in structural applications. Factors such as the part's geometry, stress distribution, and internal properties can all influence its fatigue behavior and it is essential to consider these factors in the design and selection of materials for L-PBF parts to ensure their performance and reliability.

The layer-by-layer nature of L-PBF determines the formation of unique surface morphology and microstructures within the finished part, resulting in different mechanical and physical properties compared to conventionally produced parts. There are several features that describe the mechanical properties of components manufactured using L-PBF, including surface roughness, material microstructure, defects distribution, and residual stresses, and the combination of all these features play a significant role in determining the overall characteristics of the component.

Since these factors have been extensively investigated on different L-PBF metals during this Ph.D. activity, a discussion of the relevant available literature can be found in the published contributions by this author.

1.5.1 Surface morphology

The L-PBF surface morphology is defined by various phenomena, ranging from stair-step effects due to the layer-wise manufacturing method, the layer thickness, the size of powder, and interactions within the melt pool[51]. Upward (upskin) and downward (downskin) surfaces are distinct from one another, with downskin frequently being rougher and having lower surface quality than upskin [48].

Surface morphology is affected by support removal in the area in contact with the support material and accurate removal operations are required to avoid negative effects on the final part. Surfaces in contact with the powder during solidification result in the attachment of residual particles and consequent higher surface roughness[52]–[54].

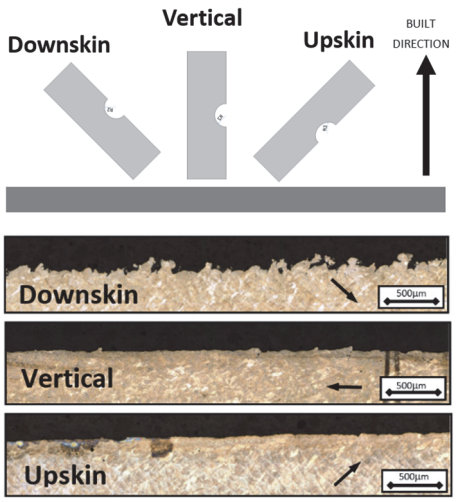

Figure 11 – a) Specimen orientation and denomination; b) Surface morphology and near-surface microstructure obtained observed on IN718 samples (the black arrows indicated the build direction) [48].

The effect of the process on the surface morphology of different L-PBF metals to understand the effect of the morphology on the mechanical properties of the AM parts has been studied intensively by this author. The orientation of the part in the build chamber is the main factor determining the final quality of the part, as reported in Figure 11. Characterization of the surface roughness with different measurement techniques and subsequent correlation with the mechanical response was presented in [47], [55]. Further, the severity of surface roughness can be compared to a system of micro notches acting as possible crack initiation points, thus generating local stress concentrations that contribute to reducing the fatigue performance of parts. This aspect was studied using FE simulation by reproducing the surface profile as a series of notches. The numerical results proved that the higher the surface roughness, the higher the stress concentration at the notch roots of the roughness profile[56].

1.5.2 Material microstructure

The build orientation affects the solidification and the properties of the material's microstructure. The microstructure is described by the shape of the melt pool generated during the manufacturing process, as well as by the hatching distance and contour parameters of the different parts of the component. The melt pool shape, hatching, and contour parameters describe the geometric features of the component and how the mechanical properties are influenced[57]. This can cause material anisotropy determined by the defects distribution that changes the

mechanical response of the material and by the orientation of the grains, which are usually elongated in the direction of the thermal gradient. [58]. The high thermal gradients and solidification rates in L-PBF can result in the formation of a very fine cellular or cellular-dendritic microstructure[59], [60].

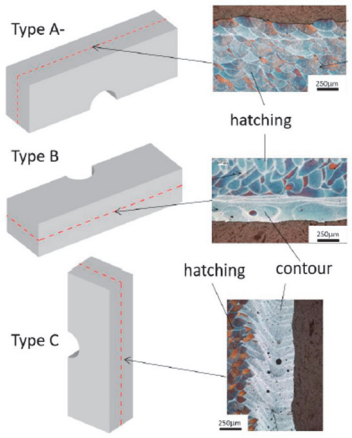

Figure 12-Different areas of the samples microsection shows peculiar feature caused by the specific orientation and build direction and the selected process parameters [61].

To clarify how the microstructure depends on the parameters of the L-PBF process, and therefore it may be directional, Figure 12 shows the cross-sectional views of chemically etched AlSi10Mg in the as-built state studied in [61]. Depending on the sectioning plane, the surface may be formed by contour layers (parallel (B) or perpendicular (C) to the plane) or hatching layers (A-). Defects (small gas pores) are observed in the contour layers, while the hatch microstructure appears defect-free.

1.5.3 Defects distribution

The formation of defects in L-PBF parts is an issue that affects the performance and reliability of components. Studying the mechanisms behind pore formation and developing methods to reduce or eliminate them, allow to improve the application of the technology in critical functions[62]. The formation of internal defects, such as pores and lack of fusion can reduce the strength and durability of components; defects can occur in various sizes, shapes, and distributions, and can be difficult to control, making it challenging to ensure consistent qualification of the parts[63], [64]. Porosities in L-PBF parts are typically small, rounded and

uniformly distributed, minimizing the risk of crack initiation; Lack of fusion (LoF) and keyhole defects are can occur in L-PBF parts because of inefficient melting of the powder and keyhole porosities are generated by the formation of void in the melt pool leaving a trapped vapor cavity in the material as it solidifies [65], [66]. Their presence is particularly detrimental for fatigue application because their irregular shape lead to crack initiation and propagation, reducing the operation of the parts[67], [68].

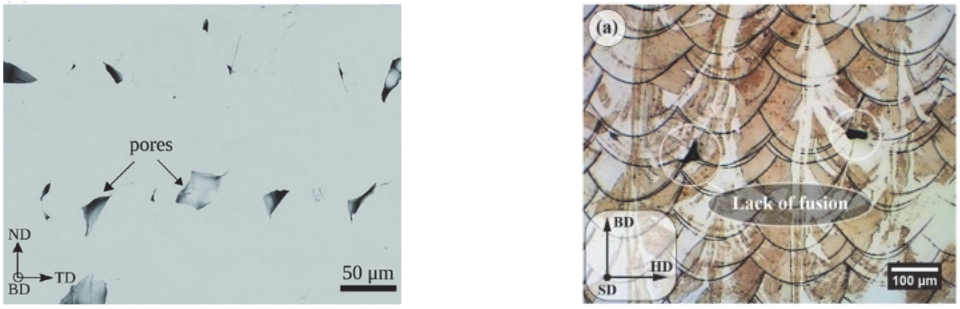

Figure 13 – a) Microstructure of the L-PBF-densified sample showing pores in a view perpendicular to the build-up direction. [64], b) Annotated as-built material microstructure images [66]

Our experience with AM metals produced according to qualified production processes by Beamit has demonstrated near-theoretical material density and internal defects of very small dimensions. Since the fatigue properties of parts with surfaces in their as-built condition was our research focus because its practical significance (i.e. cost containment), we observed that fatigue crack initiation always initiated from the surface irregularities where stress concentration is higher than at small internal defects. However, internal flaws of dimension above of a threshold value may critical in fatigue when the surfaces are polished.

1.5.4 Residual stresses

Residual stresses are a common issue in L-PBF and can have a negative impact on the performance of L-PBF parts. They are caused by the rapid heating, melting, solidifying, and cooling cycles that occur during L-PBF, as well as the layer-by-layer nature of the process. These stresses are caused by the rapid heating of the material, which expands but is hindered by the adjacent material at a lower temperature and vary with build orientation due to differences in thermal history. When the heat source is removed, these areas begin to cool and shrink, generating tensile stresses that are balanced by the compressive stresses in other areas. [69]–[72]

Residual stresses can be reduced through post-fabrication heat treatments, such as stress relief or aging, in high temperature furnaces but during the process can lead to macro- and microcracking, deformation, and delamination of parts from the base, that can damage the parts and the system. High residual stresses near the surface can weaken the part's fatigue endurance, especially if the part is also subjected to tensile loads during operation; on the other hand compressive residual stress could positively affect the mechanical properties and under certain condition could be also desired. While residual stress is a common issue in all metal manufacturing methods, including L-PBF, it can be managed and controlled through careful optimization of the process parameters and post-processing treatments.

One aspect that has been investigated in this thesis is the usefulness of L-PBF process simulation when applied to determine either the danger of material cracking and job failure or the residual stress locked into the part at the end of the process that will superpose to the live-load-induced stress that affect the fatigue strength of a AM component. A full discussion of the implications the residual stress for the fatigue response of as-built AlSi10Mg specimens and parts is given in the following chapter.

1.6 Static properties of L-PBF metals

Static Mechanical properties are the reference properties used in engineering design and materials qualification and to evaluate the performance of different materials and select the most suitable material for a given application. Material testing for metals manufactured by additive manufacturing is critical because the mechanical properties of L-PBF parts can vary significantly depending on the manufacturing conditions, process parameters, part orientation and final heat treatment applied to the component[73].

The tensile properties of L-PBF material can be anisotropic primarily due to the presence of anisotropic microstructure, lack of fusion defects, and macrostructure feature such as melt pools[64], [74]. These factors can cause the material to have different mechanical behavior in different directions, leading to variations in its tensile properties depending on the direction of the applied load[75].

Performing standardized tests, such as tensile and compression tests, allows to verify that the parts have the required strength, stiffness, and ductility to withstand the loads and stresses they will encounter in service; material testing can be used to identify potential defects or flaws in L-PBF parts, such as porosity or inclusions, that can affect their performance [58].

Uniaxial tensile is used to collect the basic static material properties such as young's modulus, yield tensile strength, Ultimate tensile strength, and elongation at fracture. Hardness measurements are conducted as non-destructive method to quantify the basic static properties and this kind of test are usually performed at every production to verify and ensure the respect of the basic material properties of the produced parts.

All the specimens and parts that we investigated in this research activity were produced by Beamit using qualified powder, modern and certified L-PBF equipment and optimized process parameters. The process qualification for a give metal powder is aimed at the achievement of adequate static mechanical properties, such as UTS, yield stress, and elongation to rupture. After qualification for industrial production the L-PBF process is "freezed" and the reference material data are published in the company data sheets.

1.7 Fatigue on L-PBF metals

Fatigue response is the key material phenomenon considered in this study because it is directly connected to the dynamic loading conditions typical of structural parts in automotive and aerospace sectors. Fatigue is responsible for most failures in the operation of aircraft components, with a percentage exceeding 90%[76]–[78].

Fatigue in metals refers to the process by which a metal becomes damaged or weakened over time because of exposure to cyclic stress or strain of significant magnitude. When a metal is subjected to cyclic stress or strain, local micro deformation at the surface may evolve into one or multiple micro cracks that with time evolve into a macrocrack. This is a damage of the part that evolve and may precipitate until the final collapse of the part. Fatigue is a common problem in metal structures and is one of the main causes of failure in metal components, in additive an extended knowledge of the fatigue properties is one of the major concerns and an efficient characterization of these properties is vital to optimally use the AM technology[79].

The relationship between a material's maximum stress (S) and the number of loading cycles (N) needed to cause failure is described by the S-N curve. By exposing a material to a variety of stresses and counting the cycles needed for failure at each stress level, the S-N curve is typically determined experimentally. The Wöhler diagram is a tool used to describe the fatigue resistance of a material and its ability to withstand cyclic loads over time without breaking. Fatigue can be of two types: low-cycle fatigue (LCF) and high-cycle fatigue (HCF), depending on the number of cycles a component can withstand before breaking. LCF is characterized by elasto-plastic deformations at each cycle, which means that macroscopic plasticization of the material occurs at

values of σ greater than the yield stress, resulting in a reduced material life. HCF, on the other hand, is characterized by deformations only in the elastic field, as σ remains below the yield stress, with plasticization only at the microscopic level.

The transition between the two fatigue regions depends on the ductility of the material, but it is generally assumed to occur around $10^3/10^4$ cycles. High-cycle fatigue is the most important from a practical point of view and the fatigue limit describes the stress below which it is assumed that the component will have an infinite life.

Being a common mode of failure of metals, fatigue is also an important consideration when using L-PBF to manufacture components. The microstructure of the material can significantly impact its fatigue behavior and the presence of internal defects, such as pores and porosity, can also negatively affect fatigue behavior by creating stress concentrations that can lead to early failure.

An accurate characterization of the fatigue behavior of a material is typically a complex, costly and time-consuming process because there are many factors that can affect it. The more so in the case of L-PBF metals because of the high costs of metal powder and of the AM equipment maintenance and use.

Fatigue strength of a given material depends on type of loading, frequency, environment, specimen geometry, material defects, surface quality, etc. Fatigue data are typically scattered, therefore multiple specimens must be produced and tested to obtain a significant material response. The fatigue behavior is typically investigated using standard specimens and procedures and the reference fatigue data provide are used by designers when assessing the safety of new parts.

Generation of reference fatigue data is therefore very important for L-PBF exploitation in industry although the link between L-PBF metals and their fatigue properties is complicated by the novelty of the technology and the large number of influencing factors. To gain insight into the fatigue response of L-PBF metals while containing the staggering production costs of standard specimens, an original fatigue testing approach using miniature specimens has been extensively used on several L-PBF metals throughout this study period. The primary features of the method and results of its application to L-PBF metals will be given in the next chapter.

The fatigue behavior of L-PBF-manufactured metals is often characterized by significant anisotropy due to the layer-wise nature of the technology. This anisotropy can result in differences in fatigue strength depending on the orientation of the part in the build chamber, as the external morphology and microstructure can vary. This can have an impact on the overall fatigue behavior of the material [80]–[82].

Surface roughness can affect the fatigue behavior, with rougher surfaces tending to have poorer fatigue behavior than smoother surfaces [52], [83]–[85]. It has been demonstrated that machining the sample's surface, significantly contribute in improving fatigue strength, the effect of the as-fabricated surface on the fatigue performance has been observe to be detrimental for both AlSi10Mg and In718 alloys, as reported in Figure 14; the machining of the surfaces allowed to obtain a remarkable increase in the fatigue strength; however if as polished surface is often desired, is not always feasible and sometimes is necessary to maintain surfaces in the as-built state and consider to design the parts in that condition [86], [87].

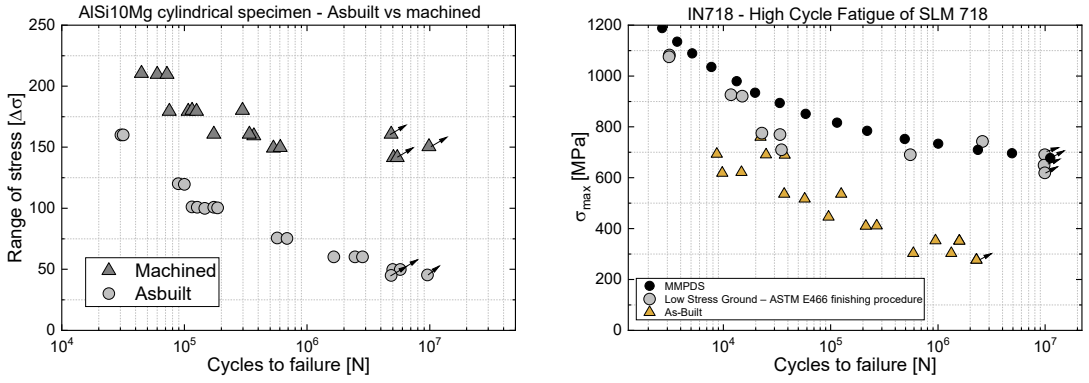

a) b)

Figure 14 - Effect of surface finishing on fatigue behavior L-PBF metals. a) Improvement of the fatigue strength of AlSi10Mg after machining [87]; b) Detrimental effect of as built L-PBF surface morphology on fatigue behavior of IN718[86]

The possibility to make items with intricate shapes and geometries that would be challenging or impossible to manufacture using conventional manufacturing techniques is one of the advantages of 3D printing technology, but this complexity determines to be challenging the use of conventional surface finishing methods on the parts, which could raise production costs and extend the time to market. In many instances, it is best to leave the parts in their original state to guarantee a competitive cost of 3D printing. For this reason, it is important to consider the superposition of this factors on the cyclic properties of 3D printed parts since this can have a significant impact on their performance and to carefully design and manage the surface finish of 3D printed parts to ensure their durability.

1.8 Structural Design of L-PBF parts

The several benefits that the L-PBF technology provide to companies guarantees them a competitive advantage in relation with the ability to efficiently design and produce parts characterized by complex geometries and lightweight structures. In sectors such as automotive and aerospace the possibility of reducing the weight of components can have significant benefits in terms of fuel efficiency, performance and in terms of flexibility in production.

A recognized limitation in the widespread adoption of L-PBF to produce structural components is the capability of ensuring their structural integrity under dynamic loading conditions. The fatigue behavior of L-PBF components is influenced by stress gradients, residual stresses, surface morphology and internal defects and the overall evaluation of L-PBF structural integrity is vital to qualify the final properties of the printed parts. Understanding the combination of the various factors that affect the stages of component development is crucial and acknowledging how the relationship between these parameters determines the component's final properties is fundamental to embrace the technology and be aware of its potential, a full-scale structural component can be influenced by many factors and all of them need to be recognized and fully considered.

There have been few studies that have tested full scale L-PBF components, most of the research in this area has focused on characterizing the mechanical properties of 3D printed components using sample testing, with the assumption that the results of these tests can be directly applied to the performance of the components in actual use. However, it is important to also consider how these properties may be affected by real load conditions and to test the components under these circumstances to better evaluate their performance.

Many studies have been conducted on the potential for using L-PBF to produce optimized parts, as the process allows for greater geometrical complexity and the possibility of reducing the weight of components. Topology optimization has made it possible to create innovative shapes that can be relatively easily fabricated into actual parts[88]–[90].

The geometrical complexity of parts produced using additive manufacturing adds an extra layer of difficulty to the evaluation and prediction of mechanical properties, making it necessary to conduct experiments to qualify the part and an essential step in ensuring an adequate fatigue performance. The fatigue behavior of intricate structures depends not only on the basic material properties but also on the complex interaction of geometrical features (notches etc), surface roughness and the operating conditions of the actual part. Fatigue tests of optimized part under various loading conditions support the qualification of the L-PBF parts [91].

However, there is a limited number of studies available in the literature that deal with the entire L-PBF part development workflow, which is from the structural design of optimized parts to manufacturing, post-processing, and final qualification by realistic testing.

A notable recent work jointly developed at POLIMI and ESA [87] consisted in a comprehensive benchmark activity for the assessment of an AlSi10Mg component made by the L-PBF process. The fatigue performance was evaluated for both as built and machined conditions of small specimens and a benchmark component (demonstrator). A fatigue assessment procedure demonstrating the transferability of fatigue performance from AM specimens to components was developed using with a fracture-mechanics-based approach. Size and distribution of defects and the heterogeneity of the residual stresses were considered. The fatigue performance of as-built specimens was comparable to those of the as-built demonstrators, while a significant difference was observed for the machined conditions of specimens and demonstrators.

Another study, presented an example of an optimized conrod, considering a critical automotive engine component that was designed with the aim of reducing the weight through topological optimization [92], [93]. The durability of a lightweight titanium alloy (Ti6Al4V) conrod made using selective laser melting (SLM) was investigated comparing prediction and full-scale fatigue test results conducted on the conrod under loading conditions that simulate real-world use.

A significant study was conducted in the context of a Formula Student racing car development to explore the feasibility of using L-PBF to produce metallic parts. It describes the entire process of selecting significant components, optimizing their design, producing them using L-PBF equipment and validating their performance through actual use and testing on a racing circuit [94].

Developing a workflow that outlines the steps involved in creating structural additively manufactured parts is crucial for identifying critical issues and key considerations.

The workflow presented in this dissertation will cover the entire process, from design to fabrication and qualification of the structural part. It is crucial to carefully plan and prepare for the various activities that will be required in the service application to create a reliable component and this approach is also necessary when developing lightweight components and the parts must follow strict qualification procedures.[95], [96].

The aims of this study are i) to present and discuss the entire workflow required to design, manufacture and qualify a structural part to be produced by Laser Powder Bed Fusion and subjected to fatigue loading and ii) to assess fatigue test results of the component against fatigue life predictions obtained according to specific design methodology.

The goal is to assess and to predict the structural performance of L-PBF metal parts by studying the impact of dynamic loading, residual stresses, surface condition, and other factors on the fatigue behavior of L-PBF aluminum. This will involve using a range of tools and methods, such as geometrical topological optimization, AM process simulation, and testing both actual parts and specimens made from AlSi10Mg alloy powder in an industrial L-PBF system. .This study will contribute to the development and use of design methods for L-PBF metal parts operating under realistic service conditions thus promoting widespread adoption of L-PBF in industry.

2 Methods

2.1 Design, Production and Testing of an AM Component

High performance and reliability in 3D printed metal parts are obtained when various critical steps including material selection, design and preparation, support structures positioning, fabrication optimization and post-processing are carefully considered and implemented. Extended experience and knowledge of the L-PBF technology is required to manage all the information involved in the development process.

The activity of this thesis has been characterized by the hands-on experience and know-how on the L-PBF technology gained through close collaboration with the technological partner Beamit Spa (Fornovo di Taro, Parma, Italy), a leading service company in additive manufacturing with extensive expertise in powder bed metal components. The extensive experience of Beamit has provided valuable insight and knowledge about the latest advancements and trends in additive manufacturing and awareness of current industry needs and practices. The hands-on cooperation provided the required and comprehensive knowledge of all stages of the L-PBF part production workflow and the access to industry-grade L-PBF equipment. Further, it highlighted the crucial steps of the technology, such as determining external conditions to sustain, selecting materials that can respect the requirement of the application, and optimizing the component's characteristics.

However, the focus of Beamit as a service AM company is the production of parts using qualified materials, processes and equipment while the actual part design and its qualification for the application are in charge of the customer. The main goal of the present thesis was therefore the exploration of the entire development process of an L-PBF part for structural use, from the initial part identification and design phase through the part production phase and the final qualification by testing phase ending with the definition of a comprehensive workflow specifically tailored for L-PBF technology and structural applications.

The design workflow for fatigue-critical additively manufactured metal components is a comprehensive process that includes multiple steps and various software tools. This workflow is necessary to ensure that the components are designed and qualified properly. However, one issue with this workflow is the use of multiple software tools, which can make it difficult to operate in a single, unified digital environment, the knowledge gained through this work highlights the importance of being aware of the specific tools necessary to design and produce these types of

components. The goal of the workflow is to successfully integrate the outcome obtained from all of the different software tools in order to produce a fully functional part.

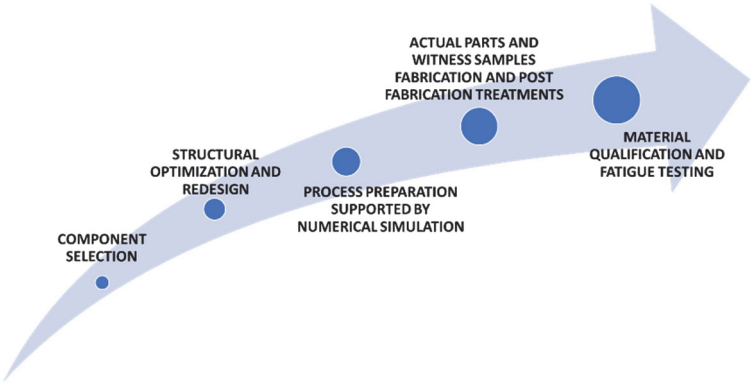

Figure 15 - Workflow for design, production and qualification of an L-PBF component

Representative fatigue data are also needed for part design. Therefore, production and testing of numerous witness miniature samples was carried out to quantify the influence of technological-dependent factors such surface finish, microstructure, heat treatment, residual stresses on fatigue performance.

An integrated workflow, graphically reproduced in Figure 15 , has been developed and applied throughout this thesis and is proposed as a guide for designing L-PBF components subjected to fatigue and ensuring performance and reliability requirements. The principal steps included:

i) Component selection: which define the geometry and the boundary condition applied to the part of interest, including the load applied to the part and the material selection.
ii) Structural optimization and redesign: software tools are employed to optimize the shape of the component and improve the overall performance.
iii) Process preparation supported by numerical simulation to optimize part production: before the fabrication, the best orientation of the part in the build volume and optimization of the supports structure position are conducted.
iv) Actual parts and witness samples fabrication in an industrial-grade L-PBF system and post fabrication treatments; each object is separated from the build platform after the production and is subjected to heat treatment and surface finishing.

v) Material qualification and fatigue testing: parts and sample are tested to evaluate their mechanical properties and investigate the influence of the process on their global characteristics (roughness, hardness)

vi) Final assessment – the evaluation of the results allows to understand the effects of the technology on the fabricated parts and the correlation of the data obtain from the parts and from the samples allow to collect information about the behavior of the parts and develop prediction models.

2.2 Technological partner

Beamit Spa (Fornovo di Taro, Parma, Italy) is a leading provider of high-end metal additive manufacturing (AM) components for demanding industries. They are experts in metal AM and specifically Powder Bed fusion and have multiple certifications and accreditations for their processes and labs activities. Beamit with its 59 qualified PBF systems across Europe in 7 plants serves a variety of industrial sectors, such as aeronautics, space, defense, energy, industrial, motorsport and automotive. Beamit can offer a wide range of metal alloy powders, design services, advanced post-processing and testing options, and expert consulting.

Figure 16 – L-PBF Fabrication systems at the production plant of the company Beamit – Rubbiano (PR) Italy

The long-standing collaboration between Beamit and the University of Parma played a key role in the research activities for this dissertation by providing specimens for material characterization and by manufacturing the actual components that are the focus the present case study.

One of the key benefits of the collaboration was the opportunity to share knowledge and results and the extensive experience of Beamit in the AM industry and its advanced facilities and equipment provided an opportunity to gain hands-on experience in the field of AM.

2.3 Component selection for case study

The practical application of additive manufacturing begins with the identification of the component and its functions. Ideally, a product is investigated using Design for AM (DfAM) concepts seeking improvements, such as multiple part integration, light weighting of existing parts or part redesign for improved performance.

In the present study this part identification phase was driven by i) the relevance to the automotive industry, ii) the safety-critical characteristic and associated dynamic loading conditions in service, iii) the relatively simple geometry considering the planned testing in the laboratory.

The scaled suspension control arm of a commercially available high-performance car was chosen on this case study as the example of part suitable to be produce by L-PBF (Figure 17). The control arm plays a critical role in the vehicle suspension, connecting the chassis, wheel upright, and shock absorber. The original arm was made of high pressure die cast aluminum and experienced variable loading conditions during its service life. Its original geometry was considered promising to be produced by additive manufacturing technology with the aim of improving its performance-to-weight ratio.

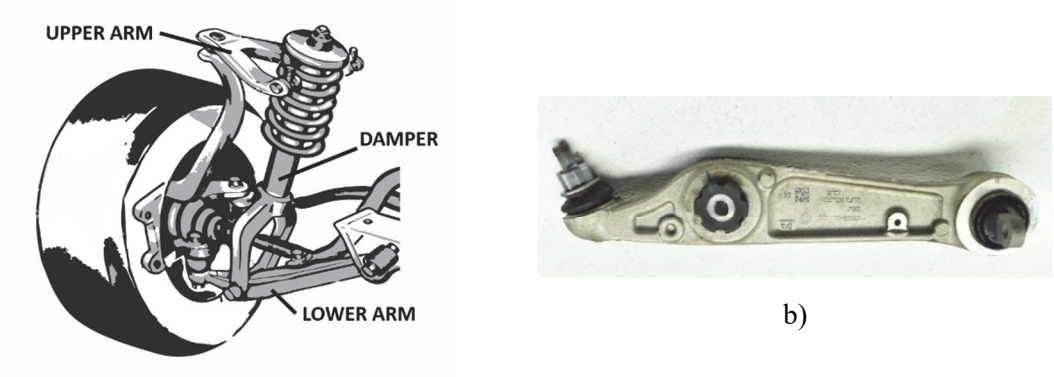

a) b)

Figure 17 – a) Configuration of the suspension lower control arm b) Example of the actual component with a connection point and bushings

The redesign process was conducted with the aim of producing the part using L-PBF process, which enables the production of complex geometries and can reduce the overall weight of the part. To achieve the design goal of this case study, advanced design tools and optimization techniques were selected and applied.

Preliminarily, however, it is essential to conduct a thorough analysis of the working conditions and external loads that the part will be subjected to, including the assessment of the external boundary conditions in term of magnitude of the loads and constraints position; this information will aid in determining the appropriate material, geometries and structural features that will be needed to design the part to meet the required specifications. The suspension arm is subjected to significant dynamic loading in service. As a result, the suspension arm must undergo a fatigue integrity assessment during the design process and subsequent experimental verification.

Parts of this research activity have been published in recent scientific contributions. Specifically, the design and production phases from the digital model to the L-PBF fabrication of the parts were described in [97]; The advantages of the L-PBF technology for the automotive industry in view of lightweight component production were discussed in [98].

2.4 Material selection

To meet lightweight requirements the component will be produced on a L-PBF system using gas atomized AlSi10Mg powder. Aluminum alloys are widely used in the automotive industry because of their high strength-to-weight ratio, corrosion resistance, recyclability, and cost effectiveness. They are used for chassis components and body panels as well as for the majority engine parts to improve fuel efficiency. [99], [100].

Table 1 - AlSi10Mg material composition

Element	Al	Si	Fe	Cu	Mn	Mg	Zn	Ti	Ni	Pb
%	Balance	11	0,55	0,05	0,45	0,45	0,1	0,15	0,05	0,05

AlSi10Mg alloy is the most used Al-alloy for L-PBF production because of its properties:

- Low thermal expansion: This alloy has a low coefficient of thermal expansion, which helps to minimize distortion and warping during the L-PBF process.
- Good thermal conductivity: AlSi10Mg has a good thermal conductivity, which allows heat to be dissipated quickly and evenly throughout the component, reducing the risk of thermal damage.

- Fine microstructure: The alloy has a fine microstructure, which improves its mechanical properties and makes it suitable for use in high-precision parts.
- Good corrosion resistance: The addition of silicon and magnesium to the aluminum improves its corrosion resistance making it suitable for use in harsh environments.

All commercial L-PBF equipment successfully process AlSi10Mg and their manufacturers and service providers include data sheets with properties for qualified materials. The L-PBF equipment and process parameters used for the production of AlSi10Mg specimens and parts of the present study were developed and qualified by Beamit using static mechanical properties as reference.

2.5 Re-Design and Optimization

The front suspension arm is designed with a spherical hinge and cylindrical coupling at its two ends(Figure 17 -b), and a central cylindrical hinge in the middle for connecting to the shock absorber. The loading conditions on the component are like a three-point loading configuration.

Before beginning design and production, it's important to consider factors such as the starting geometry, volume optimization, and the boundary conditions and loads that the part will need to withstand. This includes identifying and defining the specific part that will be studied. In this study, the component has been down scaled to a size (to ½ of original) that can be conveniently produced using a commercial L-PBF machine and tested with available equipment. Simplifications have been made to ensure consistency in load application and control of constraints during testing, which will aid in the analysis and identification of key aspects of the AM design and production workflow. The purpose of these changes is to facilitate the analysis and identification of the most critical aspects of the process.

The objective of this redesign is to modify the original geometry to decrease the weight of the lower suspension arm and to optimizing the stiffness-to-mass ratio. To accomplish this, a structural optimization computational phase will be implemented. This process will aim to make the component lighter, more efficient while maintain acceptable structural stiffness and strength. This can be achieved by using a combination of material property selection and topological optimization. The part redesign will have a positive impact on the overall performance and fuel efficiency of the vehicle.

To simplify the design and make it more reproducible, the spherical hinge of Figure 17-b was removed, eliminating the need to replicate the contact between the socket and inner part. Instead, a circular seat like the one on the opposite side was added, enabling the use of cylindrical

couplings at all three locations. This change was introduced to simplify the fatigue testing phase that was to be carried out using the conventional servo-hydraulic test system in a material testing lab without significantly modifying the component function and the representative loading conditions.

The final geometry of the part subjected to optimization is presented in Figure 18, with the length being 180mm, thickness 18mm, and height 43mm. The part has three holes for fixing, with the two at the ends having a diameter of 22mm (D1) and the one in the center having a diameter of 20mm (D2).

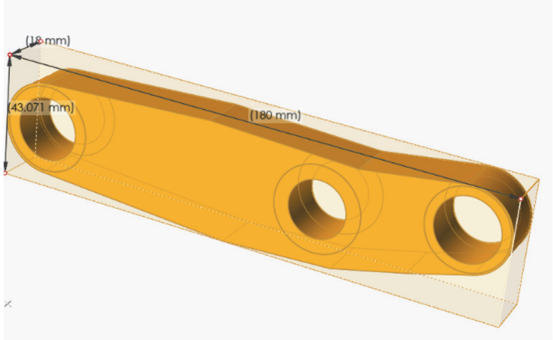

Figure 18 – Geometry of the control arm after defeaturing, simplification of the constraints and geometrical resizing

There are three main types of structural optimization that can be used depending on the chosen design variable and are qualitatively represented in Figure 19. Size optimization aims to improve the size of the individual parts that make up a structure, rather than the structure. Shape optimization aims to find the optimal shape of the component within the design space, rather than changing the size of the parts. Topology optimization targets the optimal distribution of material within a structure while meeting any specific requirements. Each approach focuses on different aspects of the design, and the appropriate method can be chosen depending on the desired outcome and constraints of the project.

Topological optimization is most suitable for creating designs that can be produced with additive manufacturing. It allows to generate the most efficient solution by considering the stress distribution within the part, without being constrained by the limits of traditional manufacturing methods. The result of this optimization can be directly manufactured using 3D printing techniques resulting in parts that are both light-weight and strong. It also enables the creation of unique internal structures and features that are not possible with traditional manufacturing methods, making it a powerful tool to create optimized parts [89], [101].

Topology optimization is a powerful computational tool first introduced in the 1980s by Bendsøe and Sigmund [102], [103]. that has gained popularity in recent years with the evolution of additive manufacturing. The method involves an iterative process of removing material from the part, in order to find the optimal distribution of material within the structure. The process starts with a solid block of material under applied forces and gradually removes material from regions where it is not needed. The goal of the optimization is to find the optimal distribution of material that satisfies specific design objectives, such as for example maximizing stiffness-to-mass ratio of the structure. This approach allows for the creation of parts that are both strong and lightweight and can lead to significant improvements in the performance and efficiency of the final product.

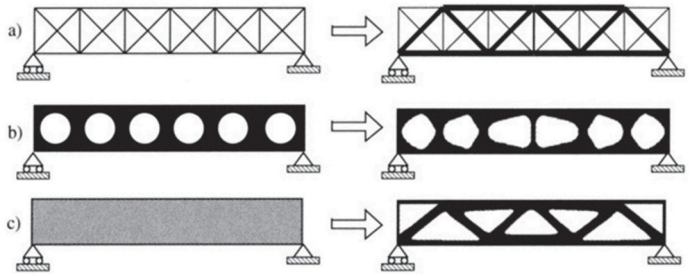

Figure 19 – a) Size optimization, b) shape optimization c) Topology Optimization

The topology optimization activity on the component was performed using ALTAIR INSPIRE software (Altair Engineering Inc.), which is specifically conceived for the design and optimization of structural parts. ALTAIR INSPIRE is a comprehensive suite of tools that includes 3D modelling, structural analysis, simulation, and optimization capabilities. It helps engineers and designers to create and analyze complex designs, test loading scenarios, and optimize product performance. Additionally, the software includes INSPIRE STUDIO, a modelling tool that allows for the re-modelling of the final optimization result with an organic approach, providing more flexibility in reproducing the complex shape resulting from the topology optimization process.

The optimization process begins by separating the total volume of the part into two parts: the design space (DS) and the non-design space (NDS). The DS is the area where the geometry can be modified to find the best possible distribution of material under certain constraints and load conditions, with the goal of reducing mass and increasing weight-to-stiffness ratio. It is important to make the DS as large as possible to give the optimization algorithm more freedom to find an optimal solution. The NDS, on the other hand, is the portion of the model that must not

be altered during the optimization process. This typically includes parts that interface with other members or serve a specific function. Constraints and loads are applied to the NDS instead of directly to the DS.

In the present case study shown in Figure 20-a, the inner faces of the holes have been chosen as the non-design space (NDS). A thickness value has been assigned to these volumes, indicating that they must remain unchanged during the optimization process. The gray areas in the structure of Figure 19 represent the areas outside the design space (DS) where boundary conditions such as constraints and loads are applied. The structure is constrained at its ends by two cylindrical hinges, which allow rotation around its axis but it is restrained in other directions.

The process begins by determining the reference loads that the design must withstand. A load of 5000 N was applied to the central hole, perpendicular to the line connecting the center of the two cylindrical hinges. This load is representative of real conditions and helps to determine how the structure will perform under the specific stress condition..

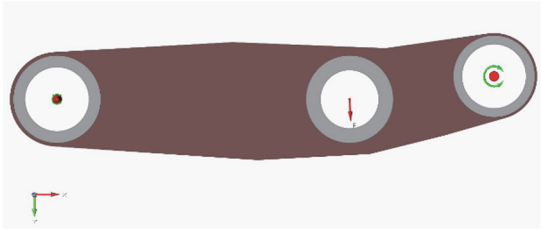

a)

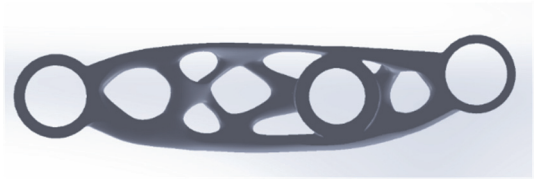

b)

Figure 20 – a) suspension arm with description of DS (red) and NDS (grey) prior to topology optimization using Inspire; b) suspension arm after topology optimization and reconstruction using Inspire Studio

By applying these constraints and loads to the non-design space (NDS) rather than the design space (DS), the optimization algorithm can focus on finding the best possible distribution of material within the design space (DS) while ensuring that the non-design space (NDS) remains unchanged. The optimization process is typically iterative and different designs can be obtained. Figure 19-b shows the selected optimized geometry after application of ALTAIR INSPIRE and

geometry regularization of INSPIRE STUDIO. This is the final design to be 3D printed using laser-powder bed fusion equipment and the procedure the conducted to this solution will be presented in the next section (Figure 20-b).

The proposed design is evaluated in terms of the stress distribution in the component using finite element analysis. Load-induced stresses are compared to material allowables to preliminarily assess the expected component performance with respect to fatigue. This step ensures that the final design not only lightweight but also able to withstand the intended loads. The stress distribution identifies critical locations of the component for detailed assessment. Undesired stress concentration points can be locally redesigned to optimize fillets or geometrical variations.

2.6 •AM Production

2.6.1 Job preparation

After the optimized geometry was determined (Figure 21), the build job is prepared. It means that the number of parts to be produced is defined and their placement within the build volume is carefully planned, to ensure a smooth manufacturing process and high-quality final product. The job preparation determined the best position and orientation of the parts in the build chamber to efficiently exploit the printing volume for multiple parts. This phase also includes determining the location of support structures, which are placed in areas of the part that are at risk of excessive deformation or collapse, often guided by experience or suggestions from software tools.

During the job preparation phase, specialized software was used to determine the best orientation and position of the part in the build volume, minimizing interference, and maximizing the use of space. In this work the job preparation software used is MATERIALISE MAGICS developed by the company Materialise (Materialise NV, Belgium, 3001 Heverlee, Technologielaan). It allowed to prepare, check, and correct 3D models for printing and to define the production details of 3D printed parts. The software is designed to quickly evaluate part orientation and nesting in the build volume, identifying the key surface that would necessitate the incorporation support structures, the estimated construction time for each orientation, the number of supports required for each orientation, and the expected post-processing effort involved in removing supports and achieving the desired surface finish.

An example of a build job containing parts and testing samples is shown in Figure 21 where ten parts oriented vertically on the build platform are identified in red with their respective

supports in blue. Four sets of witness specimens are also included in the build job for simultaneous production and characterization of the fatigue properties and the material anisotropy as dependent on the L-PBF process. The build job shows also additional specimens used for process simulation software calibration.

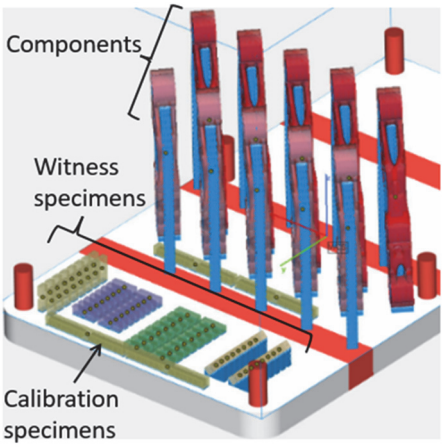

Figure 21 – Build Job representation from Materialise Magics software interface

The user can check the job printability and fix any issues before actual production and simulates the manufacturing process, which enables the prediction of potential problems such as significant distortion, excessive deformation, and residual stress distribution. It helps to understand how the production process may impact the final properties of the part, and identify any potential issues that need to be addressed, in order to produce high-quality parts.

The build job preparation phase and associated numerical simulation tools enables the preliminary definition of process parameters combination to optimize the production process and improve the quality of the final product.

2.6.2 AM Process simulation

Optimization of the manufacturing process parameters considering the specific material and AM equipment available is typically carried out by the service company before offering a qualified process to the customers. This process iteratively adjusts machine parameters and evaluates the results in term of material density (i.e. lack of defects) and material properties (i.e. static mechanical properties via tensile tests). It is typically a time-consuming and costly process due to the need for multiple production runs.

Therefore, L-PBF process simulations can help by allowing for the preliminary evaluation of production results, such as deformations and residual stresses, without the need for actual production runs, thus saving time and money. To effectively optimize the process and contain costs, it is essential to consider not only the cost due the production process but also the unwanted part distortions or part cracking that may lead to part rejection.

Predictions about distortion and internal stress, help in determine the best part orientation minimizing the undesired aspects. Numerical simulation can be beneficial, but it can also be complex and time-consuming due to the large number of material and process parameters involved in the complex L-PBF process. A balance between accurate and detailed simulation results and efficient simulation of large parts is to be found and it involves a compromise between the level of detail and the computational effort.

In this work, the AMPHYON process simulation software was used to simulate the L-PBF processing of AlSi10Mg job. The software, originally developed by Additive Works GmbH founded in late 2015 as a spin-off company of ISEMP, University of Bremen. Amphyon is now supported by Oqton and 3D Systems.

The software is based on the Inherent strain approach and is designed to help users predict and optimize the quality and performance of AM parts, as well as identify potential process issues and design for manufacturability[104]. Specifically, it predicts the mechanical performance of the part obtained by the additive manufacturing process, the part distortion and the residual stresses.

The Inherent Strain Method (ISM) derives from the method developed for determining residual stresses in weld seam[105]; L-PBF similarly to welding involves melting and solidification of a solid material using an energy source. Residual stresses are evaluated from intrinsic deformations of the part calculated by measuring the recovery of elastic deformations.

Figure 22 -a) Amphion process simulation software calibration specimen; b) Method of measuring the deflection of a calibration specimen

The set of specific Inherent Strain for a given material and the specific L-PBF process parameters must be obtained through experiments on calibration samples. The deformation is

determined from the calibration specimens, after their removal from the build platform, see Figure 22-b. This deformation for the given geometry contains information about all parameters used in production, such as material, laser power, scanning speed, scanning strategy, layer height, chamber temperature and how their combination affect the final part properties.

Once the deformation of the calibration specimen of Figure 22 is known, a series of numerical simulations are performed to calibrate the AMPHYON software. The calibration is considered completed when the simulated strain value on the calibration specimen geometry coincides with the measured one and, at this point, the set of IS obtained is saved and used as input for subsequent simulations of print jobs that use the same material and equipment and process parameters. The variation of a single parameter should necessarily be followed by a new calibration procedure. For the present project, the AMPHYON software was integrated into the production workflow to evaluate different component orientation and the impact of their overall position in the build volume. Preliminarily, calibration specimens were incorporated into in the build job and used to evaluate the inherent strains for the used sets of materials and process parameter and after the production, the calibration specimen were removed from the platform and the maximum deflection due to the deformation was evaluated to complete the software calibration. The calibrated software was used to select the solution that best met the production requirements in terms of production time, limitation of deformation, and optimal distribution of support structure material while determining the residual stresses present into the parts.

2.6.3 Fabrication and post processing

After finalizing the design of the part, determining its shape and overall configuration, the production phase began. Components were produced and tested during the experimental phase to gather reliable data and evaluate the structural integrity and fatigue behavior of the AM part. The material used for manufacturing, i.e. aluminum alloy AlSi10Mg, was chosen at the start of the process based on the requirements and intended function of the component.

The actual job production was carried out at Beamit Spa. The equipment used for the production was a modern, high productivity SLM 500 system (SLM Solution GmbH - Germany), (Table 2) that integrates 4 independent lasers of 400 W and it has a machine build volume of 500x280x365 mm3.

The process parameters used for the present production job are listed in Table 3 and define a layer thickness of 50μm, a build plate temperature of 150°C, and an energy density of 32.62 J/mm3.

Table 2 – Technical specification of SLM500

Technical specification of SLM500	
Build Envelope (LxWxH)	500x280x365 mm
3D optics configuration	4x400W
Real Build Rate	up to 171cm3/h
Variable Layer Thickness	20 mm – 90 mm
Minimum feature size	150mm
Beam Focus diameter	80-115mm
Maximum scan speed	10 m/s
Machine dimension	6080x2530x2620 mm

Table 3 - Process parameters for the realization of components and specimens

Production equipment	SLM 500 HL
Laser Power	320 ÷ 370 W
Scanning speed	1000 ÷ 1300 mm/s
Layer thickness	50 µm
Hatch distance	0,14 ÷ 0,20 mm
Build plate temperature	120 ÷ 160°C

Post-processing includes the removal of the parts from the build chamber, removing support structures and applying a heat treatment to achieve the desired microstructure and strength. Internal defects can be eliminated if a hot isostatic pressing treatment (HIP) is applied to the part but the cost is considerable and used only in selected cases, typically in aerospace.

After post-processing, the parts may undergo various inspections to ensure that they meet desired quality standards. These inspections may include checking the dimensions of the parts, visually examining them, and inspecting their surface finish. The surface finishing process is crucial as it helps improve the surface quality of the parts, reduce surface irregularities that could affect their mechanical properties such as fatigue strength and improve the aesthetic and functional appearance of the parts. This process may involve using specialized tooling to smooth the surface, achieve a desired roughness and tolerance. In this study, only the contact surfaces of the optimized parts with pins machined to the correct tolerances. The remaining surfaces were left in the as-built condition.

To investigate the effect of different build directions on the mechanical properties of L-PBF components, a total of 10 optimized arms were printed according to two different directions. Two calibration specimens for the process simulation software were also included in the job. These specimens were printed using the same hatching and contouring strategy and process parameters as the actual parts and underwent the same post-fabrication heat treatment.

Determination of distortion upon progressive separation from the build plate, was used to calibrate material and process parameters via AMPHYON software.

The job was completed with the simultaneous production of 64 micro fatigue samples having different build orientations along with the components. Details of the test methodology will be presented in a later section. These samples were printed and tested to determine the role of build direction on the final surface morphology and fatigue performance. Surface roughness and hardness were also measured on these samples. The fatigue results obtained with the L-PBF AlSi10Mg miniaturized specimens will be presented and used as reference design data in the next section to support the fatigue assessment of the printed components.

2.7 Qualification

Production of L-PBF metal parts is a complex process which has to be preliminarily qualified, in term of equipment, material, process parameters and heat treatments. These properties are typically considered as reference for part design and the qualified manufacturing process ensure that parts will meet the specifications. During serial part production, quality control may periodically verify process stability and required quality of the components.

It is important to qualify the parts, but also to gather information that can aid in future design and predict the mechanical properties of parts. This highlights the need to understand the general operating conditions and factors that affect the final properties of the object being evaluated. When designing structural components, several factors must be considered, such as the shape of the parts, how stress is distributed, the operating environment, and the allowable design limits. These factors establish the reference values for certain properties or characteristics of the material used in engineering design. Concerning L-PBF, there are additional factors to consider to fully comprehend the properties of the final part.

2.7.1 Components testing

The qualification phase in additive manufacturing (AM) is essential for ensuring the best outcome of the production. During this phase, test samples are typically produced alongside the actual parts to verify and qualify the basic properties of the material. These tests usually evaluate hardness, which provides a preliminary overview of the static properties of the material, and microstructural samples to evaluate the quality of the material microstructure and the effectiveness of heat treatment. Gathering more data and information about the mechanical properties and quality of the material during the qualification phase of additive manufacturing

(AM), help to ensure that the production process is optimized and that the final parts meet all the requirements. To fully qualify a part it is recommended to perform full scale testing that reproduces the loading conditions that the real part will be subjected to. This because the relationship between data obtained from sample testing and actual parts may not always be straightforward, and the features introduced in complex structures typical of optimized components may not always be repeatable or investigable with sample reproduction.

For this reason, the presented workflow for design and development of safety-critical parts produced by L-PBF AlSi10Mg culminates with the experimental fatigue testing of actual parts.

A testing setup was designed and experiments were carried out in the material testing laboratory. The fatigue testing was performed using a MTS 810 servo-hydraulic testing machine that had been modified for custom testing.

Due to the high cost and limited availability of the components, three different test configurations were created for each individual component. Initially the testing configuration applied the same force scheme previously used in finite element analysis and topology optimization. After part failure according to the first configuration, the part was re tested under a different configuration to obtain additional data from the same sample. When failure occurred to the modified loading condition, the failed part was tested again according to a third testing mode. In this way three fatigue results were obtained from each printed part thus optimizing data collection vs. resources available.

The first configuration represented in Figure 23-a (Test Configuration 1 - TC1), was based on the original loading conditions of the suspension arm, which involved applying a load at the central hinge and defining two cylindrical hinges at the two ends. This type of load setup is reproducing a three-point bending configuration and is also the loading condition that was used for initial FEA and topology optimization.

The second testing configuration (Test Configuration 2 - TC2) (Figure 23-b) was designed to gather more data from the optimized sample, even though it did not accurately reproduce a realistic condition for this type of component. This testing solution was implemented after the recognition of the first failure mode that occurred on the component. It involved applying a load along the center of the top hinge and the central part reproducing a tensile load to the suspension arm.

The third testing setup (Test Configuration 3 - TC3) was designed to address the issues with the previous testing conditions and was chosen to perform an additional test to gather more information (Figure 23-c). This final test involves applying a tensile load by introducing an

external constraint at the central cylindrical hinge position and applying vertical loading by bringing the steel pin into direct contact with the components.

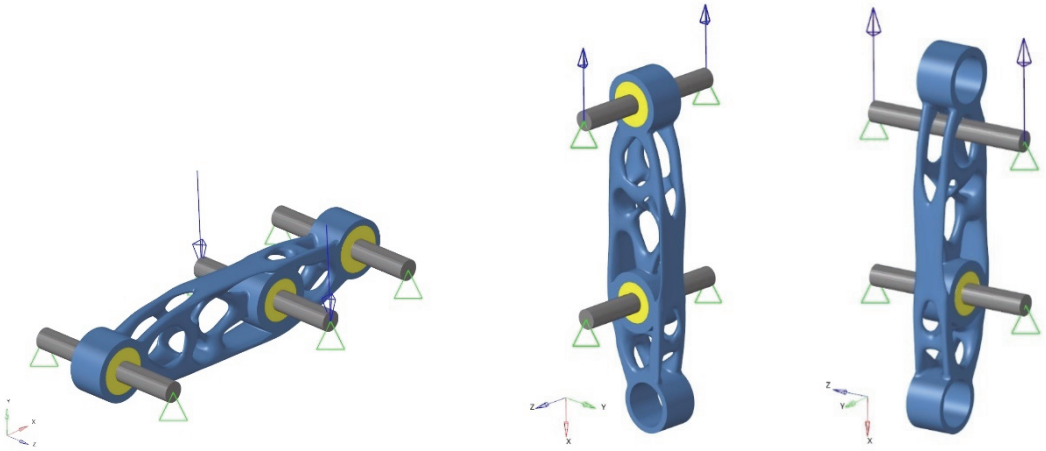

a) b) c)

Figure 23 – Experimental test configurations (TC) of an optimized part. a) TC1 – cyclic 3-point-bending; b) TC2 - cyclic tensile load; c) TC3 – Cyclic tensile load with local contact

2.7.2 Design and Development

The engineering design of structural components involves recognizing the four fundamental dimensions: 1) loading 2) part geometry 3) material and 4) manufacturing technology. Load and geometry are then combined via finite element analysis into the stress distribution within the part. The stress distribution is then compared to design allowables that are specific for the material/manufacturing process combination.

Design allowable are reference values used in engineering design to ensure that a component can withstand the loads and stress it will encounter during its intended use. They are established with material's performance testing and are used as a guide for determining if a part will meet design requirements in its intended application and include yield strength, ultimate strength, modulus of elasticity and fatigue limit for metals.

In the context of L-PBF, it can be difficult to determine specific factors that affect the mechanical properties of a part and particularly in relation with fatigue performance, as these properties are heavily dependent on the process conditions. To understand these properties, it is necessary to identify the key factors that influence them and efficient method to collect information on the material and the effect of these factor are required.

There has been ongoing research in recent years on the development of new testing methods for the evaluation of fatigue properties in metallic materials[[106], [107]] . This research aims at creating new methods and technologies for fatigue testing, with the objective of increasing the understanding of the fatigue behavior of these materials, and to optimize their performance in various applications as well as gathering crucial data for design of the parts to be produced. Traditionally, fatigue testing is done using large-scale samples, but this can be expensive and may not allow for extensive characterization campaigns. This can limit the opportunity to thoroughly test and understand the fatigue properties of materials. One way to overcome this limitation is to use smaller-scale samples, which can provide a similar level of information at a lower cost.

2.7.3 Miniature samples

To qualify the fatigue performance of metals produced using additive manufacturing, a novel testing method based on the use of a prismatic miniature sample loaded in plane bending has been used [81], [108]. A specific geometry has been developed in place of the traditional "dog-bone" standard sample or the traditional "push-pull" hourglass geometry. The advantage of miniaturization comes from the lower production cost and the shorter time required for manufacturing, as well as the ability to print a larger quantity in a single manufacturing cycle, given the same amount of material available.

The specimen has a prismatic shape and measures 22 mm in length, with a minimum cross-sectional area of 5 x 5 mm2 and a 2-mm-radius notch located on the opposite side of the flat surface being tested Figure 24-a.

This method involves using specialized cyclic desktop electromechanical machine to apply alternate bending load typically uses an R = 0 load ratio to induce fatigue cracks on the top surface (Figure 24-b). The relationship between the applied bending moment M and the stress σ that causes fatigue crack initiation in the miniature specimen geometry is established following the analytical beam equation, which states that the stress is linear. The maximum value of σ_n at the top and at the bottom surfaces can be calculated as $\sigma_{n,max} = +/- M/W$, where M is the bending moment measured by the load cell of the test machine, and the sectional modulus is $W = BH^2/6$, with B and H being the width and height of the nominal specimen cross-section, respectively (here B=H=5 mm).

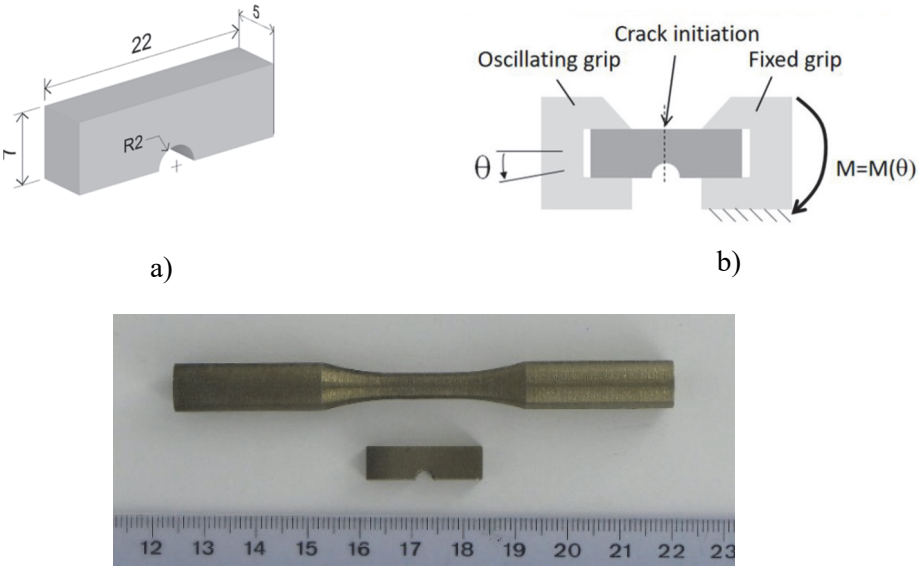

Figure 24 - a) Overall dimension of the miniature sample; b) cyclic plane bending testing of the miniature sample; c) Comparison between the mini-specimen and the standard hourglass specimens used for push-pull tests during experimental activities at ESA

The effective stress distribution in the unsymmetrical minimum cross section of the proposed miniature specimen deviates from the linearity. The elastic stress distribution in the miniature specimen in bending was determined by FEA as reported in Figure 25 -a.

Quantitatively is compared the elastic principal stress distribution in the minimum cross section and the nominal bending stress distribution. This comparison shows that the maximum σ_{FEMmax} on the flat surface is 9% lower than the nominal stress value σ_{NOMmax} (Figure 25 b). Therefore, a correction factor for the miniature specimen geometry $C=\sigma_{FEMmax} / \sigma_{NOMmax}=0.91$ must be applied to the experimental stress value applied to the tested sample.

This method also allows for the investigation of the effects of build direction, surface morphology, and microstructure on fatigue behavior. The small size and prismatic geometry of the specimens enables their free orientation in the build chamber to study of the role of build direction of notches and other complex geometries on fatigue behavior. Despite their small size, they are readily used to characterize microstructure, hardness, and surface roughness. Further, and most important, these samples have been demonstrated to provide valuable information about the fatigue properties of the L-PBF metals[80], [81], [109]. Therefore, this original methodology has been extensively adopted during this research activity to characterize the high cycle fatigue behavior of the L-PBF materials of interest [47], [49], [50].

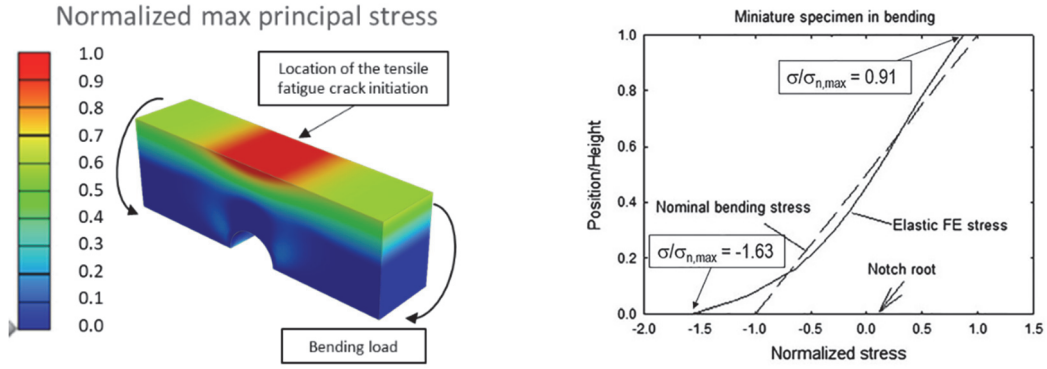

a) b)

Figure 25 - Elastic stress distribution in the miniature specimen under plane bending; a) FEA contour plot with indication of fatigue crack initiation location; b) distribution of the normalized stress along the minimum cross-section

The test method based on the miniature specimens was also employed in the research activity conducted on L-PBF Inconel 718 at ESA. Its versatility in investigating different aspects of the AM technology and the limited material consumption of this approach combined with valuable fatigue data was a strong motivation. The miniature samples allowed to perform an extensive testing campaign, providing valuable information about the properties and behavior of the materials under study; the results of the fatigue tests performed on miniature samples were compared with the results obtained from the testing of standard push-pull samples (Figure 24- c), providing comparable results with considerably lower material consumption .

The miniature sample methodology is particularly useful in situations where it is necessary to test and qualify innovative alloys with limited material available. The low cost of producing miniature samples and the flexibility to investigate different aspects of the material's properties with minimal resource consumption make it well-suited for applications where a preliminary qualification is needed or where only a single aspect needs to be studied without the need for much larger standard samples.

In this study, the directional fatigue strength of as-built L-PBF AlSi10Mg was determined according to the new test methodology and the studied samples are represented in Figure 26. The testing of miniature samples was essential in determining the reference material properties of the present L-PBF AlSi10Mg to be used in the development of a predictive fatigue design methodology that is presented and discussed at the end of the next chapter.

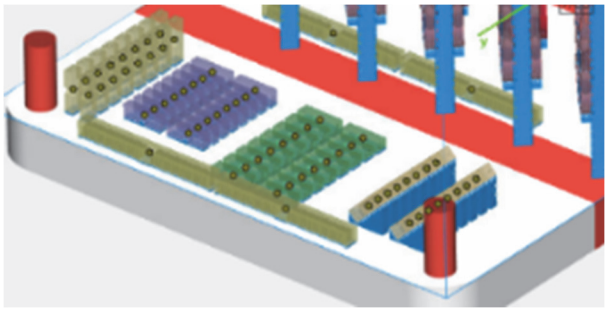

Figure 26 – Miniature samples fabrication for determining the reference material properties of L-PBF AlSi10Mg

2.7.4 Hardness and roughness measurement

Components and samples of this study were characterized before fatigue testing to evaluate the quality of the L-PBF production process and evaluate the results. These investigations included determination of the surface quality and surface hardness to characterize the condition of the final parts and specimens.

In actual practice this kind of testing is used to check the process stability and repeatability. If deviations are observed in the manufactured parts, necessary adjustments of the production process can be rapidly introduced to reestablish the expected outcome.

Rockwell hardness measurements (HRB) were conducted using a 206EX Digital Rockwell Brinell Hardness tester (Affri, Italy) on miniature sample and on components. according to the standard ISO6508[110]. Linear roughness parameters were then measured with a SA6220 contact profilometer (SamaTools, Italy) to characterize the as-built roughness of the samples and the roughness of the component after the sandblasting. Measurements were performed along the longitudinal direction of the miniature specimen applying a Gaussian filter and a sampling length of 2.5 mm according to the ISO4287[111] standard. The main linear roughness parameters collected were: i) arithmetic mean deviation Ra which represents the arithmetic mean of the absolute profile height within the sampling length; ii) maximum height Rz which represents the sum of the maximum peak height and the maximum valley depth of a profile within the sampling length, iii)root mean square deviation Rq which represents the root mean square of the profile height within the sampling length and iv) total height Rt which represents the sum of the maximum peak height and the maximum valley depth of a profile within the evaluation length.

The results of this experimental activity will be presented and discussed in the next chapter.

.

3 Design, production, and testing - Results

3.1 Structural optimization

This section concretely examines all steps of the workflow outlined in the previous section. Figure 15 presents the results of the computational efforts with the different software and of the results of the experimental activities at the component level and the specimen level referring to the framework of the selected case study from the automotive sector: the lower suspension arm.

3.1.1 Topology optimization

The stress distribution of the original lower suspension arm design was investigated using finite element analysis (FEA) to understand how the part would perform under nominal loading conditions. This provided a baseline understanding of the stress distribution in the initial configuration and helped identify areas where the design could be improved (Figure 18).

This initial numerical FE analysis was used to define the assumptions about the boundary conditions, which include the alignment of all holes and the definition of coupling d.o.f. to allow rotation around their own axes and to prevent hyperstatic restraints. A reference load of 5000N was applied in a perpendicular orientation to the line connecting the centers of the two holes at the ends of the component, simulating the response of a suspension shock absorber. The material response, i.e., AlSi10Mg alloy, was assumed linear and elastic using the material properties of Table 4.

Table 4 – Material properties of Aluminum alloy selected to perform the numerical simulation.

Young modulus [GPa]	Poisson ratio	Density [g/cm3]	Yield stress [MPa]
75	0.33	2.77	275.8

The first FEM analysis of the initial component provides an initial understanding of the behavior of the suspension arm and is used to determine if the applied conditions lead to consistent results. The von-Mises stress criterion was used to calculate the static strength of the part, determining the link between the applied load and elastic stress distribution of the part, see Figure 27. The simulation results revealed that the maximum Von Mises stress experienced by the material was 53MPa. Therefore, the component under the reference applied load is far from its maximum load capacity, thus suggesting its design can be improved.

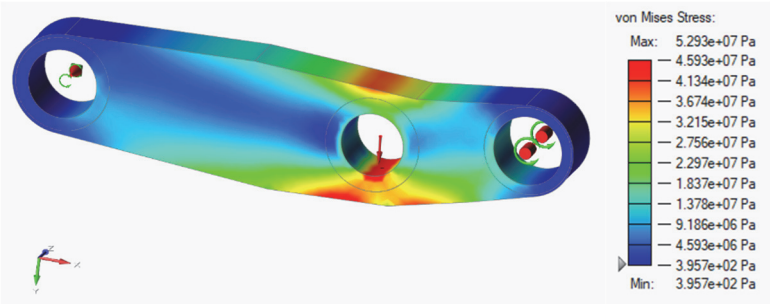

Figure 27 - Von-Mises stress under an applied load equal to 5000N

Structural topological optimization is the process of enhancing the design of a component to effectively handle loads with the goal of creating a strong and lightweight structure that utilizes materials efficiently and can withstand the admissible stresses without material waste. Objectives of the optimization include maximizing stiffness, minimizing mass, or maximizing frequency value, among other possibilities.

Here, the objective was to find the optimal design of the suspension arm that provides the best performance in terms of its strength-weight ratio. The first step in the optimization process was to minimize the mass of the component so as to determine the minimum amount of material needed to support the applied loads while still meeting a minimum safety factor of 1.5 with respect to yield stress. Then the process focused on maximizing stiffness while considering the given mass of the part.

The optimization process was carried out using the software Altair INSPIRE and evaluating several variations with different goals and symmetry conditions starting from the design space given by the original defeatured part geometry. The most significant results of the topological optimization are presented in Figure 28 with an explanation of their characteristics feature.

Three solutions were obtained through optimization with the same boundary conditions but with different symmetry constraints. Solution A represents the topology optimization of the structure with a target of maximum stiffness without defining any symmetry constraints (Figure 28-a). Solution B (Figure 28-b) involves optimization for maximum stiffness with the requirement of respecting a single XY symmetry, and Solution C (Figure 28-c) determines the optimization of the component requiring a double XY and XZ symmetry and a goal of the optimization for optimization of the stiffness.

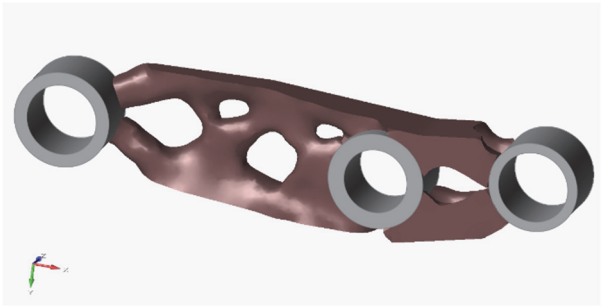

a)

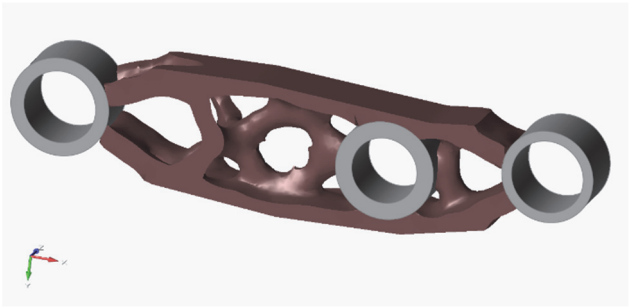

b)

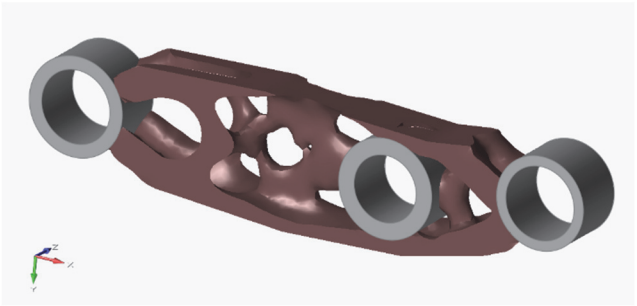

c)

Figure 28- The topology optimization solutions show the design space and optimized redistributed volume, with the goal of maximizing stiffness. a) Configuration A – no symmetry; b) Configuration B – symmetry XY; c) Configuration C, symmetry XY, XZ.

The data reported in Table 5 summarize the results of the topology optimization study of the lower control arm. Solution B and solution C obtained the best performance demonstrating similar stiffness-to-weight ratios and similar topology in terms of volume distributions and final shape. Solution C achieved a higher mass reduction compared to solution B. The results of solution A are comparable to solution C in terms of mass reduction, but the stiffness is not acceptable.

Solution C was then considered the best overall result in terms of stiffness-to-mass ratio. It achieved a significant mass reduction of 53% for the same level of stiffness. The unique shape resulting from the topology optimization is compatible with the L-PBF manufacturing capability.

Table 5 – Results of the topology optimization of the suspension arm with different symmetry conditions with the goal of maximizing stiffness.

ID	Original design	Solution A	Solution B	Solution C
Mass [Kg]	0,248	0,114	0,13	0,116
% Mass reduction	-	54,15%	47,58%	53,14%
Max Displacement [mm]	0,06	0,16	0,11	0,12
Max VM stress [Mpa]	52,93	131,1	73,46	121
Max Principal Stress [Mpa]	50,46	159,6	75,41	78,75
Min SF	5211	2,1	3,75	2,28
Stiffness [N/mm]	84033,61	32010	45455	40161
$\frac{stiffness}{weight}$	337,63	280,48	348,43	344,37
symmetry		none	XY	XY – XZ

3.1.2 Remodeling

The topological optimization procedure generates a raw volume definition due to discrete material elimination. The irregular part geometry is not directly suitable for AM production because the fine detail definition that characterizes L-PBF would negatively impact the mechanical properties of the component. Therefore, it is necessary to perform a remodeling (i.e., smoothing and blending) of the optimization geometry before actual fabrication. The complex "organic" shape, typically the result of topology optimization, cannot be obtained using traditional parametric modeling software.

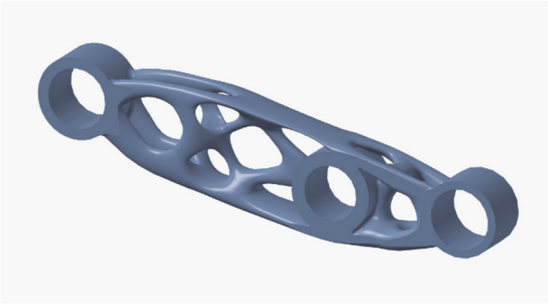

Figure 29 – Final topology optimization solution remodeled using PolyNURBS

The optimized model was therefore redesigned using the "PolyNURBS" functions in the INSPIRE STUDIO design software. This function allows the creation of a new component with

a smooth, continuous surface starting from the optimized but rough part geometry with a controlled transition between the design space and the non-design space. This software makes the original design suitable for AM production. After production, the final weight of the optimized and redesigned component was 0.110 Kg, achieving a final weight reduction of 56%; the final design is displayed in Figure 29.

3.2 L-PBF Fabrication

3.2.1 Job preparation

The job preparation phase involves the definition of the number of parts to be included in the build job in relation to the available print volume that depends on the AM system and the desired outcome of the study. MATERIALISE MAGICS was the software used for print job preparation, including the preparation, analysis, and definition of 3D printing files, as well as the creation of support structures. In parallel, the software AMPHION was used as a process simulation software to support the preparation procedure, allowing for the comparison and evaluation of different solutions in terms of the orientation of the parts in the build volume, with the goal of minimizing deformation and minimizing the support needed for the selected parts, to reduce post-processing operations and the use of support material. The two software were used concurrently to achieve the best possible solution.

The first operation is determining the orientation of the parts. The expected deformations during manufacturing, the production time, the height of the part, and the number of supports needed need to be compared to obtain the configuration that best meets the desired production goals. The simulation was performed based on process parameters defined for the production, comparing the effect of the process on the optimized arm. This process allows the production team to make data-driven decisions in order to produce the best final product possible with the best cost-benefit relationship possible.

Three possible orientations of the part to be produced were considered: Orientation A, orientation B, and orientation C (Figure 30). The effects investigated were on part deformations during production, the time required to complete the printing process, and the number/types of supports needed to sustain the part during production.

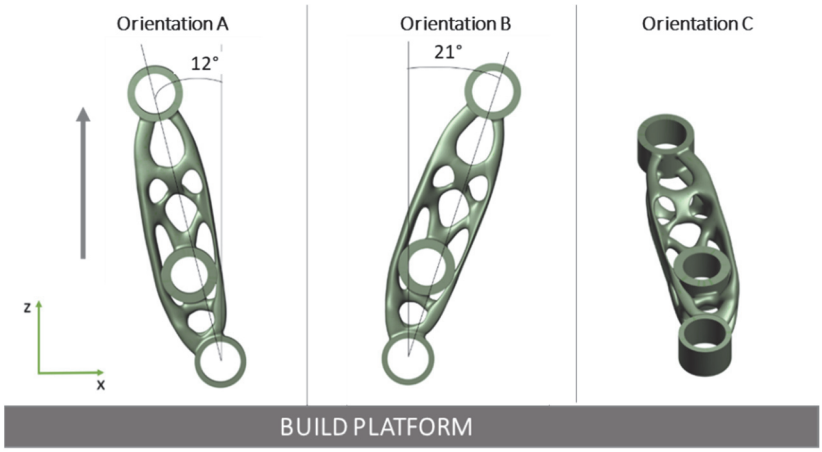

Figure 30 – Three component orientations evaluated during the process preparation to select the best configuration to minimize deformation during the process

Table 6 – Result of the preliminary simulation to select the best building direction using Amphion simulation software

	Max deformation [mm]	Total height [mm]	Fabrication time	Support material [cm3]
Orientation A	0.496	174	High	146,05
Orientation B	0.492	171	High	155,62
Orientation C	1.39	137	Low	50,5

The first orientation (orientation A) is characterized by an approximately vertical positioning of the part, rotated of 12 degrees with respect to the build direction (parallel to the z-direction). The second orientation (orientation B) was suggested as involving minimum deformation by the preparation software and tilted of 21-deg towards the other side. In Orientation C, the part is flat on the build platform, and it is characterized by the condition of minimum required supports and post-processing operations.

Of the three investigated solutions, Orientation A and Orientation B of Figure 30 were selected on the basis of distortion minimization and the best compromise among building time, volume of supports, and post-processing effort, and therefore produced (Table 6).

These two orientations were chosen to investigate the effect of different building orientations on the final properties of the parts. The simulation results provided a detailed analysis of the impact of each orientation on the final product, and the comparison of the different orientations allowed us to make an informed decision on which orientation would produce the

best final product. To create effective supports, manual adjustments to the automatically generated supports are often required. Therefore, the expertise of the technologist was at this stage essential for producing the best support solution.

The print job design included the introduction of witness specimens, that is, the miniature specimens presented in the previous section to be used to characterize the reference fatigue behavior of L-PBF AlSi10Mg obtained according to the same process parameters of the actual components. The limited size and geometrical simplicity favor the fabrication of sets of specimens characterized by different orientations with respect to build direction. Four orientations of the miniature samples, shown in Figure 31, were chosen to replicate the most common surface orientations found on the component.

The different orientations are as follows:

A-: horizontal sample with a flat surface perpendicular to the build direction

B: horizontal sample with flat surface parallel to the build direction

C: vertical sample with flat surface parallel to the build direction

45+: tilted sample with flat surface in the 45° down skin orientation; to reproduce the surface features of the brackets, the 45+ samples will be supported on their flat side to simulate the effect of the support removal operation.

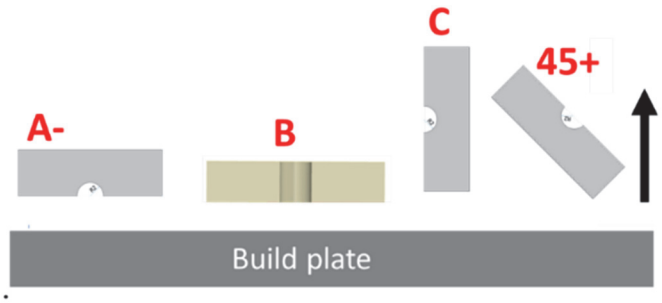

a)

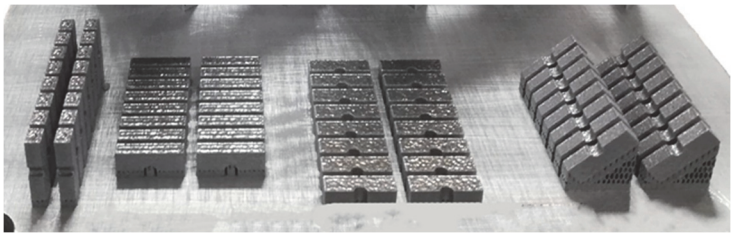

b)

Figure 31 – a) Orientation of the miniature witness samples produced along with the components in the build job. The black arrow represents the build direction; b) Miniature samples fabrication for determining the reference material properties of L-PBF AlSi10Mg

Fatigue testing of A, B, and C miniature samples provided a comprehensive insight into the role of surface orientations on fatigue. Specimens 45+, see Figure 31-b, also characterize the influence of supports after their removal on fatigue strength.

The build job was eventually composed as summarized in Table 7.

Table 7 – Summary of the number of parts and samples produced in the build job.

Summary	Part ID	Quantity
Optimized component	Orientation A	5
	Orientation B	5
Miniature sample	A	16
	B	16
	C	16
	45+	16
Calibration specimen		3

3.2.2 Job Fabrication

The job fabrication was carried out at Beamit Spa on a high-productivity SLM 500 system (SLM Solution GmbH - Germany). The production time for the build job was 39 hours and 35 minutes. However, it included a confidential component of the same material for a customer, which increased the total manufacturing time.

After the production, the build job was cooled down to room temperature and after the depowering phase, all the platform underwent a heat treatment that consisted of direct aging of the produced part to be kept in the furnace at a temperature of 200°C for 4 hours. This treatment is commonly applied to all components made of AlSi10Mg material in Beamit.

Table 8 - Mechanical properties of AlSi10Mg after direct aging heat treatment (Beamit AlSi10Mg datasheet)

Young Modulus [GPa]	77
Yield Strength [MPa]	232
Ultimate Tensile Strenght (UTS) [MPa]	414

Figure 32 - Build job showing optimized suspension arms, miniature specimens, and software calibration specimens after fabrication and prior to separation from the build platform and support removal

The parts were first removed from the build platform using wire erosion, and then the supports were carefully removed with pliers to avoid any potential damage. Upon initial inspection, the components have distinct differences due to their varying orientations and optimized surface structures. The support removal process was done manually and required time and care to ensure the best possible final surface finish. After removing the supports, the components were sandblasted with corundum powder to further improve the surface finish. Figure 33 shows a close view of the suspension arms printed according to the two directions with respect to the building. The distribution of the supports is significantly different and is expected to affect locally the surface quality and possibly the local strength in dependence on different heat flows.

a) b)

Figure 33 – Views of the suspension arms printed according to the two orientations with respect to building direction also show the different distributions of supports.; a)orientation A; b)orientation B

The miniature specimens were not given any additional surface finishing and were kept in their original surface state.

The variation in surface condition between the two geometries is due to Beamit standard procedure of sandblasting the components after fabrication. The miniature samples were left untreated to focus on the as-built condition and adopt a cautious approach for fatigue performance evaluation by examining properties under the worst surface condition.

The static mechanical characteristics of L-PBF AlSi10Mg of Table 8 were determined by Beam-It using dedicated specimens and verified to comply with the reference data of the qualified process. The focus of the miniature samples is the flat surface, which will be tested to determine the material's fatigue strength and how it is affected by the manufacturing process. The surface morphology varies depending on the orientation of the coupons and the layer-by-layer building process. The flat surface of A-samples is characterized by a hatching pattern, and it is apparent that since this surface corresponds to the last layer built, it is directly influenced by the scanning strategy. The flat surfaces of B and C samples are determined by the layer-by-layer process but with a 90-degree difference in orientation. The build direction is parallel to the longitudinal direction of the sample for C and perpendicular for B. The samples built with a 45-degree orientation have a flat surface that is fully affected by the removal of the support structures and the imprecision of the manual removal operation. These samples are tested in their as-built condition without any further post-processing to evaluate the effect of manual support removal on fatigue properties. Figure 34 shows the different qualities of the test surfaces of the four types of miniature specimens qualitatively. Later the characterization in terms of surface roughness will be provided.

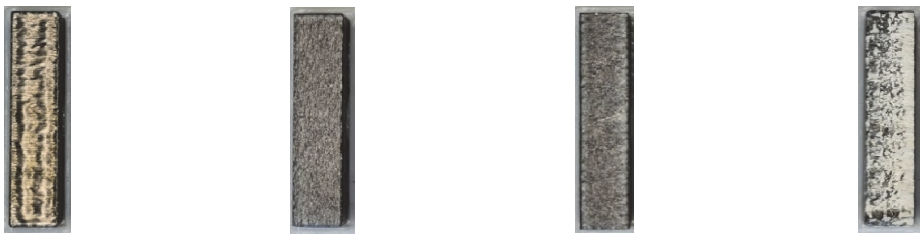

Figure 34 – Flat surface of the miniature samples manufactured alongside the components to characterize the fatigue performance of the material

3.2.3 Process simulation software calibration

The simulation process was updated and re-executed using information obtained from the calibration sample, considering the impact of heat treatment on the final properties and deformation of the calibration sample. This enabled more accurate predictions of residual stress values on the samples and components being examined. To simulate the distributions of residual stresses on the optimized arm and miniature samples, the process simulation software was calibrated, and the Inherent Strain vector was determined by evaluating the deflection of the calibration specimens produced in the same job, including the effects of thermal treatment. The procedure involves printing two calibration specimens alongside the arms, which must be subjected to the same thermal treatment (kept in an oven at 200°C for 4 hours) and then cut and measured to quantify the deflection.

Experimental calibration is the quickest and most efficient way to determine the Inherent Strain (IS) to be used as a starting point for mechanical analysis. This method involves creating a calibration specimen and measuring its strain, which includes information about all the parameters used in the production process, such as material, laser power, scanning speed, scanning technique, layer height, chamber temperature, etc. Once the strain of the calibration specimen is known, a procedure is carried out by running a series of mechanical simulations on the specimen, where the values of IS applied as a mechanical load are iteratively varied. The calibration is considered complete when the simulated strain value matches the measured one on the actual cantilever produced in the job of interest, and at this point, the derived IS set is saved and used as input for future simulations. It is important to note that this method is more reliable when the printing conditions of the calibration specimen are like those of the simulated build job otherwise, a new calibration procedure should be conducted if any parameter is changed.

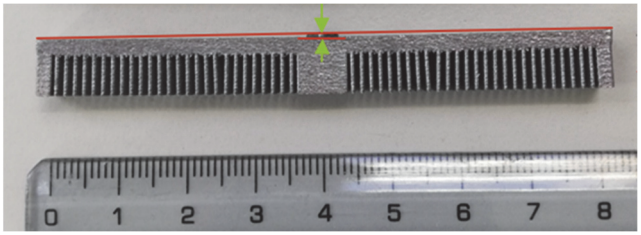

Figure 35 – Cantilever calibration sample manufactured to evaluate the deflection induced by the process after removal from the build plate and for the calibration simulation software

It is also necessary to calibrate the effects of the heat treatment. First, a simulation of an unheattreated calibration specimen is recommended to evaluate the expected tension on the top surface of the specimen before the heat treatment is applied. Then, the heat treatment is simulated by selecting the option that considers the heat treatment before the removal of the specimen from the printing plate and specifying the material properties at the heating temperature and the expected residual stresses. The Young's modulus of the material, evaluated at the heat treatment temperature [112], [113], and the maximum value of the Von Mises stress expected because of the treatment are introduced in the software and the simulation is then launched and the simulated strain is compared to the measured strain. If they do not match, the simulation is iteratively repeated by adjusting the expected Von Mises stress value until the simulated strain matches the measured one.

3.3 Experimental results

Extensive laboratory investigations were conducted to characterize parts and specimens produced using L-PBF AlSi10Mg alloy and the results of this activity are reported here. The experimental characterization was in terms of: i) hardness maps to determine the uniformity of the material strength across specimens and components and ii) linear roughness measurements to quantify the role of surface orientation with respect to build direction since this was expected to play a role during fatigue testing.

Then, specimens and components were characterized in terms of residual stresses. In this case, the residual stresses were obtained by process simulation using the AMPHYON software after a preliminary experimental calibration using the ad-hoc specimens printed together with specimens and components. They are introduced in this section because they depend on the experimental calibration and they are useful in the interpretation of the fatigue test results obtained on components and specimens that are also presented here. It is emphasized that the computed residual stresses in the specimens were confirmed by experimental measurements given in [106], [114].

The most important experiments, however were the fatigue tests of the components using a servo-hydraulic test system and the fatigue tests of the miniature specimens with a dedicated electromechanical test system applying the method previously described (Figure 24). The fatigue test results obtained on the components are the reference data for the validation of a fatigue design methodology to be presented and discussed in the next section. The fatigue test results obtained on the different sets of miniature specimens are the basic material response data used in the fatigue

design methodology to predict the fatigue behavior of the optimized components. This section initially presents all the data obtained on the optimized L-PBF control arms and then all the data for the miniature L-PBF specimens.

3.3.1 Optimized L-PBF AlSi10Mg control arms

3.3.1.1 Hardness

To evaluate the consistency of the 3D printing process in producing items with optimal performance in static conditions, a preliminary analysis was conducted to compare results between the different orientations of the optimized component and the consistency of the process in the height of the build volume. Hardness was measured using the Rockwell B scale and planned to gather data on the part's static characteristics across its height. Results showed good repeatability of hardness in the longitudinal direction for various points on the samples when tested in different orientations. Two components for each orientation were measured, two data points were collected at each measurement point, and the average results were considered for the analysis. The measuring point are reported in red in Figure 37

Based on the minimal variations observed in the two samples, it can be recognized that the manufacturing procedure affects the material properties with respect to the distance from the build platform. A small range of measured values was observed, with component A showing slightly higher hardness in the lower portion of the volume when compared to component B, while the hardness in the upper portion became more similar for both components. However, the values for both components remained within the range of 52 HRB to 57 HRB, as shown in the measurements results described in Figure 36

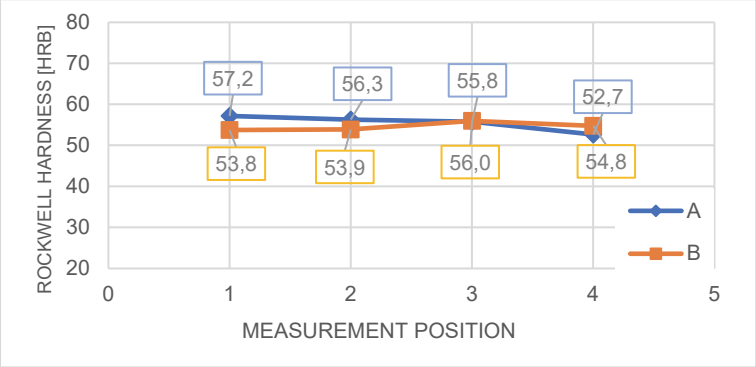

Figure 36 – Surface Hardness distribution along the length of the optimized arm in relation to the build direction.

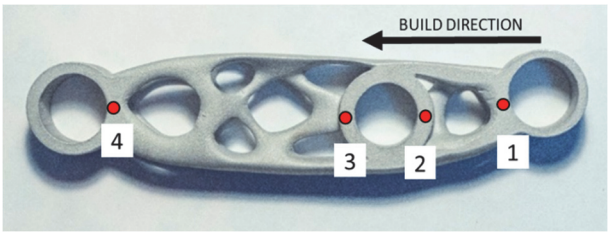

Figure 37 – Hardness measurement location on the optimized sample

3.3.1.2 Roughness of components

The surface roughness of components fabricated using L-PBF is known to be a critical factor that can affect the mechanical properties of the part. Therefore, it is important to investigate surface morphology to understand the quality of the surface finish. In this case, the components were subjected to sandblasting after production. Four positions on the optimized component were measured for linear roughness evaluation to determine the uniformity of the post-process and to see if there were any differences in the different areas of the sample or between the two sample orientations. As shown in Figure 38, four areas of the part were selected for surface roughness evaluation. Positions 1 and 2 were chosen to compare the differences between the two orientations of the components and to investigate any differences related to the position of the surface, which were respectively up-skin and down-skin for component A, and inverted for component B. Positions 3 and 4 were selected to compare the roughness values on a flat surface for the two differently oriented samples and to investigate the differences between the lower and upper part of the build volume. Unfortunately, it was not possible to measure the surface roughness on the surface characterized by the removal of the support structures since they were in areas that were not accessible with the stylus of the contact profilometer used for this investigation.

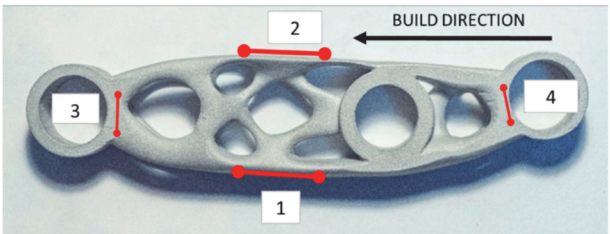

Figure 38 – Optimized bracket with the indication of the areas where linear profile roughness was collected

Table 9 shows that the roughness of the optimized arm is consistent throughout the part, with no significant differences found between areas A and B. This suggests that sandblasting

uniformed the surface of the components. However, without roughness measurements before surface treatment, it is difficult to determine the specific impact of sandblasting on surface morphology.

Table 9 – Linear surface roughness parameters measured on the parts.

Orientation	Position	Ra [mm]	Rz [mm]	Rq [mm]	Rt [mm]
A	1	5,20	14,70	2,22	14,84
	2	4,93	13,93	2,25	14,07
	3	3,83	10,82	1,61	10,93
	4	4,47	12,64	2,59	12,77
B	1	4,28	12,09	1,59	12,21
	2	6,99	19,78	3,43	19,97
	3	4,92	13,91	3,40	14,05
	4	4,63	13,09	2,07	13,22

3.3.1.3 Fatigue tests

Fatigue tests of the optimized L-PBF AlSi10Mg control arms were performed in the laboratory using servo-hydraulic equipment. Each component was evaluated in three different ways to obtain multiple load-life data from a single part. The components printed according to orientation A and orientation B were tested under testing configurations TC1, TC2, and TC3. While test configuration TC1 was strictly related to the service condition of a lower control arm, that is three-point bending; the other two configurations exploited the remaining sound part after the preceding fatigue failure. So conditions TC2 and TC3, while not representative of a lower control arm application, are however relevant for linking the complex geometry of an optimized L-PBF AlSi10Mg component to a specific loading condition, failure mode, and fatigue life.

To guide the definition of the experimental loading conditions, elastic FE analyses were preliminarily carried out for the three loading modes using the commercial HYPERMESH software. Simulation of the different test setups ensured that results accurately reflected actual complex test conditions and identified areas of high stress and potential failure points. The FE analysis improved the understanding of the structural behavior of topologically optimized geometries.

From the simulation standpoint, loads were applied to the component through steel pins connected to the loading rig of the testing machine. To ensure that the load was transferred correctly from the pins to the actual part, nylon bushings were positioned to couple the pin and the cylindrical boundary of the arm, see Figure 39.

The cylindrical steel pins were modeled assuming an elastic modulus of 210 GPa. The nylon bushings that were inserted between the component and the pins to ensure an accurate transfer of the load were assumed to have an elastic modulus of 3 GPa. The contact interface was modeled between the component and the bushings and also between the bushings and pins.

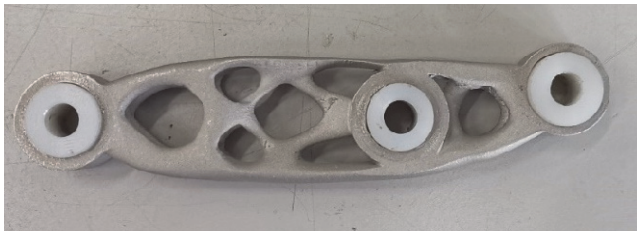

Figure 39 - Optimized component prepared for fatigue testing with nylon bushing positioned inside the part.

The FEA mesh was developed using tetrahedral elements with an increased density of elements in the portions of the components close to notches or small radii of curvature. This helped to ensure that the simulation captured the behavior of the component in these critical areas with a higher degree of accuracy. The use of tetrahedral elements also allowed for a more accurate representation of the geometry of the component, making the simulation results more reliable. The constraints and forces were applied to the ends of the steel pins, and the degrees of freedom were assigned to ensure the appropriate displacements of the part. The reference applied load of 3000 N was used to perform the numerical simulations. Elastic stress distributions associated with other load levels could be predicted using a linear relation.

The relevant FEA results for the three-test configuration TC1, TC2 and TC3 are now presented with potential failure locations identified as M, U, S1, and S2.

Location of fatigue crack initiation and reference local stress

Testing Configuration 1

Testing configuration 1, also known as TC1, represented the original loading condition of the parts and was the same used during the optimization process to achieve the best response to the applied load. The configuration closely resembles a three-point bending setup, with constraints at the extremities of the component and a vertical load applied in the middle. This configuration (Figure 40) is used to simulate a loading scenario where the component is supported at both ends and loaded in the middle. The arm was mounted on the servo-hydraulic system, with nylon bushings inserted between the aluminum geometry and the steel pin. The numerical

simulation model replicates the experimental setup precisely, with a 3000N force split and applied to the central pin on the two external sides. The load is applied perpendicular to the line connecting the center of the two circular extremities. The degree of freedom allows movement along the x-axis to avoid over-constraining the structure. The interaction between the bushing, steel, and component is modeled without any initial pre-load.

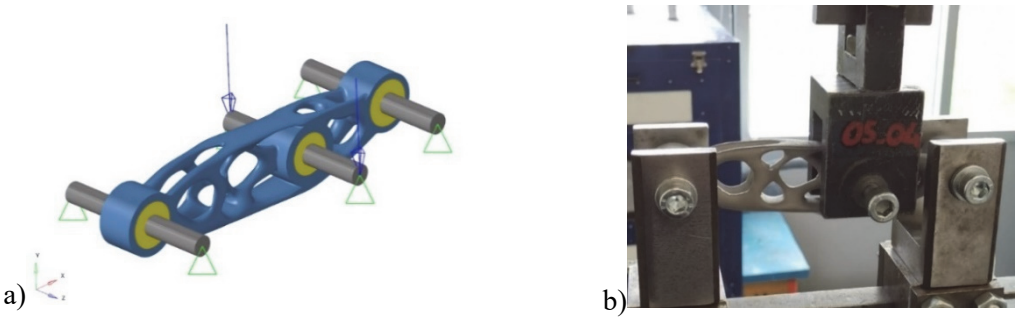

Figure 40 – First testing configuration: three-point bending. a) numerical simulation model with the definition of load and constraints; b) experimental setup for TC1

The contour plot of the principal stress distribution (Figure 41) for testing configuration 1 (TC1) shows that the highest stress points are located near the fillet connecting the optimized volume of the component and the non-design space (location M). This feature creates a stress concentration point where the highest stress values are recorded. Although the loading condition is symmetric, the principal stress peak values are similar but not identical due to the slight asymmetry introduced by the manual remodeling of the topologically optimized volume. For analysis and comparison with experimental results, the highest stress value of 228 MPa was considered.

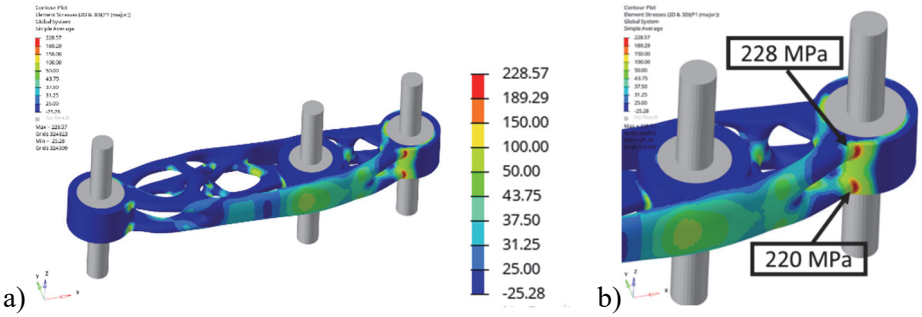

Figure 41 – Contour plot of the principal stress distribution for testing configuration 1 (TC1) the critical point in position M. a) contour plot of the tested components; b) detail of the contour plot with identification peak stress point.

Testing configuration 2

Testing configuration 2, also known as TC2, is an additional test setup used to evaluate the fatigue behavior of the components after they fail under TC1. This configuration (Figure 42) simulates a tensile load applied to the parts by vertically positioning the component in the testing machine. Although this type of loading is not theoretically appropriate for this type of topology, it is useful for obtaining additional information about the material and design. The arm was attached to the testing machine to assess the component with TC2. Nylon bushings were inserted between the aluminum geometry and the steel pin to transfer the loads.

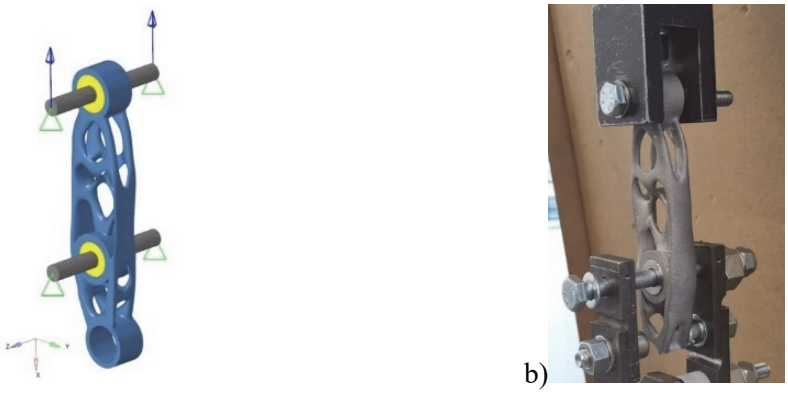

a) b)

Figure 42 – Second testing configuration with vertical tensile loading. a) numerical simulation model with the definition of load and constraints; b) experimental setup for TC2

The numerical simulation model replicates the experimental setup for TC2, where a force of 3000N is split and applied to the top pin, loading the component in a tensile configuration (Figure 43). The lower steel pin is constrained, and the degree of freedom of the top part allows for displacement along the vertical axis, parallel to the longitudinal direction. The contour plot of the principal stress distribution for TC2 shows four major stress concentration points, which are located near the fillet connecting the optimized volume of the component and the non-design space.

The most stressed areas are on the S1 side with the highest stress value equal to 167 MPa and used for the analysis and comparison with experimental results. On the S2 side, the most stressed area is located near the blended notch, which connects the optimized portion of the component with the non-design space. The highest principal stress value of 150 MPa was used to evaluate the component under TC2

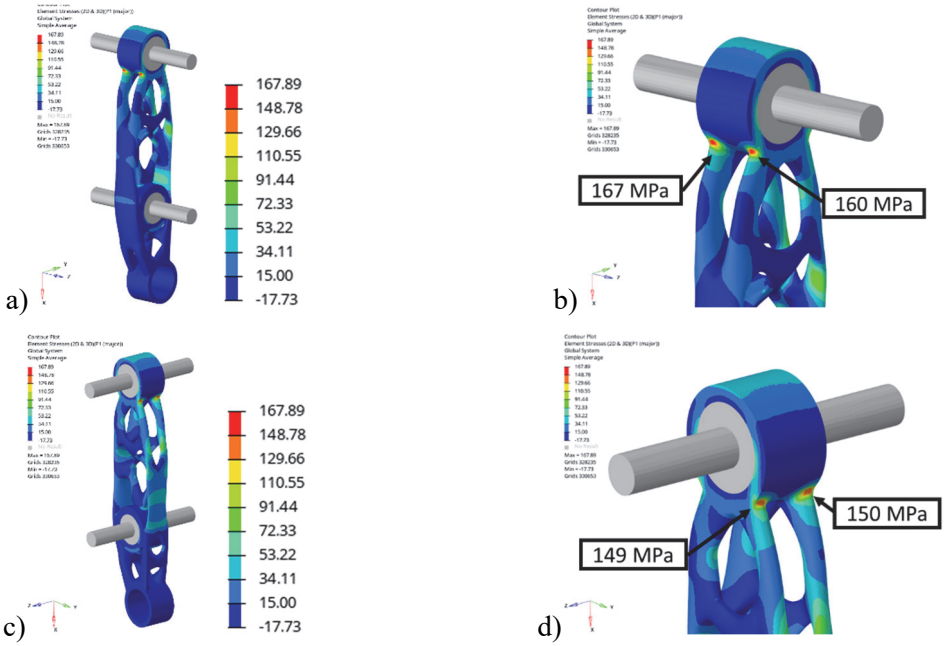

Figure 43 – Contour plot of the principal stress distribution for testing configuration 2. (TC2). The critical points are in positions S1 (a – b) and S2 (c-d).

Testing configuration 3

Testing Configuration 3 (TC3) was established to acquire additional experimental data about the fatigue properties of the component (Figure 43). A setup similar to TC2 was used, but with a steel pin directly in contact with the aluminum component. One major concern with this configuration is the possibility of contact stress occurring between the two materials. The finite element (FE) model replicates the experimental setup for Configuration 3, where the force of 3000N is split and applied to the top pin, loading the component in a tensile configuration. The lower steel pin is constrained, and the degree of freedom of the top steel is a translation along the vertical axis.

Figure 44 - Third testing configuration with vertical tensile loading and contact between the component and the steel pin. a) numerical simulation model with the definition of load and constraints; b) experimental setup for TC3

The contour plot of the principal stress distribution for TC3 shows four major highly stressed areas located on the thinner sections of the optimized structure on both the external and internal sides of the truss. The stress was identified as slightly higher on the internal side (Figure 45 c-d) and similar but slightly lower on the external side of the component (Figure 45 a-b); for the planning and the correlation of the experiments, the overall highest stress value of 98 MPa was considered due to the observed limited differences.

The peak stress values evaluated from FEA with a reference load of 3000N were identified for each testing configuration and reported in Table 10. The maximum stress value determined in the numerical simulation was used to determine the different load levels at which the fatigue test was carried out.

In conclusion, the FEA of the three testing configurations identified four critical locations where fatigue crack initiation is expected. Table 10 and Figure 46 summarize the points identified for the specific TC and the peak stress at 3kN.

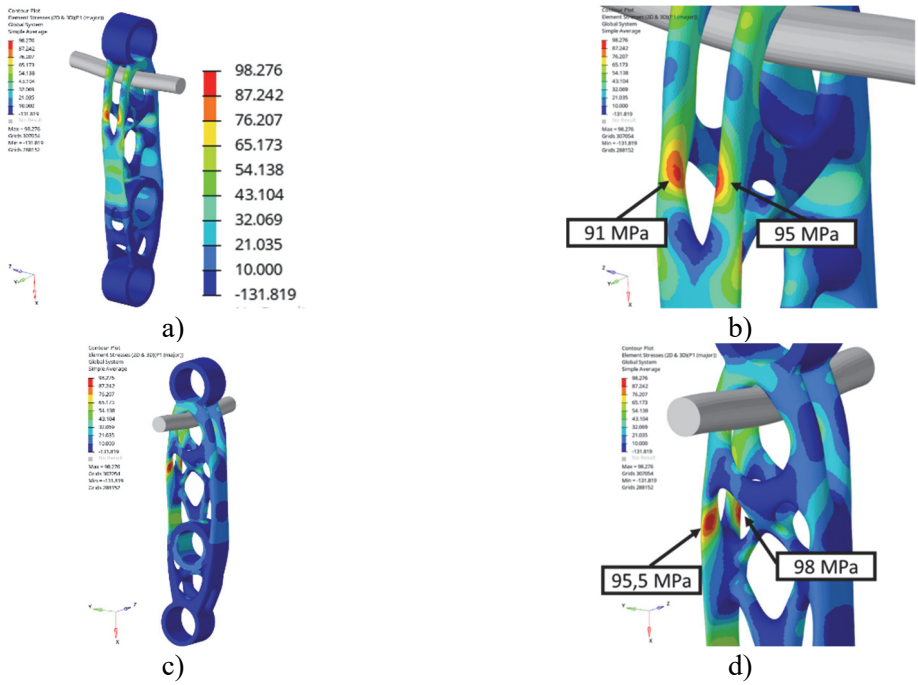

Figure 45 - Contour plot of the principal stress distribution for testing configuration 3. (TC2). The critical points are in position U with distribution peak stress values on the external side (a – b) and on the internal side (c-d), but with limited differences.

Table 10 – Position of the peak stress related to the relative testing configuration and principal stress value determined by an applied load of 3000N evaluated with FEA

Peak-stress location	Test Configuration	σ_{FEA} [MPa] @3kN
M	TC1	228
S1	TC2	150
S2	TC2	167
U	TC3	98

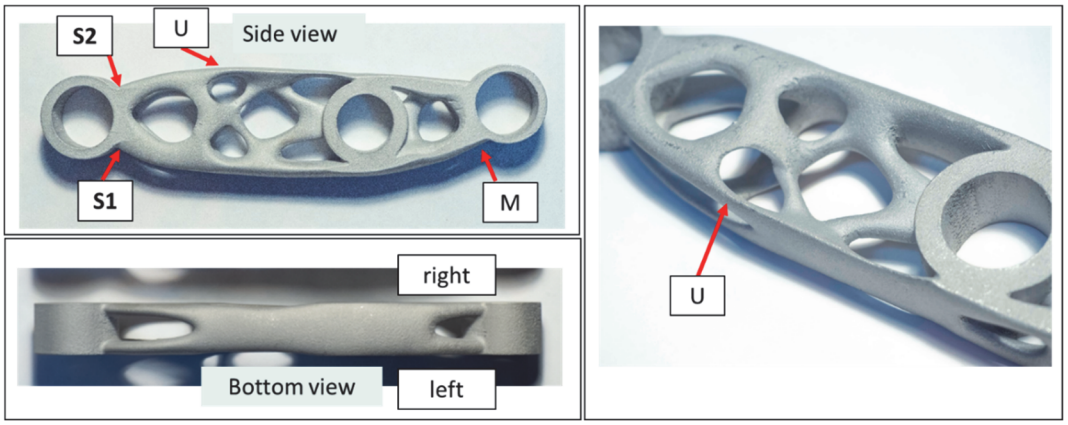

Figure 46 – Optimized arm with the indication of the higher stressed point for each loading configuration and where the failure occurred

3.3.1.4 Fatigue tests of components

The fatigue behavior of the parts was evaluated by testing the components and reproducing the service load. This was done at the University of Parma's laboratories, where three different testing configurations were used to gather as much information as possible about the component's performance. The fatigue tests of the components were performed at an experimental stress ratio of R = 0.1 and a test frequency of 5 Hz. The run-out, which represents test interruption without failure, are identified in the plots with arrows. This information allows an understanding of how the component performs under different loading conditions, how many cycles the component can survive before failure, and what critical areas of the component are more likely to fail. The tests were performed on each component starting from the original service condition, represented by Test Configuration 1 (TC1). Three samples were tested for each orientation, and the failure point was always identified as the location where the highest stress was observed with numerical simulation, which is point M, corresponding to the blended notch root under the right pin coupling. After the failure of the component under the first testing condition, the testing setup was switched to the second configuration, Test Configuration 2 (TC2), to collect additional

fatigue data. The numerical simulation of TC2 identified two different critical locations with high stress, S1 and S2, where the crack occurred at a blended notch root under the top pin coupling. After the completion of the second testing option, the final configuration was established to acquire additional information by loading the remaining material to determine another stress distribution. Test Configuration 3 (TC3) allowed identifying failure positions that were far from the critical notches. The results of the fatigue testing are reported in Table 12 and plotted in semi-log S-N curve in Figure 47.

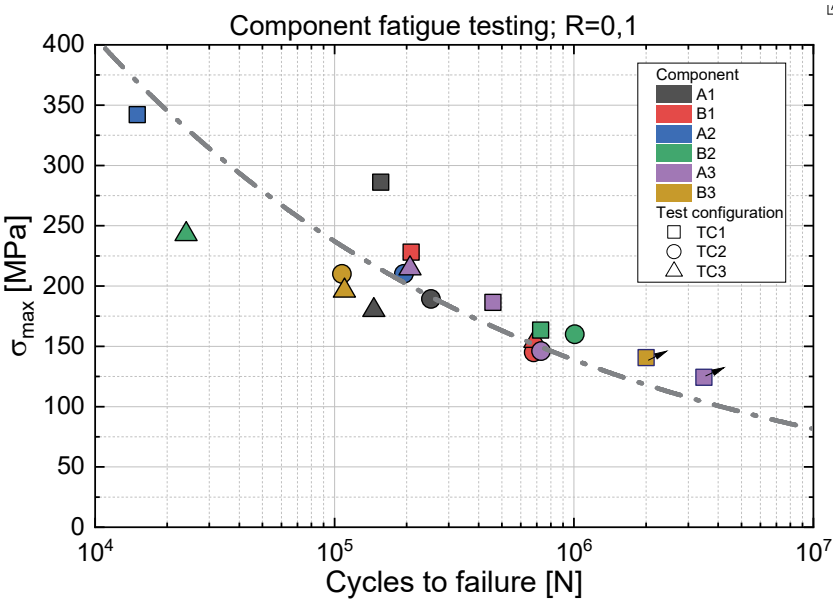

Figure 47 - Fatigue behavior of A and B components on the different testing configurations.

To generalize the experimental results, the data for each individual set were interpolated using the power law relationship of the type.

$$\sigma^b = N * A$$

By means of the least square method (ASTM-E739) and the statistical estimation of the parameters for the linear model log(N) = log(A) + b log(σ) obtained and reported in Table 11.

Table 11 - S-N power law coefficients and exponents experimental fatigue strength at 2 10^6 cycles

log(A)	b	R2	Number of tests	Estimated fatigue strength at 2 10^6 cycles [MPa]
15.14	-4.27	0.72	18	130/140

Table 12 – Summary of the fatigue test performed on the optimized component at R=0,1

Specimen ID	Test Configuration	Crack initiation Point	Max Experimental Load [N]	Nominal stress s11 @crack initiation point	Cycles to failure
A1	TC1	M	3763	285,9	156000
	TC2	S1	3400	189,2	252900
	TC3	U	5506,9	179,9	146000
B1	TC1	M	3000	228	209000
	TC2	S2	2900	145	678730
	TC3	U	4722,7	154,3	686916
A2	TC1	M	4500	342	15000
	TC2	S1	3774	210,1	195000
B2	TC1	M	2150	163,4	725777
	TC2	S2	3200	160	1008000
	TC3	U	7434	242,9	24000
A3	TC1_step1	runout	1634	124,18	3488500 →
	TC1_step2	M	2452	186,35	459000
	TC2	S1	2622	145,96	728782
	TC3	U	6566	214,49	206795
B3 B3	TC1	runout	1850	140,60	2000000→
	TC2	S2	4200	210	107400
	TC3	U	6000	196,00	

The R-squared parameter of about 0.72 indicates that the model fits the data well, but other factors that influence the dependent variable need to be included and considered in the model.

It is apparent that the scatter in the stress values is greater when they exceed the yield strength of the material. This may suggest that plasticity is present in the component, which could result in a different fatigue response that needs to be considered when interpreting the results of the model. The experimental fatigue strength of the aluminum components was determined to be around 130/140 MPa, and the position of the failures corresponded to the highest stress position identified by the FEA for all the tested parts.

The local FEA stress vs. life plots of A and B components show similar fatigue behavior. But the results from testing on various configurations revealed the importance of conducting multiple fatigue evaluations and experiments. The manufacturing process has a crucial influence on the fatigue life of the parts and the location where fatigue cracking occurs.

Both A and B components failed at the same location when subjected to Test Configuration 1 or TC1, i.e. close to the blended notch root at the right pin coupling (failure location M). The indication of the position and optical observation of the fracture surface is reported in Figure 48.

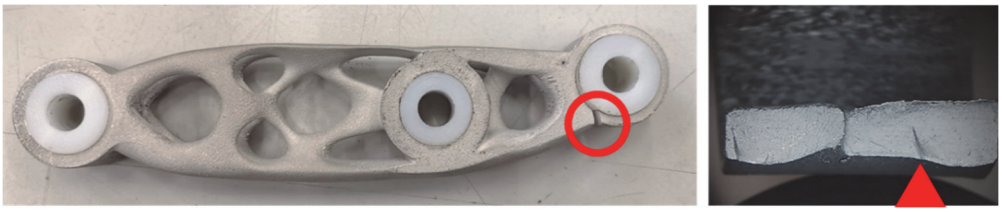

Figure 48- Component A1 tested at TC1 and identification of the failure location at M critical point and fracture surface

When tested under Configuration 2 (TC2), different crack initiation points were identified for orientation A and orientation B.

a)

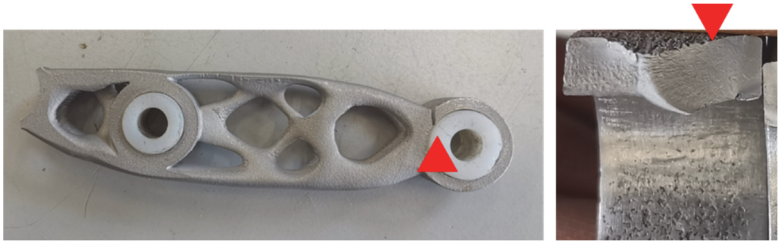

b)

Figure 49 - Components tested at TC2, identification of the failure location, and optical observation of the fracture surface. a)Component A1 with failure location at S1 critical point; b)Component B1 with failure location at S2 critical point

All the Orientation A components failed at the S1 position (Figure 49-a), while orientation B components failed at the S2 position (Figure 49-b),. This evidence is relevant because it demonstrates that the slightly different geometries of components A and B induce different failure patterns and different fatigue lives despite being subjected to the same loading condition.

Component A is tilted towards the S1 side (Figure 33-a), thus requiring support structures near the critical S1 location. Their presence is associated with a rougher surface morphology upon support removal compared to unsupported surfaces and the creation of small local defects, which act as a crack initiation point for A-oriented parts.

Components B, on the other hand, were fabricated when tilted towards the S2 side, thus determining a similar situation on the opposite side S2 (Figure 33-b), which proved more critical for component B. The common point of fracture propagation in both A and B components indicates that the defects causing fracture originated from the supported areas.

The experimental crack initiation point of components tested at TC3 confirms the FEA predictions that a high-stress area of the component is most critical. The failure occurs on the thinner portion of the optimized structure (Figure 50).

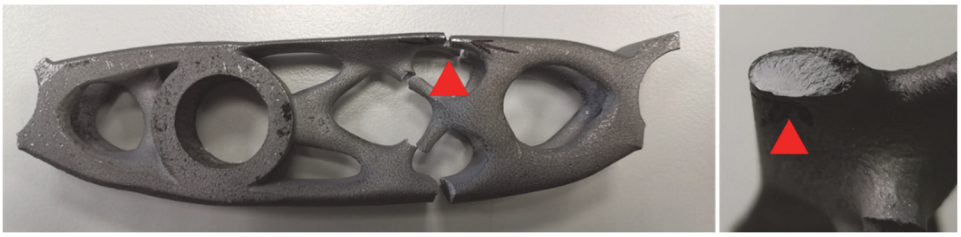

Figure 50 - Component B1 tested at TC3 and identification of the failure location at U critical point and fracture surface

The identification of the precise point of failure helped to evaluate the accuracy of the numerical model and to correlate the results of the experimental activities with the expected critical peak stress position. Additionally, it allowed us to identify where the material failed and understand the reasons behind it. Furthermore, this information is crucial for the design optimization process, as it can help to identify areas of the component that need to be strengthened or modified in order to improve the performance. By comparing the location of the failure to the predicted stress concentration points, it is possible to evaluate the effectiveness of the topology optimization process in addressing these critical areas. Overall, the correlation between the numerical model and the experimental results provides valuable insights into the strength and durability of the component and can inform future design decisions. This information can be used to improve the mechanical properties of the component and to validate the simulation results by comparing them to the experimental data. Further examination in SEM would define more clearly the quality of the crack initiation points.

3.3.2 Residual stresses in the components

To understand the impact of different orientations on the final properties, the residual stresses on the component were evaluated for the two directions. Residual stresses are considered crucial in

additive manufacturing because they can affect the final behavior and performance of the part. Heat treatments may not always be sufficient to address this issue, so it is important to consider residual stresses when characterizing the mechanical properties of the part. To compare the stress distribution between the two orientations, the residual stress was evaluated using the software Amphion's term of stress component, which helped in obtaining the stress distribution for orientations A and B. The overall outcome of the simulation performed with Amphion simulation software is the distribution of the residual stress with the highlight of the more affected part of parts and the identification of the portion of the component that is characterized by the higher deformation.

a) b)

Figure 51 –Displacement of the components after production; a) Orientation A; b) Orientation B

Based on the simulation results reported in Figure 51, it appears that the oriented A samples do not experience significant deformation. The highest estimated deformation is 0.121 mm, which is relatively low compared to earlier evaluations for the orientation definition. This may be due to the stress reduction from heat treatment and the optimization of supports during the manufacturing process. The results of the process simulation for component B are reported in Figure 51-b. The strain evaluation for orientation B does not show any critical aspect and is consistent with the results for orientation A.

By extracting the x, y, and z stress components at each node, it is possible to gain a deeper understanding of the distribution of residual stress and the stress components that have the most influence on fatigue response. This allows for the selection of the most relevant stress component, which was found to be parallel to the built direction and the Z axis and parallel to the stress direction of the load applied during testing.

CLOUDCOMPARE, an open-source software, was utilized to manage the results obtained from Amphion, which were exported in terms of node coordinates and local stress values. The point cloud generated by this process was then further processed to visualize the specific stress values for the chosen stress component. This allowed for the examination of the distribution of the stress values in the desired direction and provided a better understanding of the local stress distribution in the direction of the applied load during fatigue testing. This helped to identify areas of high stress and potential points of failure.

The focus is on the critical location of the sample, which exhibits the highest structural stress according to the finite element analysis. The distribution of residual stress was examined at the specific points (M, U, S1, and S2) for both orientations, and the numerical values are reported in Figure 52. The different orientations of the components in the build chamber result in a different distribution of residual stress in these locations. Additionally, the left and right sides of the same oriented components also have different values, likely due to the asymmetry of the part and variations in meshing accuracy.

However, since the values are similar and it is necessary to consider a standard deviation when evaluating residual stress, the average value is used for further analysis. The results of the measurement are reported in Table 13, with a standard deviation of 20 MPa considered.

Table 13 – Residual stress distribution on critical location for Component A and B evaluated from process simulation.

Component	Position	$\sigma_{res-left}\ [MPa]$	$\sigma_{res-right}\ [MPa]$	$\sigma_{res-mean}\ [MPa]$ ±20
A	**S1**	41	31	36
	S2	41	39	40
	U	51	42	46.5
	M	26	23	24.5
B	**S1**	57	45	51
	S2	45	51	48
	U	49	46	47.5
	M	32	31	31.5

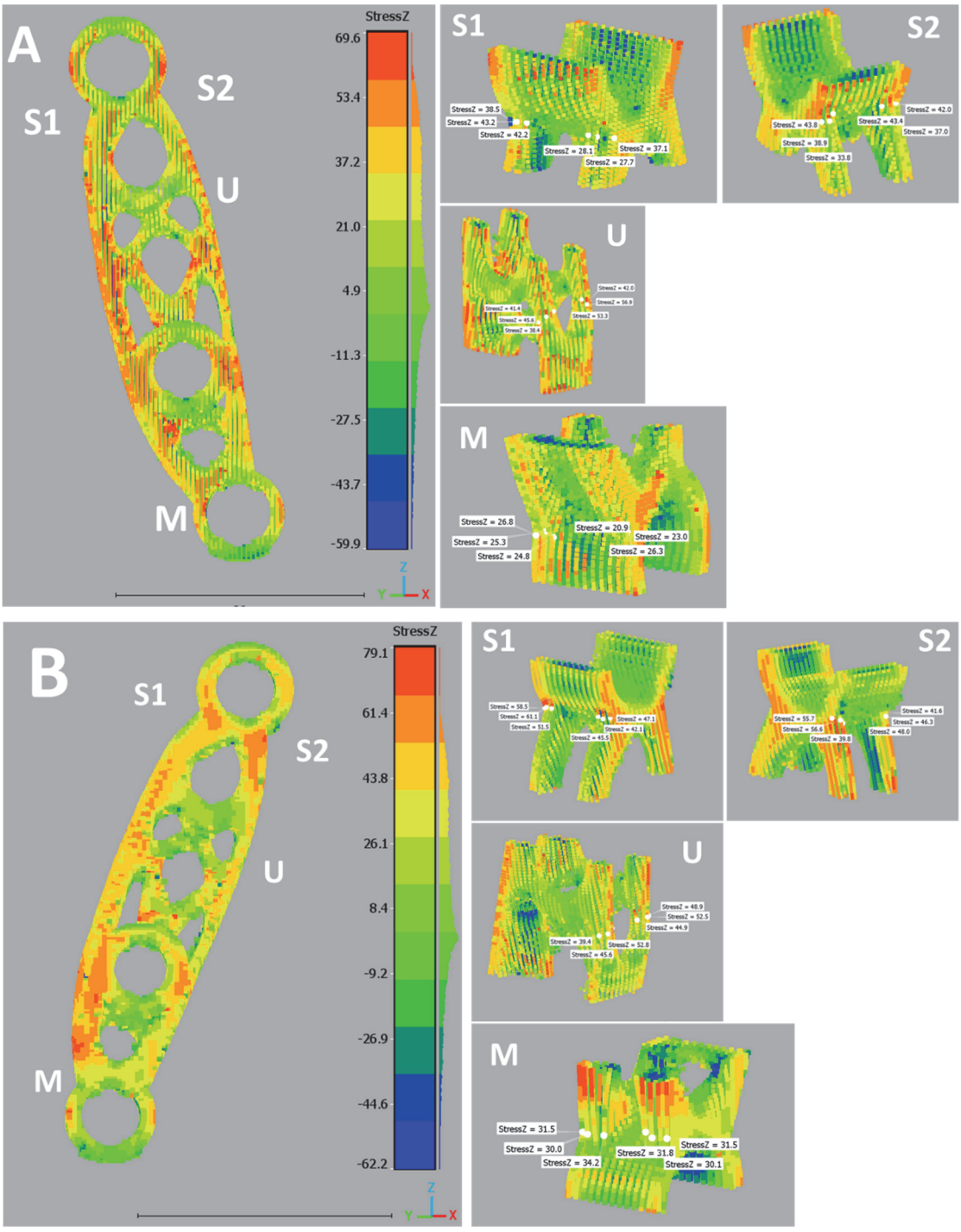

Figure 52- Residual stress distribution evaluated on optimized component using process simulation software Amphion. The stress direction reported in the contour plot is Z parallel to the build direction.

3.3.3 Miniature L-PBF AlSi10Mg specimens

Beyond the traditional methodology for characterizing the fatigue performance of L-PBF metals, it is important to keep in mind that many influencing factors can affect the final properties of the produced part, and the process itself can determine characteristics that lead to different material responses. In the case under examination, AlSi10Mg aluminum alloy was selected for production, and the part underwent specific post-process heat treatment.

However, the final properties of the parts produced with L-PBF are characterized by different aspects that, when combined, describe the final behavior of the part; the superposition of the effects introduced by surface morphology, material microstructure, and defect distribution is complex and would require an extensive characterization campaign to recognize and correlate the various factors that are playing a role in describing the final mechanical properties.

To qualify the basic material properties independently from the actual parts, witness samples were produced alongside the components during the job; gathering information regarding the mechanical fatigue properties of the material using the mini specimens is critical to validate the methodology and gather as much information as possible regarding the major influencing factors governing the fatigue life of the material.

The miniature sample methodology was selected because of the possibility of obtaining a significant amount of information with limited material consumption compared to standard fatigue sample dimensions. Additionally, the small volume of the coupons allowed for freely orienting them in the build chamber and investigating the influence of the build direction on the mechanical properties of the part.

Characterizing the material properties and the mechanical performance using representative samples instead of performing that activity on real parts is useful to have the chance to obtain more generalized information independently from the final shape of the specific component. This allows to recognize in the samples the information that can be transferred to the actual part in relation to the specific local properties and finally be able to properly design an L-PBF part taking into account the most critical aspects and forecasting the performance of components in relation to the local properties.

On the miniature samples, a variety of tests were conducted to assess the surface morphology of the specimen, as well as the impact of the process on the differently oriented flat surface. Specifically, roughness measurements were performed to gain insight into the surface roughness, while hardness measurements were conducted to obtain information about the static

mechanical properties of the material. All of these tests helped to provide a comprehensive understanding of the material's behavior under different conditions.

3.3.3.1 Roughness

The first parameters evaluated on the miniature sample were the linear surface roughness parameters measured on the flat surface. These were compared to observe differences and anisotropy caused by the production process. The surface morphology of the A-oriented samples is described by the scanning strategy and the wavy pattern introduced by the scanning strategy (Figure 34) and exhibited the lowest surface roughness value among the other orientations. B and C orientations exhibited similar surface roughness parameters, mainly due to the layer stratification and the presence of powder particles partially melted on the surface. The highest surface roughness was observed on the 45+ oriented samples. This was due to the presence of the supports, which are characterized by irregular surfaces and the presence of many imperfections that were measured on the higher roughness of the profile. The results of the roughness measurement are reported in Table 14.

Table 14 - Roughness measurements on differently oriented surfaces and an indication of the direction of measurement(a)

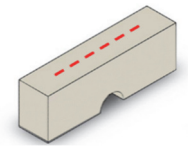

Sample		Ra [mm]	Rz [mm]	Rq [mm]	Rt [mm]
A	Mean	3,22	9,09	1,59	9,01
	Dev std	0,20	0,58	0,22	0,73
B	Mean	5,09	14,38	2,39	14,52
	Dev std	0,48	1,37	0,37	1,38
C	Mean	6,25	17,79	2,69	18,01
	Dev std	0,17	0,64	0,43	0,63
45+	Mean	7,98	22,55	4,03	22,78
	Dev std	1,69	4,78	1,07	4,83

3.3.3.2 Hardness

The orientation of the samples in the build volume can also influence the mechanical characteristics of the part, as the different process history acting on each geometry could lead to different material properties. To assess the anisotropy of the material caused by the process, Rockwell hardness measurements (HRB) were carried out on the flat surface of the miniature samples. The results are presented in Table 15. Four points were measured and averaged to get an average value for each specimen orientation. The difference between the hardness values for

each orientation is relevant with the highest values of hardness exhibited by C and B-oriented samples, which, similarly to what was observed for surface roughness, demonstrate similar properties. The lowest hardness HRB values were found in the A- and 45+ samples due to the specific orientation and the different thermal history during fabrication.

Table 15 – Hardness measurement position and results.

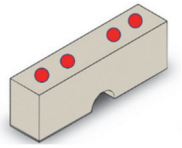

Miniature samples	HRB	Standard Deviation
A-	52.7	1,60
B	56,93	1,63
C	57,65	1,09
45+	53,98	3,00

3.3.3.3 Fatigue results of miniature samples

The fatigue strength of the material and the effect of the investigated properties was then investigated by testing the miniature samples. Evaluating miniature specimens can be extremely beneficial when working with a limited amount of material since it is possible to get multiple specimens from the same amount of material as standard specimens, which can be especially useful for the high-cost process such as L-PBF.

The fatigue results obtained by testing miniature specimens of as-built AlSi10Mg are presented as maximum stress σ_{max} vs. number of cycles to fatigue crack initiation (N) data in the S-N plot reported in Figure 53. The fatigue tests were performed at a stress ratio of R=0 and a test frequency of 25Hz, the run-out, which represents test interruption without failure, was fixed at 2 million cycles and is identified in the plots with arrows.

Fatigue data trends are well distributed in the S-N plots with limited scatter for each specimen orientation; the best performance is exhibited by the A- sample, which demonstrates the highest experimental fatigue strength at 135 MPa. The lowest performance is reached by 45+ samples, which demonstrate a significant reduction compared to A- of about 35% (90 MPa). C and B samples exhibit intermediate and comparable fatigue behavior, revealing a similar trend and experimental fatigue strength (100 MPa). This evidence can be preliminarily related to the measured surface morphology, which is coherent with the results: A- samples are characterized by the lowest roughness and the best performance, while the 45+ samples, described by irregular surface morphology and the highest roughness, exhibited a reduced fatigue behavior.

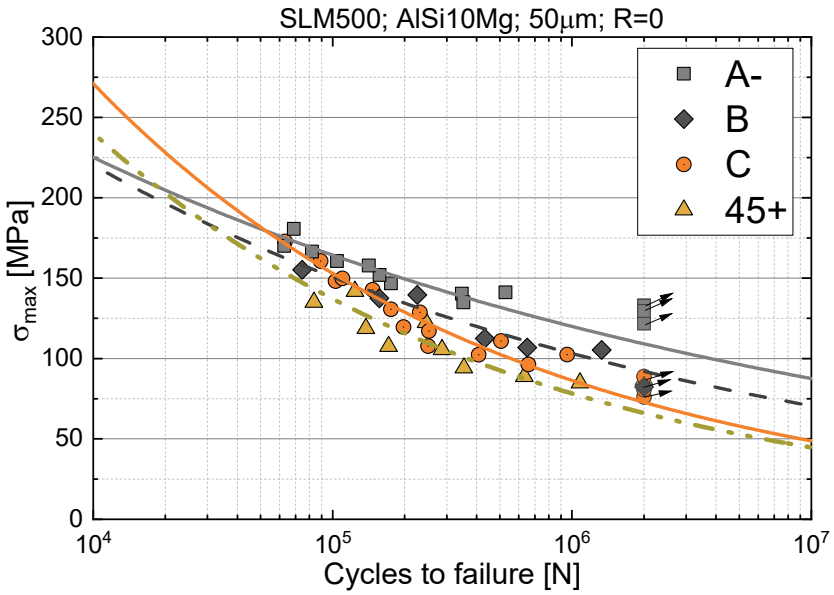

Figure 53 - Fatigue behavior of as-built AlSi10Mg samples produced with SLM500, Nominal layer thickness 50µm.

To generalize the experimental results, the data for each individual set were interpolated using the power law relationship of the type $\sigma^b = N * A$, the statistical estimation of the parameters for the linear model log(N) = log(A) + b log(σ) are summarized in Table 16 in terms of estimated fatigue strength at 2 million cycles and, goodness of fit R^2 and a number of tested specimens.
The estimated fatigue strength was evaluated from the results of the experimental campaign, the estimated fatigue strength was derived from the results obtained on each samples orientation at 2 million cycles.

Table 16 - S-N power law coefficients and exponents. Fatigue strength at 2 10^6 cycles is estimated for different specimen orientations.

Miniature sample	log(A)	b	R2	Number of samples	Estimated fatigue strength at 2 106 cycles s [MPa]
A-	21.21	-7.31	0.87	14	135
B	18.22	-6.09	0.79	7	100
C	13.80	-4.03	0.83	18	90
45+	13.77	-4.10	0.82	13	80

3.3.3.4 Residual stress on miniature samples

Process simulation was performed on the miniature samples to evaluate the stress distribution on samples A, B, and C. The 45+ samples' residual stress values were not evaluated during the simulation procedure because of the difficulties of simulating their distribution being in contact with the support structures.

The process simulation was performed as previously stated, reproducing the process parameter used for the fabrication of the real job.

The stress component that was taken in consideration is the stress direction parallel to the longitudinal dimension of the sample(Figure 54), that is the direction of application of the stress during the fatigue testing. The direction was the same for each sample and the stress distribution was evaluated on the top part of the cross-sectional area at the flat surface opposite to the notch.

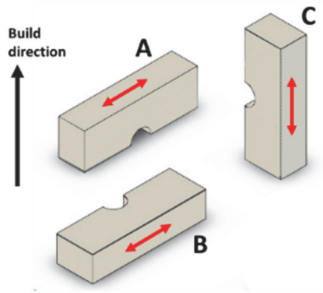

Figure 54 – a) direction of the miniature samples evaluated for residual stress calculation with process simulation and the direction of evaluated stress indicated with red arrow.

The results of the process simulation and the numerical values of the distribution of residual stress observed on the samples is reported in Figure 55 and Figure 56. The first observation that is possible to see is that the difference between each orientation is significant because of the different process histories that each specimen experienced. The trend of the residual stress distribution on the profile is not uniform and changes along the section. Specimen C and A- display a symmetrical distribution of residual stress; instead the specimen B demonstratd an increase; this result is related to the process itself that, for C and A- the linear section that we are observing and analyzing is extrapolated from the same layer and then characterize by the same thermal history and process induced effects; instead the analyzed profile of B sample describe the trend induced by all the layer that contributed in building that sample.

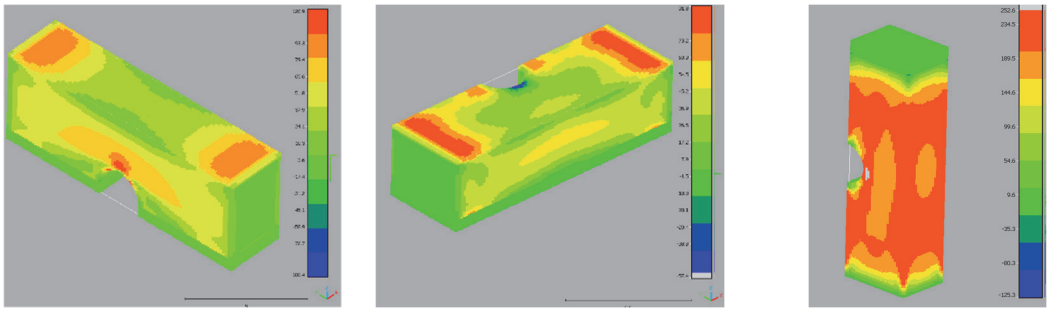

a) b) c)

Figure 55 – Contour plot of the residual stress distribution evaluated using the software simulation software AMPHYON. a) A; b) B, c) C.

It is important to note that the stress values measured in the middle of the cross-section is the one considered for the analysis and for further discussion because it is measured with a more uniform distribution of elements and describe more accurately the stress values, avoiding the stress singularities that have been observed on the edges of the simulated samples.

The vertical miniature sample C demonstrates the highest positive residual stress with the highest values on the edges of the sample and the lowest value of about 185MPa in the middle.

The other two orientations demonstrate a lower residual stress distribution, with positive residual stress of 50MPa for sample B and of 3MPa for orientation A

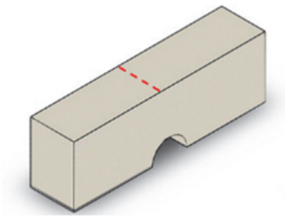

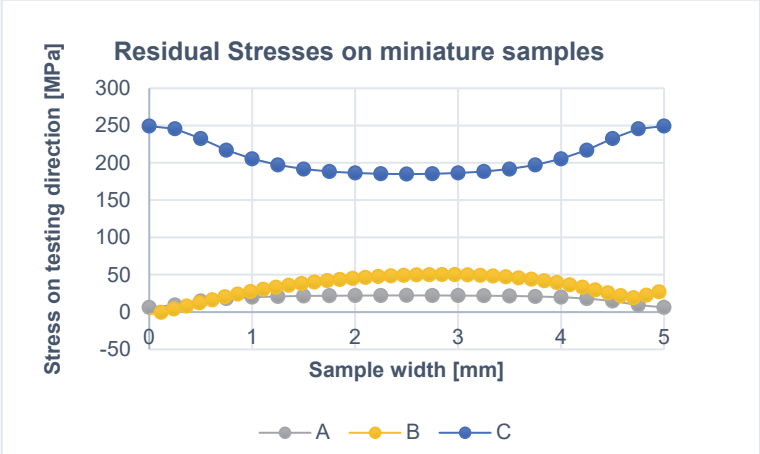

Figure 56 – Residual stress distribution on cross section of the miniature samples, the dashed line indicates the top surface line where the residual stress was evaluated for each orientation.

The value of the residual stress evaluated with process simulation software on A-, B, and C are reported in Table 17.

Table 17 – Reference residual stress values measured on the top profile of the cross-sectional area of the fatigue miniature sample

Sample type - Flat side	Stress [Mpa]
A-	3
B	50
C	185

The resultant residual stress values are compared with results obtained from other studies; Beretta et al. [106] produced a differently oriented sample on the build platform to evaluate the fatigue performance of AlSi10 and investigated the residual stress generated by the manufacturing process by X-ray diffraction. The vertical C sample demonstrated the highest tensile residual stress compared with the other orientation (167,7±20.1 MPa) and considerably lower value of residual stress for A (−6.9 ±10.3 MPa) and B (−14 ±9.4MPa). Samples A and B, which are directly connected to the baseplate, are likely to cool faster and have lower residual stresses, as indicated by the low compressive stresses observed. Meanwhile, sample type C, which does not have any supports in a vertical position, has the highest tensile residual stress. Another evidence of residual stress measurement on AlSI10manufactured by L-PBF is demonstrated by Bagherifard et al [114] that measured the distribution of process-induced residual stress on the vertical as-built sample prior to specific heat treatment finding a consistent distribution of tensile residual stress measuring the highest value of about 100MPa but with an elevated standard deviation of +-40. In addition, Salmi et al[115], focused on the measurement of the residual stress on L-PBF AlSi10Mg using the hole-drilling method (HDM) which is a residual stress measurement technique that is used in industrial practice[116]. The residual stress measured on the vertically fabricated samples reached the highest values reaching the highest value of 100 MPa with limited standard deviation and the horizontal samples are characterized by a residual stress equal to 50mpa.

Because of the many factors that affect the residual stress distribution, it is difficult to give clear-cut answers about how to measure residual stress accurately. Nevertheless, the distribution of residual stress was confirmed to have the maximum value when printed vertically. This result offered important information regarding the accuracy of the data obtained using process simulation software; despite a disparity between the values obtained through numerical simulation and experimental measurement, the three different methods provided coherent results that confirmed the reliability and usefulness of the numerical tool to evaluate the residual stress distribution.

3.3.3.5 Literature comparison

The results obtained from the miniature sample testing allowed to observe that the fatigue behavior of the material is anisotropic and their final different properties are also confirmed by the different properties measured on the samples in terms of surface roughness, hardness, and residual stress.

- Sample A has a roughness of 9.09 μm, a hardness of 51.4 HRB, a residual stress of 3 MPa and an experimental fatigue strength of 135 MPa.
- Sample B has a roughness of 14.38 μm, a hardness of 56.93 HRB, a residual stress of 50 MPa and an experimental fatigue strength of 100 MPa.
- Sample C has a roughness of 17.8 μm, a hardness of 57.65 HRB, a residual stress of 185 MPa and an experimental fatigue strength of 90 MPa.
- Sample 45+ has a roughness of 22.55 μm, a hardness of 53.98 HRB, and experimental fatigue strength of 80 MPa, and residual stress was not calculated.

To ensure consistency, the results of the test conducted on a small sample were compared with those of the fatigue test conducted on as-built samples collected from the literature. The comparison was made using the results of tests conducted under similar conditions from Gerov[117], Beretta[106], Nicoletto[118] and Aboulkhair[119], that tested AlSi10Mg produced by L-PBF at the as-fabricated surface condition and the comparison plot is reported in Figure 57.

Often only vertically built specimens, that is, specimens with their longitudinal axis parallel to the build direction, are often used for the characterization of the L-PBF material performance. This orientation is preferred because testing the layer-wise fabricated material and the peculiar, elongated microstructure produced is expected to provide a conservative performance. Data obtained according to this orientation are then used in comparison with literature and reference data to assess the success of the L-PBF process.

The results of the current work were consistent with the ones obtained previously, indicating that the new testing method was effective and the testing methodology valid. The data obtained from the new methodology was distributed similarly to that reported in the literature, further confirming the accuracy of the results. This suggests that the novel testing method could be a reliable and valuable tool for collecting data and obtaining meaningful results in the future. Moreover, the data obtained was found to be of high quality, providing a strong foundation for further research and development in this area. Furthermore, the testing method was found to be easy to use and versatile, allowing for the collection of data from a variety of sources across a

range of different contexts. This indicates that the method could be an asset for future research, providing an efficient and reliable way of collecting data and obtaining results.

The following chapter presents a comparison of the results from fatigue testing and measurements on miniature samples with those obtained from testing on the actual part. It also describes the methodology used to evaluate the mechanical properties of the part.

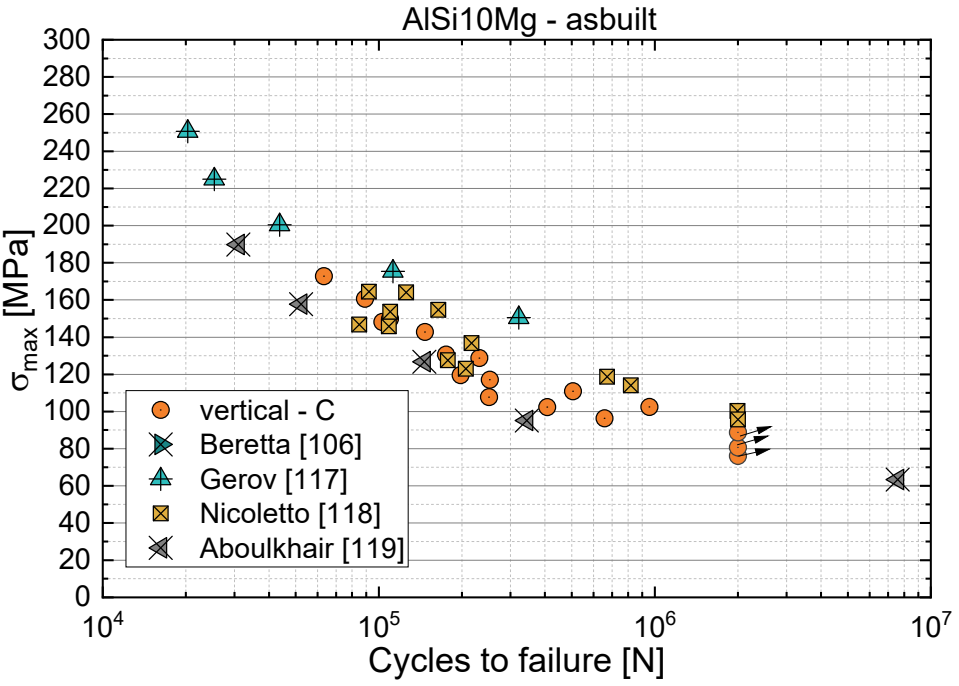

Figure 57 - AlSi10Mg fatigue test comparison performed on as-built samples R=0,1

3.4 Integrated workflow used to develop the fatigue design methodology of an L-PBF AlSi10Mg part

Figure 58 summarizes the sequence of the activities that were developed to design, fabricate, and qualify an L-PBF AlSi10Mg part. While the topological optimization mainly depended on the geometry and loading, the L-PBF fabrication of the part required numerical and experimental activities to arrive at a suitable job definition, defining the qualified process parameters for the equipment and material. Professional software were used to optimize the parts placements, support definition and job finalization. The L-PBF process conditions of AlSi10Mg determined the creation of residual stresses that can affect the structural performance and are frequently neglected. Here L-PBF process simulation software was used to determine residual stress distribution, and to support the part qualification phase, fatigue properties of L-PBF

AlSi10Mg were determined using miniature witness specimens. Experimental qualification in fatigue of the parts was performed on components tested in the laboratory.

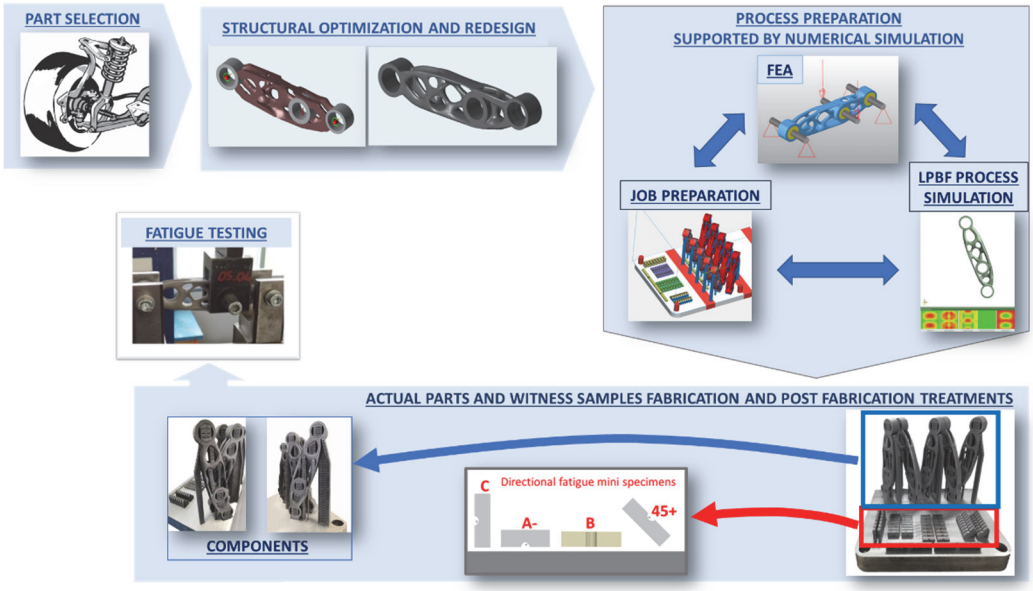

Figure 58 – Integrated design workflow for design, produce, and testing of L-PBF components.

The main objective of this study is to present and discuss an integrated design workflow for a metal additive manufacturing (AM) part, specifically the lower suspension arm of a car. The workflow includes steps such as geometrical topological optimization, AM process simulation, actual part fabrication in an industrial-grade L-PBF system using the AlSi10Mg alloy powder, and structural qualification by fatigue testing of real parts under realistic working conditions. The suspension arm was selected as the component to be optimized as it is subjected to dynamic loading. It, therefore, requires a fatigue integrity assessment at the design stage and subsequent experimental verification. To perform the optimization, the geometry is divided into a "design space", where material can be removed to achieve an optimal geometry and a "non-design space", where material and geometry are fixed to guarantee necessary interfaces. The optimization goal is defined in terms of minimization of mass and global maximization of stiffness while respecting imposed limits and is characterized by the best stiffness-to-weight ratio. The validation of the reconstructed and optimized part geometry requires repeated finite element analyses to identify possible critical points and local model refinement. Numerical process simulation is used to forecast the distribution and magnitude of residual stresses and part deformation upon fabrication and after release from the build plate. The production includes the fabrication of optimized

suspension arms printed according to two different orientations to investigate differences in surface morphology, local hardness, and residual stress distribution, and miniature specimens are also produced to evaluate the effect of build direction on the fatigue performance of the material and to generate fatigue data for part qualification. The fatigue performance is a crucial aspect to be considered for part design and manufacturing process qualification, with laboratory tests used to correlate results from numerical simulation of the model and experimental results on the real part.

4 Fatigue design of L-PBF AlSi10Mg parts

4.1 Fatigue design approach

The final section of the thesis brings together all the numerical and experimental results obtained and uses them within a fatigue design framework. The objective is to demonstrate that once a structural component is identified for redesign and production using L-PBF technology and AlSi10Mg powder, the proposed steps generate all the information needed to predict the fatigue life of the optimized L-PBF ALSi10Mg component.

As in conventional fatigue design, materials allowable are needed to establish an acceptable level of local stresses at critical locations. However, L-PBF technology is still relatively new, AM metals are less known and understood compared to conventionally processed metals and fatigue characterizations are expensive and dependent on AM process parameters. Here we experienced the use of witness specimens that were printed simultaneously with the parts, providing direct information on the combined effect of the fabrication process on fatigue performance. A number of factors, such as surface orientation with respect to building direction, as-built surface roughness, and heat treatment on fatigue of L-PBF AlSi10Mg are thus quantified.

L-PBF fabrication of AlSi10Mg generates residual stresses that the direct aging heat treatment cannot eliminate. Therefore, residual stresses are needed to assess fatigue data of the actual component as well as of the miniature fatigue specimens. This information is obtained by L-PBF process simulation after calibration and is also used in the fatigue assessment.

Finally, the optimized parts typically have a complex geometry that is highly complex with notches and thin sections. The surfaces not used to connect to other parts are typically left in the as-built state for economic and practical reasons. The elastic FE analysis is then needed to link complex geometry and loading patterns to fatigue-critical locations in part. Combining local stress variations and representative fatigue S-N behavior allows the prediction of the component life in fatigue.

So now, the fatigue prediction methodology is proposed with reference to the optimized lower suspension arm component produced in AlSI10Mg by L-PBF. The raw fatigue data obtained by testing miniature specimens and components are recollected and given perspective in the initial subsection. Then both fatigue data sets are upgraded to systematically include several specific factors, such residual stresses, surface roughness, and surface orientation, with respect to building direction in the next two subsections.

In the last subsection, the reviewed fatigue results from the two sources are compared to determine the degree of correlation between the actual fatigue lives of the components and the fatigue lives estimated on the basis of the upgraded miniature specimen data. A good correlation

would support the approach adopted and would demonstrate the usefulness of the miniature witness specimens, whose data could be used for the fatigue design of future L-PBF AlSi10Mg components.

4.2 Integrated workflow for the fatigue design of L-PBF AlSi10Mg parts

All the activities developed in this thesis and described in the previous chapters initially followed a general workflow typical of the development of the L-PBF part shown in Fig. 16. However, the peculiar characteristics of L-PBF AlSi10Mg, which is directly aged only by Beamit before actual use, suggested a significant role played by residual stresses associated to the fabrication process. This motivated the use of the Amphyon software after suitable calibration to determine the distribution and quantify the respective values in the specimens and in the components. This added a demanding simulation phase to the initial workflow, and the results will be exploited in this section.

Further, the fatigue characterization of L-PBF AlSi10Mg was performed originally using directional specimens with as-built surfaces because typically, surfaces of L-PBF parts are left in the as-built condition, and the parts themselves may be printed according to specific directions with the aim of reducing printing time or part distortion or optimal nesting of multiple parts in one build job. The directional fatigue behavior of the miniature specimens provides useful insight into the part response but adds a specific characterization phase to the generic workflow that would typically consider only standard specimens oriented in the vertical direction. The flowchart illustrated in Figure 59 shows the upgraded workflow specifically followed for the design, production, and qualification of the optimized control arm fabricated using L-PBF AlSi10Mg of this thesis that includes the residual stress simulation activity and the specific material characterization in fatigue using directional specimens.

On the other hand, Figure 59 shows the streamlined workflow that could be adopted for the development of a new structural part made of L-PBF AlSi10Mg on the same AM equipment and with the same process parameters. The fatigue characterization at this stage would not be required as now available. The process simulation for residual stress determination would be needed because the different part geometry involves a specific residual stress distribution.

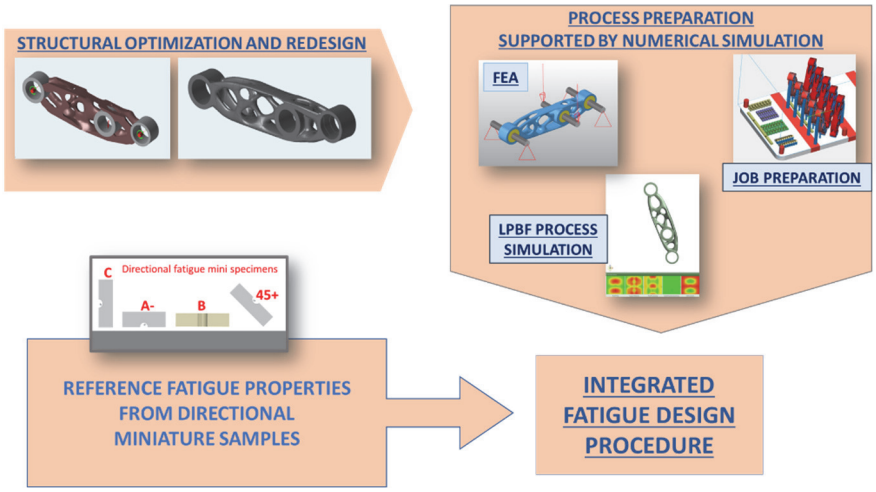

Figure 59 – Integrated procedure for the design of structural L-PBF part from reference fatigue properties

4.3 Fatigue data of L-PBF AlSi10Mg specimens and components

At this point, all data collected from experiments on specimens are reviewed and used to forecast the fatigue of L-PBF-manufactured components. In this section, the raw experimental data in terms of maximum cyclic stress vs number of cycles to failure for the four sets of miniature specimens and for all component tests are collected and plotted in the same diagram of Figure 60.

Inspection of Figure 60 reveals that the directional specimen's behavior, besides being distinct from each other in dependence on factors such as orientation in the build chamber, surface roughness, hardness, and microstructure, is also completely separated from the component S-N trend. Significant longer lives for a given stress level is observed from the control arm data.

So, although the static mechanical properties of the samples and the full-sized component are similar, the results of the fatigue testing reveal important differences in their S-N curves. The conventional approach of estimating the fatigue behavior of a part from the UTS of the constative material is not applicable.

If the part orientation effect is considered in terms of surface roughness, the vertical miniature specimens (denominated C) are expected to be especially relevant for the interpretation of the fatigue behavior of the optimized parts which were printed nearly vertically and whose

locations of fatigue crack initiation where on the lateral vertical surfaces Figure 60 however shows a gap in the S-N trends.

The next section will introduce the role of the residual fabrication stress on the fatigue behavior of the parts and of the witness specimens analytically.

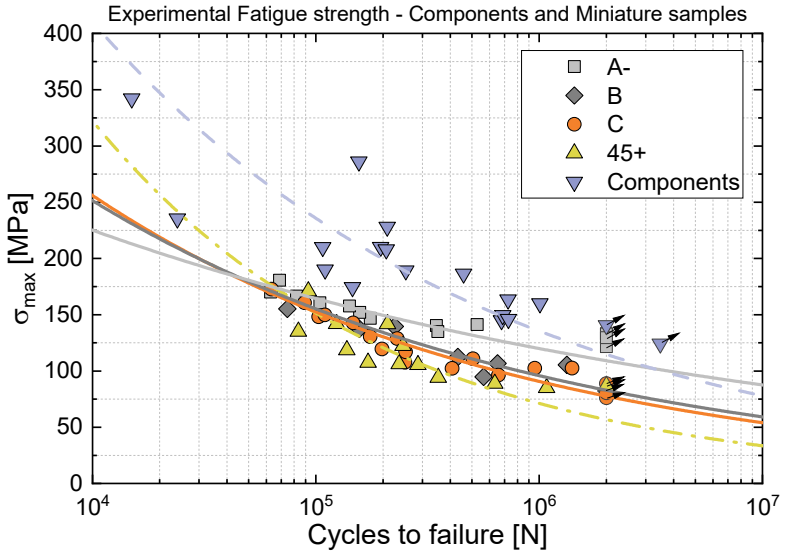

Figure 60 - Experimental fatigue behavior of directional miniatures specimens and optimized parts made of L-PBF AlSi10Mg

4.4 Upgrade of fatigue data from miniature specimen tests

The fatigue data obtained on the miniature specimens and on the lower control arms are reexamined in this section to account for the role of the residual stresses.

Table 18 summarizes the characterizing data of the directional miniature specimens of L-PBF AlSi10Mg obtained previously as surface roughness in terms of Rz value and hardness for each sample.

Table 18 – Representative properties of AlSi10Mg miniature samples

	Rz [µm]	HRB	Residual stress [Mpa]
A	9,01	51,4	3
B	14,38	56,9	50
C	19,78	57,7	185

In addition, the last column lists the relevant residual stress values obtained from the L-PBF process simulation described in the previous section and determined at the center of the flat specimen surface opposite to the round notch; that is where fatigue crack initiation occurs. It is noted that the vertical miniature specimens are characterized by a very high tensile residual stress compared to the other directions.

On the other hand, all the fatigue tests on the miniature samples were conducted with a load ratio of R=0 as prescribed by the approach introduced in work.

A factor to be considered to explain the fatigue strength differences among miniature specimens is the distribution of residual stress in different orientations of the samples, as residual stress can affect the fatigue performance by altering the intended load stress ratio R to an effective stress ratio R_{eff} as mean stress in the load cycle would.

Since the effective stress ratio is different for each sample depending on the actual testing load and residual stress of the specific configuration, it is necessary to correct the mean stress condition for each curve at a full reverse fatigue strength. The maximum and minimum stress values considering the influence of the residual stress are identified as effective stress values (σ_{eff}) and are equal to the nominal values considered in the experiment (σ_{nom}) plus the residual stress (σ_{res}) evaluated with the process simulation on the specific orientation.

$$\boldsymbol{\sigma_{max,eff} = \sigma_{max,nom} + \sigma_{res}} \tag{1}$$

$$\boldsymbol{\sigma_{max,eff} = \sigma_{max,nom} + \sigma_{res}} \tag{2}$$

$$\boldsymbol{\sigma_{max,eff} = \sigma_{max,nom} + \sigma_{res}} \tag{3}$$

$$\boldsymbol{\sigma_{min,eff} = \sigma_{min,nom} + \sigma_{res}} \tag{4}$$

The effective load stress ratio R_{eff}, describe the effective load ration of each sample depending from the experimental stress applied and the residual stress recognized for the single orientation.

$$\boldsymbol{R_{eff} = \frac{\sigma_{min,eff}}{\sigma_{max,eff}}} \tag{5}$$

As a result, the residual stresses acting on the sample lead to a change in the definition of the mean stress and stress amplitude.

$$\sigma_{m,eff} = \frac{\sigma_{max,eff} + \sigma_{min,eff}}{2} \quad (6)$$

$$\sigma_{amp,eff} = \frac{\sigma_{max,eff} - \sigma_{min,eff}}{2} \quad (7)$$

The results of the fatigue tests performed on the three different orientations of miniature samples, with the indication of the nominal stress applied during the experimental campaign under a nominal load stress ratio R=0 and the effective values, including the effect of the residual stress which generates a different load stress ratio R_{eff} for each test, conditions are reported in Table 20.

Since these fatigue data are effectively characterized by given constant amplitude values but different R ratios, to be compared they must be converted to the same stress ratio. Therefore, the following Goodman-Haigh relation[120], is used to convert the effective experimental values to an equivalent fully reversed loading condition, R=-1,

$$\sigma_{-1,eff} = \frac{\sigma_{amp,eff}}{1 - \frac{\sigma_{m,eff}}{UTS}} \quad (8)$$

The effective R-ratio correction was applied to all specimen groups except the 45+ set because their residual stress value was not evaluated during the simulation procedure, as previously explained. The UTS value used in the calculation is obtained from the reference UTS value declared by the company's data sheet and is equal to 414 [MPa] as reported in Table 8.

Figure 61 shows the converted stress amplitudes vs. cycles to failure. The vertical specimens show a completely different trend compared to the other two directions.

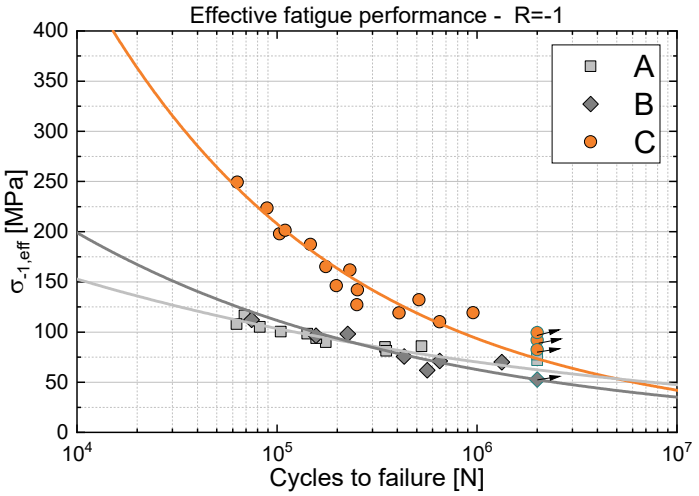

Figure 61- Fatigue strength of miniature samples in converted fully reverse loading condition considering the effect of residual stress.

The conversion shows an improved performance of the vertical samples that shift upward in comparison with the other orientation because they were affected by a severe tensile mean stress. The estimated strength after correction is 105 MPa. Orientation A and B exhibit a similar material response with fatigue strength, respectively, of 85 MPa and 60 MPa. Exponents and coefficients of the respective power law representations are given in Table 19.

Table 19 - S-N power law coefficients and exponents and fatigue strength at 2 10^6 cycles is estimated for different specimen orientations in the condition of fully reverse loading.

Miniature sample R=-1	log(A)	b	R^2	Fatigue strength at 2 10^6 cycles $\sigma_{-1,eff}$ [MPa]
A-	16.42	-5.91	0.87	85
B	13.15	-3.98	0.8	60
C	11.68	-2.88	0.87	105

The impact of residual stress on the mechanical response of L-PBF-produced parts has been revealed through the observation of directional behavior of miniature specimen performance. The convertion of the nominal applied stress at an effective R ratio influenced by the residual stress to a residual stress-free stress modified significantly the fatigue performance.

A similar approach is used now to convert the fatigue response of the components experimentally tested at nominal load ratio R = 0,1 to an effective fatigue stress at the each critical location in the part at an equivalent R=-1 ratio. The residual stress at the critical location defines an effective load ratio R_{eff} and Goodman-Haigh relation provides $\sigma_{-1,eff}$.

The experimental nominal fatigue stress at the critical location, the residual stress at the same location as determined by process simulation and the effective stress $\sigma_{-1,eff}$ are listed in Table 21.

Table 20 – Fatigue test results of the directional miniature specimens corrected for the presence of residual stresses.

Sample	Cycles to failure	$\sigma_{max,nom}\ [MPa]$	$\sigma_{min,eff}\ [MPa]$	$\sigma_{max,eff}\ [MPa]$	R_{eff}
C	147000	142,7	185	327,7	0,56
C	407800	102,4	185	287,4	0,64
C	649600	96,3	185	281,3	0,66
C	252600	117,0	185	302,0	0,61
C	2000500	83,2	185	268,2	0,69
C	175200	130,6	185	315,6	0,59
C	2000700	88,8	185	273,8	0,68
C	231500	128,8	185	313,8	0,59
C	955800	102,4	185	287,4	0,64
C	103000	148,1	185	333,1	0,56
C	109800	149,9	185	334,9	0,55
C	250700	107,7	185	292,7	0,63
C	89100	160,6	185	345,6	0,54
C	197900	119,6	185	304,6	0,61
C	2000000	76,1	185	261,1	0,71
C	63300	172,2	185	357,2	0,52
C	512800	110,8	185	295,8	0,63
B	156800	137,5	50	187,5	0,27
B	225600	139,5	50	189,5	0,26
B	74600	155,2	50	205,2	0,24
B	650600	106,8	50	156,8	0,32
B	1330400	105,3	50	155,3	0,32
B	432200	112,4	50	162,4	0,31
B	564000	94,7	50	144,7	0,35
B	2000300	82,2	50	132,2	0,38
A	2000600	121,6	3	124,6	0,024
A	68800	180,6	3	183,6	0,016
A	82000	166,5	3	169,5	0,018
A	2000700	133,0	3	136,0	0,022
A	175400	146,8	3	149,8	0,020
A	157100	152,0	3	155,0	0,019
A	346900	140,3	3	143,3	0,021
A	2000800	132,9	3	135,9	0,022
A	141600	157,8	3	160,8	0,019
A	62800	170,1	3	173,1	0,017
A	528100	141,2	3	144,2	0,021
A	351800	135,0	3	138,0	0,022
A	2000200	129,5	3	132,5	0,023
A	104400	160,6	3	163,6	0,018

Table 21 – Nominal and effective experimental results of fatigue test on L-PBF components and local residual stresses

Specimen ID	Test configuration	Crack position	σ_{res} $[MPa]$	σ_{nom} $[MPa]$	Cycles to failure	$\sigma_{-1,eff}$ $[MPa]$
A1	TC1	M	24,5	285,99	156000	229,5
	TC2	S1	36	189,27	252900	128,7
	TC3	U	46,5	179,89	146000	124,8
B1	TC1	M	31,5	228	209000	165,2
	TC2	S2	40	145	678730	91,8
	TC3	U	47,5	154,27	686916	102,0
A2	TC1	M	24,5	342	15000	316,4
	TC2	S1	36	210,1	195000	149,1
B2	TC1	M	31,5	163,4	725777	104,0
	TC2	S2	40	160	1008000	104,2
	TC3	U	47,5	242,87	24000	194,3
A3	TC1_step1		24.5	124,184	3488500 àrunout	72,0
	TC1_step2	M	24,5	186,352	459000	121,0
	TC2	S1	36	145,958	728782	91,3
	TC3	U	46,5	214,49	206796	160,1
B3	TC1		31,5	140,6	2000000 à runout	85,8
	TC2	S2	40	210	107400	151,3
	TC3	U	47.5	196	11000	141,1

Figure 62shows the converted stress amplitudes vs cycles to failure for the components when residual stress effect is compensated. The correlation factor $R^{2,}$ equivalent to 0.77, reported in Table 22, shows a good correlation of the results.

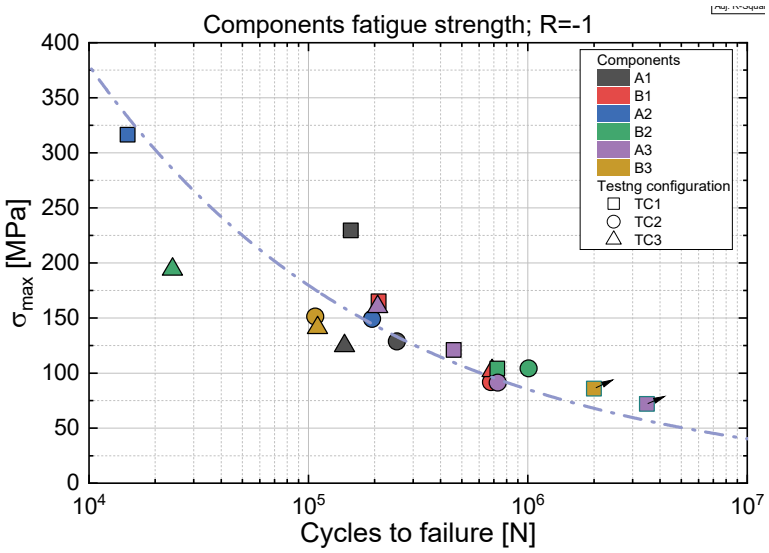

Figure 62 - Fatigue strength of A and B components after considering the effect of residual stress.

Table 22 - S-N power law coefficients and exponents for components fatigue behavior at full reverse loading

Component fully reverse fatigue strength R=-1	log(A)	b	R2	Fatigue strength at 2 106 cycles $\sigma_{-1,eff}$ [MPa]
	11.95	--3.08	0.77	90

4.5 Assessment of the fatigue design methodology

Initially the direct comparison of experimental data from specimens and from parts after the residual stress correction described in the previous section is shown in Figure 63.

The comparison considered only the vertical C specimens. This choice lies in the fact that first this direction is usually the most widely used for the characterization of the basic properties, and secondly, the vertical orientation of the mini-samples is similar to that of the components, and therefore the surface roughness, the layer orientation wit respect to the applied stress and the microstructure are expected to be similar. The two experimental fatigue curves are close one another and thus highlight a strong similitude in the fatigue performance of these two configurations although they are geometrically different and with specific influencing factors.

The previous diagram compared experimental data from specimens and from parts because the aim of the research was to have significant information on the fatigue behavior of the components.

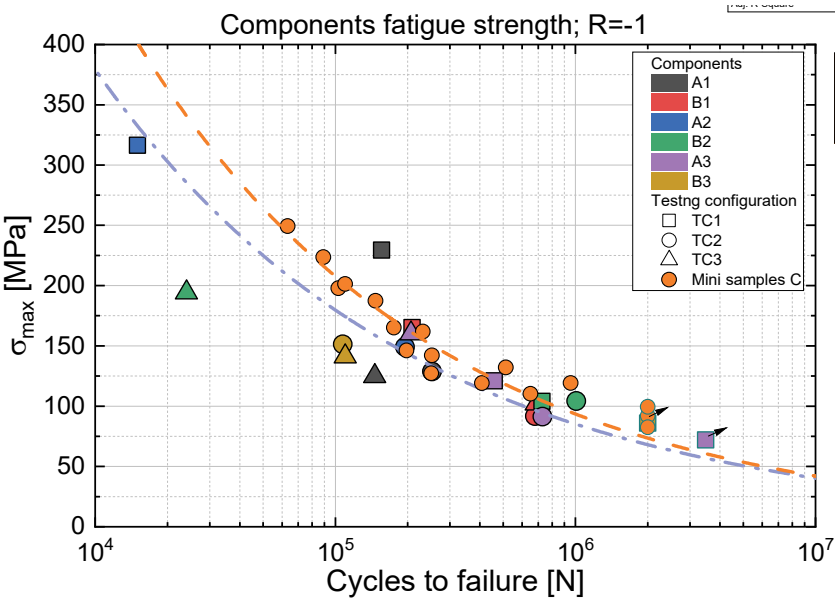

Figure 63 – S-N plot comparing the fatigue strength of components and vertical miniature sample at full reverse loading condition.

Now an alternative situation could be investigated. Given the reference fatigue S-N curve of the miniature C specimens, the live stress from FEA and residual stress from process simulation at a critical location of the L-PBF part are used to predict the fatigue life of the part. This would hold for othe part geometries provided that they are produced by L-PBF processing of AlSi10Mg powder.

Figure 64 show the comparison between predicted and experimental lives for the different L-PBF parts and their different testing configurations. The approach slightly over estimate the component lives, that is longer lives of the component than its actual lives.

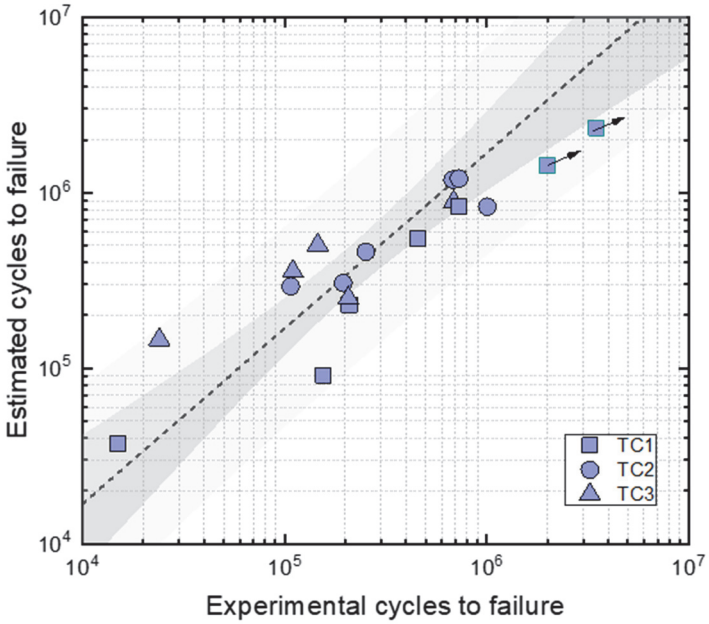

Figure 64 – Components comparison between experimental values and estimated values forecasted from fatigue vertical miniature samples.

A possible contribution in that direction could be the stress gradient effect. Failures in the parts were at rounded notches, hence in presence of a stress gradient, while failure of the miniature specimens occurred on flat surfaces under the weak gradient due to bending.

Nonetheless this first comparison suggests that the miniature sample method can be used to assess and predict the fatigue behavior of parts produced using L-PBF without having to conduct tests on actual parts.

5 Conclusions and outlook

This thesis discussed the use of Laser Powder Bed Fusion (L-PBF) to produce structural parts made of AlSi10Mg, highlighting the advantages and limitations of the technology and the challenges that need to be addressed in terms of material characterization, qualification, and applications.

The main conclusions drawn from this thesis are:

- The overall mechanical properties of materials produced by L-PBF are described by the combined effect of multiple factors identified in material microstructure, surface roughness, defects distribution, and residual stress.
- The research gained insights into the design, development, and testing phases for a structural component made of L-PBF AlSi10Mg for its potential use in the automotive industry. A lower suspension arm of a car was used here as a case study.
- Topology optimization and redesign tools allowed to obtain a 55% mass reduction and an improved stiffness-to-weight ratio with respect to the reference geometry.
- Process simulation software was used for the optimization of the production process and was found valuable for the evaluation of the residual stress distribution within the parts.
- The part has been analyzed using finite element analysis to assess its structural response under different testing conditions. Among the valuable data, the failure positions were found to be consistent with what was expected from FEA.
- The optimized parts fabricated by L-PBF in two different orientations with respect to build direction showed a limited influence of the fatigue response on part orientation.
- Directional miniature fatigue samples were produced alongside the optimized part; the experimental results of the miniature samples revealed a significant variation in fatigue strength depending on the orientation of the specimen. These variations were attributed to the different factors observed for each specific orientation, such as surface roughness and residual stress.
- The effect of residual stress on loading conditions and their impact on the results has been studied, converting the miniature samples and components' fatigue

strength to a residual stress-free condition, and their impact was observed as remarkable.

- A correlation model has been established to compare the fatigue behavior of the parts and of the samples, considering the impact of residual stress on the loading conditions. This provided valuable data that can be used to understand the effect of the production process and predict the fatigue performance of actual parts.
- A preliminary approach for designing fatigue-critical components without the need for full-scale testing was identified but required further investigation and improvement.

Unfortunately, this work was limited in time, but further studies are planned to be continued in the future

- There is still a need for more fatigue data to be gathered to understand further the impact of various technological factors on the fatigue performance of these parts and be able to fully comprehend the causes of the directional fatigue behavior.
- Additional consideration on defects distribution and material microstructure should be studied in future research to understand their impact on fatigue performance.
- Assessing the applicability of the findings to several types of materials is important to support the design and development of fatigue-critical components and improve the production process.

References

[1] T. J. Horn and O. L. A. Harrysson, 'Overview of Current Additive Manufacturing Technologies and Selected Applications', *Sci. Prog.*, vol. 95, no. 3, pp. 255–282, Sep. 2012, doi: 10.3184/003685012X13420984463047.

[2] J. J. Beaman, D. L. Bourell, C. C. Seepersad, and D. Kovar, 'Additive Manufacturing Review: Early Past to Current Practice', *J. Manuf. Sci. Eng.*, vol. 142, no. 11, p. 110812, Nov. 2020, doi: 10.1115/1.4048193.

[3] T. D. Ngo, A. Kashani, G. Imbalzano, K. T. Q. Nguyen, and D. Hui, 'Additive manufacturing (3D printing): A review of materials, methods, applications and challenges', *Compos. Part B Eng.*, vol. 143, pp. 172–196, Jun. 2018, doi: 10.1016/j.compositesb.2018.02.012.

[4] I. Gibson, D. W. Rosen, and B. Stucker, *Additive manufacturing technologies: 3D printing, rapid prototyping and direct digital manufacturing*, 2nd edition. New York London: Springer, 2015.

[5] Hull, Charles, 'Method for production of three-dimensional objects by stereolithography', U.S. Patent No. 4,929,402.

[6] W. E. Frazier, 'Metal Additive Manufacturing: A Review', *J. Mater. Eng. Perform.*, vol. 23, no. 6, pp. 1917–1928, Jun. 2014, doi: 10.1007/s11665-014-0958-z.

[7] European Patent Office, 'Patents and additive manufacturing - Trends in 3D printing technologies', 2019.

[8] M. K. Thompson *et al.*, 'Design for Additive Manufacturing: Trends, opportunities, considerations, and constraints', *CIRP Ann.*, vol. 65, no. 2, pp. 737–760, 2016, doi: 10.1016/j.cirp.2016.05.004.

[9] R. Huang *et al.*, 'Energy and emissions saving potential of additive manufacturing: the case of lightweight aircraft components', *J. Clean. Prod.*, vol. 135, pp. 1559–1570, Nov. 2016, doi: 10.1016/j.jclepro.2015.04.109.

[10] M. Bhuvanesh Kumar and P. Sathiya, 'Methods and materials for additive manufacturing: A critical review on advancements and challenges', *Thin-Walled Struct.*, vol. 159, p. 107228, Feb. 2021, doi: 10.1016/j.tws.2020.107228.

[11] F42 Committee, 'Terminology for Additive Manufacturing Technologies', ASTM International. doi: 10.1520/F2792-12.

[12] ISO/ASTM, 'Additive manufacturing — General principles — Fundamentals and vocabulary', *ISO*. https://www.iso.org/standard/74514.html (accessed Dec. 01, 2022).

[13] ISO/ASTM, 'Additive manufacturing — Design — Part 1: Laser-based powder bed fusion of metals', *ISO*. https://www.iso.org/standard/72951.html (accessed Dec. 01, 2022).

[14] C. Y. Yap *et al.*, 'Review of selective laser melting: Materials and applications', *Appl. Phys. Rev.*, vol. 2, no. 4, p. 041101, Dec. 2015, doi: 10.1063/1.4935926.

[15] B. Mueller, 'Additive Manufacturing Technologies – Rapid Prototyping to Direct Digital Manufacturing', *Assem. Autom.*, vol. 32, no. 2, Apr. 2012, doi: 10.1108/aa.2012.03332baa.010.

[16] Allied Market Research, 'Metal Additive Manufacturing Market. Global Opportunity Analysis and Industry Forecast, 2021-2031', Aug. 2022.

[17] AMPOWER, 'Metal Additive Manufacturing Market Report', 2022. [Online]. Available: https://additive-manufacturing-report.com/

[18] M. Gorelik, 'Additive manufacturing in the context of structural integrity', *Int. J. Fatigue*, vol. 94, pp. 168–177, Jan. 2017, doi: 10.1016/j.ijfatigue.2016.07.005.

[19] Wohler Associates, 'Wohlers Report 2020 - 3D Printing and Additive Manufacturing - Globale State of the Industry', ISBN 978-0-9913332-6-4, 2020.

[20] ‘Boeing Creates the First 3D Printed Metal Satellite Antenna, Saves on Mass, Time, and Costs - 3DPrint.com | The Voice of 3D Printing / Additive Manufacturing’. https://3dprint.com/239651/boeing-creates-the-first-3d-printed-metal-satellite-antenna-saves-on-mass-time-and-costs/ (accessed Jan. 05, 2023).
[21] M. Orme, ‘How AM is Disrupting the Aerospace Industry’. https://www.sme.org/technologies/articles/2022/may/how-am-is-disrupting-the-aerospace-industry/ (accessed Jan. 03, 2023).
[22] ‘Transformation In 3D: How A Walnut-Sized Part Changed The Way GE Aviation Builds Jet Engines | GE News’. https://www.ge.com/news/reports/transformation-3d-walnut-sized-part-changed-way-ge-aviation-builds-jet-engines (accessed Jan. 03, 2023).
[23] ‘Bugatti - World premiere: brake caliper from 3-D printer’. https://www.bugatti.com/media/news/2018/world-premiere-brake-caliper-from-3-d-printer/ (accessed Jan. 03, 2023).
[24] M. Molitch-Hou, ‘A Man, a Plan, a 3D Printed Hypercar: A Talk with Divergent 3D’s Kevin Czinger’, *3DPrint.com | The Voice of 3D Printing / Additive Manufacturing*, Mar. 14, 2022. https://3dprint.com/289601/a-man-a-plan-a-3d-printed-hypercar-a-talk-with-divergent-3ds-kevin-czinger/ (accessed Jan. 03, 2023).
[25] F. Voulpiotis, ‘Why is Formula 1 turning to 3D printing?’, *3Dnatives*, Mar. 27, 2022. https://www.3dnatives.com/en/formula-1-turning-to-3d-printing-281020194/ (accessed Jan. 03, 2023).
[26] T. T. Oliveira and A. C. Reis, ‘Fabrication of dental implants by the additive manufacturing method: A systematic review’, *J. Prosthet. Dent.*, vol. 122, no. 3, pp. 270–274, Sep. 2019, doi: 10.1016/j.prosdent.2019.01.018.
[27] A. Sarker, M. Leary, and K. Fox, ‘Metallic additive manufacturing for bone-interfacing implants’, *Biointerphases*, vol. 15, no. 5, p. 050801, Sep. 2020, doi: 10.1116/6.0000414.
[28] K. Schmidtke, F. Palm, A. Hawkins, and C. Emmelmann, ‘Process and Mechanical Properties: Applicability of a Scandium modified Al-alloy for Laser Additive Manufacturing’, *Phys. Procedia*, vol. 12, pp. 369–374, Jan. 2011, doi: 10.1016/j.phpro.2011.03.047.
[29] M. Raab and M. Bambach, ‘Fatigue properties of Scalmalloy® processed by laser powder bed fusion in as-built, chemically and conventionally machined surface condition’, *J. Mater. Process. Technol.*, vol. 311, p. 117811, Jan. 2023, doi: 10.1016/j.jmatprotec.2022.117811.
[30] ‘Filippo Ganna breaks record on Pinarello 3D printed bike’, *Metal Additive Manufacturing*, Oct. 07, 2022. https://www.metal-am.com/filippo-ganna-breaks-record-on-pinarello-3d-printed-bike/ (accessed Jan. 03, 2023).
[31] J. Baker, ‘An Investigation into the Handlebar Failure that Occurred in the Australian Men’s Team Pursuit race at the Tokyo 2020 Olympics’.
[32] O. Rehme, C. Emmelmann, and E. Beyer, ‘Reproducibility for properties of selective laser melting products, INTERNATIONAL CONFERENCE; 3rd, Lasers in manufacturing; LIM 2005’, in *Lasers in manufacturing; LIM 2005, LASERS IN MANUFACTURING -WLT CONFERENCE- CD-ROM EDITION-, INTERNATIONAL CONFERENCE; 3rd, Lasers in manufacturing; LIM 2005*, Stuttgart, 2005, pp. 227–232. [Online]. Available: https://www.tib.eu/de/suchen/id/BLCP%3ACN068599180
[33] J. P. Oliveira, A. D. LaLonde, and J. Ma, ‘Processing parameters in laser powder bed fusion metal additive manufacturing’, *Mater. Des.*, vol. 193, p. 108762, Aug. 2020, doi: 10.1016/j.matdes.2020.108762.
[34] D. Thomas and S. Gilbert, ‘Costs and Cost Effectiveness of Additive Manufacturing’. Special Publication (NIST SP), National Institute of Standards and Technology, Gaithersburg, MD, Dec. 04, 2014. doi: https://doi.org/10.6028/NIST.SP.1176.

[35] E. Maleki *et al.*, 'Fatigue behaviour of notched laser powder bed fusion AlSi10Mg after thermal and mechanical surface post-processing', *Mater. Sci. Eng. A*, vol. 829, p. 142145, Jan. 2022, doi: 10.1016/j.msea.2021.142145.
[36] A. Yadollahi and N. Shamsaei, 'Additive manufacturing of fatigue resistant materials: Challenges and opportunities', *Int. J. Fatigue*, vol. 98, pp. 14–31, May 2017, doi: 10.1016/j.ijfatigue.2017.01.001.
[37] H. A. Stoffregen, K. Butterweck, and E. Abele, 'FATIGUE ANALYSIS IN SELECTIVE LASER MELTING: REVIEW AND INVESTIGATION OF THIN-WALLED ACTUATOR HOUSINGS'.
[38] H. Irrinki *et al.*, 'Effects of particle characteristics on the microstructure and mechanical properties of 17-4 PH stainless steel fabricated by laser-powder bed fusion', *Powder Technol.*, vol. 331, pp. 192–203, May 2018, doi: 10.1016/j.powtec.2018.03.025.
[39] S. E. Brika, M. Letenneur, C. A. Dion, and V. Brailovski, 'Influence of particle morphology and size distribution on the powder flowability and laser powder bed fusion manufacturability of Ti-6Al-4V alloy', *Addit. Manuf.*, vol. 31, p. 100929, Jan. 2020, doi: 10.1016/j.addma.2019.100929.
[40] S. Vock, B. Klöden, A. Kirchner, T. Weißgärber, and B. Kieback, 'Powders for powder bed fusion: a review', *Prog. Addit. Manuf.*, vol. 4, no. 4, pp. 383–397, Dec. 2019, doi: 10.1007/s40964-019-00078-6.
[41] B. Poorganji, E. Ott, R. Kelkar, A. Wessman, and M. Jamshidinia, 'Review: Materials Ecosystem for Additive Manufacturing Powder Bed Fusion Processes', *JOM*, vol. 72, no. 1, pp. 561–576, Jan. 2020, doi: 10.1007/s11837-019-03892-z.
[42] N. T. Aboulkhair, M. Simonelli, L. Parry, I. Ashcroft, C. Tuck, and R. Hague, '3D printing of Aluminium alloys: Additive Manufacturing of Aluminium alloys using selective laser melting', *Prog. Mater. Sci.*, vol. 106, p. 100578, Dec. 2019, doi: 10.1016/j.pmatsci.2019.100578.
[43] N. Haghdadi, M. Laleh, M. Moyle, and S. Primig, 'Additive manufacturing of steels: a review of achievements and challenges', *J. Mater. Sci.*, vol. 56, no. 1, pp. 64–107, Jan. 2021, doi: 10.1007/s10853-020-05109-0.
[44] M. Revilla-León and M. Özcan, 'Additive Manufacturing Technologies Used for 3D Metal Printing in Dentistry', *Curr. Oral Health Rep.*, vol. 4, no. 3, pp. 201–208, Sep. 2017, doi: 10.1007/s40496-017-0152-0.
[45] R. R. Boyer, 'An overview on the use of titanium in the aerospace industry', *Mater. Sci. Eng. A*, vol. 213, no. 1–2, pp. 103–114, Aug. 1996, doi: 10.1016/0921-5093(96)10233-1.
[46] E. Yasa and O. Poyraz, 'Powder Bed Fusion Additive Manufacturing of Ni-Based Superalloys: Applications, Characteristics, and Limitations', in *Advances in Civil and Industrial Engineering*, K. R. Balasubramanian and V. Senthilkumar, Eds. IGI Global, 2020, pp. 249–270. doi: 10.4018/978-1-7998-4054-1.ch013.
[47] F. Uriati, G. Nicoletto, and A. H. A. Lutey, 'As-built surface quality and fatigue resistance of Inconel 718 obtained by additive manufacturing', *Mater. Des. Process. Commun.*, vol. 3, no. 4, Aug. 2021, doi: 10.1002/mdp2.228.
[48] F. Uriati, G. Nicoletto, E. Riva, T. Varmus, and R. Konečná, 'Influence of surface orientation on fatigue performance of as-built additively manufactured Inconel 718', *Eng. Manuf. Lett.*, vol. 1, no. 1, pp. 34–39, Apr. 2022, doi: 10.24840/2795-5168_001-001_0007.
[49] F. Uriati and G. Nicoletto, 'A comparison of Inconel 718 obtained with three L-PBF production systems in terms of process parameters, as-built surface quality, and fatigue performance', *Int. J. Fatigue*, vol. 162, p. 107004, Sep. 2022, doi: 10.1016/j.ijfatigue.2022.107004.

[50] T. Varmus, R. Konecna, G. Nicoletto, and F. Uriati, 'Microstructure and Fatigue Properties of Al2024-RAM2 Aluminum Alloy Obtained by Laser Powder Bed Fusion', *Procedia Struct. Integr.*, vol. 43, pp. 184–189, 2023, doi: 10.1016/j.prostr.2022.12.256.
[51] D. Alberts, D. Schwarze, and G. Witt, 'IN SITU MELT POOL MONITORING AND THE CORRELATION TO PART DENSITY OF INCONEL® 718 FOR QUALITY ASSURANCE IN SELECTIVE LASER MELTING', p. 14.
[52] D. Greitemeier, C. Dalle Donne, F. Syassen, J. Eufinger, and T. Melz, 'Effect of surface roughness on fatigue performance of additive manufactured Ti–6Al–4V', *Mater. Sci. Technol.*, vol. 32, no. 7, pp. 629–634, May 2016, doi: 10.1179/1743284715Y.0000000053.
[53] D. Obilanade, C. Dordlofva, and P. Törlind, 'SURFACE ROUGHNESS CONSIDERATIONS IN DESIGN FOR ADDITIVE MANUFACTURING - A LITERATURE REVIEW', *Proc. Des. Soc.*, vol. 1, pp. 2841–2850, Aug. 2021, doi: 10.1017/pds.2021.545.
[54] R. K. Leach, D. Bourell, S. Carmignato, A. Donmez, N. Senin, and W. Dewulf, 'Geometrical metrology for metal additive manufacturing', *CIRP Ann.*, vol. 68, no. 2, pp. 677–700, Jan. 2019, doi: 10.1016/j.cirp.2019.05.004.
[55] G. Nicoletto and F. Uriati, 'Fatigue Behavior of As-Built L-PBF Inconel 718 and Surface Roughness-Based Modeling', in *Fatigue and Fracture of Materials and Structures*, vol. 24, G. Lesiuk, S. Duda, J. A. F. O. Correia, and A. M. P. De Jesus, Eds. Cham: Springer International Publishing, 2022, pp. 333–339. doi: 10.1007/978-3-030-97822-8_39.
[56] F. Uriati, G. Nicoletto, and R. Konečná, 'FE Modelling of the Fatigue Behaviour of L-PBF Inconel 718 with As-Built Surfaces', in *Structural Integrity and Fatigue Failure Analysis*, vol. 25, G. Lesiuk, M. Szata, W. Blazejewski, A. M. P. de Jesus, and J. A. F. O. Correia, Eds. Cham: Springer International Publishing, 2022, pp. 117–125. doi: 10.1007/978-3-030-91847-7_12.
[57] T. Varmus, R. Konecna, and G. Nicoletto, 'Microstructure and fatigue performace of additively manufactured AlSi10Mg.', *Transp. Res. Procedia*, vol. 55, pp. 518–525, Jan. 2021, doi: 10.1016/j.trpro.2021.07.016.
[58] Y. Kok *et al.*, 'Anisotropy and heterogeneity of microstructure and mechanical properties in metal additive manufacturing: A critical review', *Mater. Des.*, vol. 139, pp. 565–586, Feb. 2018, doi: 10.1016/j.matdes.2017.11.021.
[59] L. Thijs, F. Verhaeghe, T. Craeghs, J. V. Humbeeck, and J.-P. Kruth, 'A study of the microstructural evolution during selective laser melting of Ti–6Al–4V', *Acta Mater.*, vol. 58, no. 9, pp. 3303–3312, May 2010, doi: 10.1016/j.actamat.2010.02.004.
[60] M. Frkan, R. Konecna, G. Nicoletto, and L. Kunz, 'Microstructure and fatigue performance of SLM-fabricated Ti6Al4V alloy after different stress-relief heat treatments', *Transp. Res. Procedia*, vol. 40, pp. 24–29, 2019, doi: 10.1016/j.trpro.2019.07.005.
[61] R. Konecna, F. Uriati, G. Nicoletto, and V. Tibor, 'Surface quality and fatigue behavior of L-PBF AlSi10Mg in as-built condition', *Procedia Struct. Integr.*, vol. 34, pp. 135–140, 2021, doi: 10.1016/j.prostr.2021.12.020.
[62] S. Romano, A. Abel, J. Gumpinger, A. D. Brandão, and S. Beretta, 'Quality control of AlSi10Mg produced by SLM: Metallography versus CT scans for critical defect size assessment', *Addit. Manuf.*, vol. 28, pp. 394–405, Aug. 2019, doi: 10.1016/j.addma.2019.05.017.
[63] A. Jones, M. Leary, S. Bateman, and M. Easton, 'Effect of surface geometry on laser powder bed fusion defects', *J. Mater. Process. Technol.*, vol. 296, p. 117179, Oct. 2021, doi: 10.1016/j.jmatprotec.2021.117179.
[64] M. R. G. Prasad *et al.*, 'Influence of Pore Characteristics on Anisotropic Mechanical Behavior of Laser Powder Bed Fusion–Manufactured Metal by Micromechanical Modeling', *Adv. Eng. Mater.*, vol. 22, no. 12, p. 2000641, Dec. 2020, doi: 10.1002/adem.202000641.

[65] C. Galy, E. Le Guen, E. Lacoste, and C. Arvieu, 'Main defects observed in aluminum alloy parts produced by SLM: From causes to consequences', *Addit. Manuf.*, vol. 22, pp. 165–175, Aug. 2018, doi: 10.1016/j.addma.2018.05.005.
[66] T. Ronneberg, C. M. Davies, and P. A. Hooper, 'Revealing relationships between porosity, microstructure and mechanical properties of laser powder bed fusion 316L stainless steel through heat treatment', *Mater. Des.*, vol. 189, p. 108481, Apr. 2020, doi: 10.1016/j.matdes.2020.108481.
[67] M. Tang and P. C. Pistorius, 'Fatigue life prediction for AlSi10Mg components produced by selective laser melting', *Int. J. Fatigue*, vol. 125, pp. 479–490, Aug. 2019, doi: 10.1016/j.ijfatigue.2019.04.015.
[68] K. Solberg, S. Guan, S. M. J. Razavi, T. Welo, K. C. Chan, and F. Berto, 'Fatigue of additively manufactured 316L stainless steel: The influence of porosity and surface roughness', *Fatigue Fract. Eng. Mater. Struct.*, vol. 42, no. 9, pp. 2043–2052, 2019, doi: 10.1111/ffe.13077.
[69] P. Mercelis and J. Kruth, 'Residual stresses in selective laser sintering and selective laser melting', *Rapid Prototyp. J.*, vol. 12, no. 5, pp. 254–265, Oct. 2006, doi: 10.1108/13552540610707013.
[70] M. F. Zaeh and G. Branner, 'Investigations on residual stresses and deformations in selective laser melting', *Prod. Eng.*, vol. 4, no. 1, pp. 35–45, Feb. 2010, doi: 10.1007/s11740-009-0192-y.
[71] J. L. Bartlett and X. Li, 'An overview of residual stresses in metal powder bed fusion', *Addit. Manuf.*, vol. 27, pp. 131–149, May 2019, doi: 10.1016/j.addma.2019.02.020.
[72] C. Li, Z. Y. Liu, X. Y. Fang, and Y. B. Guo, 'Residual Stress in Metal Additive Manufacturing', *Procedia CIRP*, vol. 71, pp. 348–353, 2018, doi: 10.1016/j.procir.2018.05.039.
[73] F42 Committee, 'Guide for Evaluating Mechanical Properties of Metal Materials Made via Additive Manufacturing Processes', ASTM International. doi: 10.1520/F3122-14.
[74] H. Choo *et al.*, 'Effect of laser power on defect, texture, and microstructure of a laser powder bed fusion processed 316L stainless steel', *Mater. Des.*, vol. 164, p. 107534, Feb. 2019, doi: 10.1016/j.matdes.2018.12.006.
[75] J. S. Weaver and I. Rosenthal, 'Understanding Anisotropic Tensile Properties of Laser Powder Bed Fusion Additive Metals: A Detailed Review of Select Examples', National Institute of Standards and Technology, Nov. 2021. doi: 10.6028/NIST.AMS.100-44.
[76] S. J. Findlay and N. D. Harrison, 'Why aircraft fail', *Mater. Today*, vol. 5, no. 11, pp. 18–25, Nov. 2002, doi: 10.1016/S1369-7021(02)01138-0.
[77] G. S. Campbell and R. Lahey, 'A survey of serious aircraft accidents involving fatigue fracture', *Int. J. Fatigue*, vol. 6, no. 1, pp. 25–30, Jan. 1984, doi: 10.1016/0142-1123(84)90005-7.
[78] W. D. Callister and D. G. Rethwisch, 'Materials Science and Engineering: An Introduction, John Wiley & Sons', *Inc N. Y. NY USA*, 2007.
[79] N. W. Sachs, 'Understanding the surface features of fatigue fractures: How they describe the failure cause and the failure history', *J. Fail. Anal. Prev.*, vol. 5, no. 2, pp. 11–15, Apr. 2005, doi: 10.1361/15477020522924.
[80] G. Nicoletto, 'Directional and notch effects on the fatigue behavior of as-built DMLS Ti6Al4V', *Int. J. Fatigue*, vol. 106, pp. 124–131, Jan. 2018, doi: 10.1016/j.ijfatigue.2017.10.004.
[81] G. Nicoletto, 'Anisotropic high cycle fatigue behavior of Ti–6Al–4V obtained by powder bed laser fusion', *Int. J. Fatigue*, vol. 94, pp. 255–262, Jan. 2017, doi: 10.1016/j.ijfatigue.2016.04.032.

[82] K. Solberg, E. W. Hovig, K. Sørby, and F. Berto, 'Directional fatigue behaviour of maraging steel grade 300 produced by laser powder bed fusion', *Int. J. Fatigue*, vol. 149, p. 106229, Aug. 2021, doi: 10.1016/j.ijfatigue.2021.106229.
[83] A. Yadollahi, M. J. Mahtabi, A. Khalili, H. R. Doude, and J. C. Newman, 'Fatigue life prediction of additively manufactured material: Effects of surface roughness, defect size, and shape', *Fatigue Fract. Eng. Mater. Struct.*, vol. 41, no. 7, pp. 1602–1614, Jul. 2018, doi: 10.1111/ffe.12799.
[84] S. Lee, J. W. Pegues, and N. Shamsaei, 'Fatigue behavior and modeling for additive manufactured 304L stainless steel: The effect of surface roughness', *Int. J. Fatigue*, vol. 141, p. 105856, Dec. 2020, doi: 10.1016/j.ijfatigue.2020.105856.
[85] A. du Plessis and S. Beretta, 'Killer notches: The effect of as-built surface roughness on fatigue failure in AlSi10Mg produced by laser powder bed fusion', *Addit. Manuf.*, vol. 35, p. 101424, Oct. 2020, doi: 10.1016/j.addma.2020.101424.
[86] D. Wells and K. Morgan, 'Overview of Fatigue and Damage Tolerance Performance of SLM Alloy 718', p. 50.
[87] S. Beretta *et al.*, 'A benchmark activity on the fatigue life assessment of AlSi10Mg components manufactured by L-PBF', *Mater. Des.*, vol. 218, p. 110713, Jun. 2022, doi: 10.1016/j.matdes.2022.110713.
[88] C.-H. Chuang, S. Chen, R.-J. Yang, and P. Vogiatzis, 'Topology optimization with additive manufacturing consideration for vehicle load path development', *Int. J. Numer. Methods Eng.*, vol. 113, no. 8, pp. 1434–1445, 2018, doi: 10.1002/nme.5549.
[89] D. Walton and H. Moztarzadeh, 'Design and Development of an Additive Manufactured Component by Topology Optimisation', *Procedia CIRP*, vol. 60, pp. 205–210, Jan. 2017, doi: 10.1016/j.procir.2017.03.027.
[90] A. Dagkolu, I. Gokdag, and O. Yilmaz, 'Design and additive manufacturing of a fatigue-critical aerospace part using topology optimization and L-PBF process', *Procedia Manuf.*, vol. 54, pp. 238–243, 2021, doi: 10.1016/j.promfg.2021.07.037.
[91] A. Gupta, C. J. Bennett, and W. Sun, 'An experimental investigation on the progressive failure of an additively manufactured Laser Powder Bed Fusion Ti-6Al-4V aero-engine bracket under Low Cycle Fatigue', *Eng. Fail. Anal.*, vol. 139, p. 106455, Sep. 2022, doi: 10.1016/j.engfailanal.2022.106455.
[92] S. Cecchel, D. Ferrario, F. Mega, and G. Cornacchia, 'Numerical, Mechanical, and Metallurgical Investigation of an Innovative Near Net Shape Titanium Selective Laser Melting Engine Component and Comparison with the Conventional Forged One', *Adv. Eng. Mater.*, vol. 23, no. 7, p. 2100036, Jul. 2021, doi: 10.1002/adem.202100036.
[93] S. Cecchel *et al.*, 'Fatigue testing and end of life investigation of a topology optimized connecting rod fabricated via selective laser melting', *Int. J. Fatigue*, vol. 164, p. 107134, Nov. 2022, doi: 10.1016/j.ijfatigue.2022.107134.
[94] T. Markovits and B. Szederkényi, 'Investigation of generative design for powder bed fusion technology in case of Formula Student race car components using Ti6Al4V alloy', *J. Manuf. Process.*, vol. 80, pp. 220–231, Aug. 2022, doi: 10.1016/j.jmapro.2022.05.058.
[95] M. Arena, P. Ambrogiani, V. Raiola, F. Bocchetto, T. Tirelli, and M. Castaldo, 'Design and Qualification of an Additively Manufactured Manifold for Aircraft Landing Gears Applications', *Aerospace*, vol. 10, no. 1, p. 69, Jan. 2023, doi: 10.3390/aerospace10010069.
[96] C. Grosjean, M. Marzin, E. Camus, M. Robert, and T. Munch, 'Static and fatigue behavior of hydraulic components produced by different additive manufacturing processes', *Procedia Struct. Integr.*, vol. 38, pp. 94–108, 2022, doi: 10.1016/j.prostr.2022.03.011.
[97] F. Uriati, L. Zambrelli, G. Nicoletto, and M. Garibaldi, 'Design, production, and fatigue testing of an optimized structural component made of L-PBF AlSi10Mg', *Procedia Struct. Integr.*, vol. 34, pp. 184–190, 2021, doi: 10.1016/j.prostr.2021.12.027.

[98] G. Nicoletto, E. Riva, and F. uriati, 'Lightweight Design and Additive Manufacturing of a Fatigue-Critical Automotive Component', presented at the CO2 Reduction for Transportation Systems Conference, Jun. 2022, pp. 2022-37–0026. doi: 10.4271/2022-37-0026.
[99] K. Kempen, L. Thijs, J. Van Humbeeck, and J.-P. Kruth, 'Mechanical Properties of AlSi10Mg Produced by Selective Laser Melting', *Phys. Procedia*, vol. 39, pp. 439–446, Jan. 2012, doi: 10.1016/j.phpro.2012.10.059.
[100] F. Trevisan *et al.*, 'On the Selective Laser Melting (SLM) of the AlSi10Mg Alloy: Process, Microstructure, and Mechanical Properties', *Materials*, vol. 10, no. 1, Art. no. 1, Jan. 2017, doi: 10.3390/ma10010076.
[101] O. Diegel, A. Nordin, and D. Motte, 'Computational Tools for Design Analysis and Optimisation of AM Parts', in *A Practical Guide to Design for Additive Manufacturing*, O. Diegel, A. Nordin, and D. Motte, Eds. Singapore: Springer, 2019, pp. 71–77. doi: 10.1007/978-981-13-8281-9_4.
[102] M. P. Bendsøe and O. Sigmund, *Topology optimization: theory, methods, and applications*. Berlin ; New York: Springer, 2003.
[103] M. P. Bendsøe, 'Optimal shape design as a material distribution problem', *Struct. Optim.*, vol. 1, no. 4, pp. 193–202, Dec. 1989, doi: 10.1007/BF01650949.
[104] N. Keller and V. Ploshikhin, *New Method for fast predictions of residual stress and distortion of AM parts*. 2014.
[105] J.-U. Park, G. An, W. C. Woo, J. Choi, and N. Ma, 'Residual stress measurement in an extra thick multi-pass weld using initial stress integrated inherent strain method', *Mar. Struct.*, vol. 39, pp. 424–437, Dec. 2014, doi: 10.1016/j.marstruc.2014.10.002.
[106] S. Beretta, M. Gargourimotlagh, S. Foletti, A. du Plessis, and M. Riccio, 'Fatigue strength assessment of "as built" AlSi10Mg manufactured by SLM with different build orientations', *Int. J. Fatigue*, vol. 139, p. 105737, Oct. 2020, doi: 10.1016/j.ijfatigue.2020.105737.
[107] P. Li, D. H. Warner, and N. Phan, 'Predicting the fatigue performance of an additively manufactured Ti-6Al-4V component from witness coupon behavior', *Addit. Manuf.*, vol. 35, p. 101230, Oct. 2020, doi: 10.1016/j.addma.2020.101230.
[108] G. Nicoletto, 'An Efficient Test Method for the Quantification of Technology-Dependent Factors Affecting the Fatigue Behavior of Metallic Additive Manufacturing Components', in *Structural Integrity of Additive Manufactured Parts*, N. Shamsaei, S. Daniewicz, N. Hrabe, S. Beretta, J. Waller, and M. Seifi, Eds. 100 Barr Harbor Drive, PO Box C700, West Conshohocken, PA 19428-2959: ASTM International, 2020, pp. 484–506. doi: 10.1520/STP162020180081.
[109] G. Nicoletto, 'Efficient determination of influence factors in fatigue of additive manufactured metals', *Procedia Struct. Integr.*, vol. 8, pp. 184–191, Jan. 2018, doi: 10.1016/j.prostr.2017.12.020.
[110] 'ISO 6508-1:2016 - Metallic materials — Rockwell hardness test — Part 1: Test method'. [Online]. Available: . https://www.iso.org/standard/70460.html.
[111] 'ISO - ISO 4287:1997 - Geometrical Product Specifications (GPS) — Surface texture: Profile method — Terms, definitions and surface texture parameters'. [Online]. Available: https://www.iso.org/standard/10132.html.
[112] P. T. Summers *et al.*, 'Overview of aluminum alloy mechanical properties during and after fires', *Fire Sci. Rev.*, vol. 4, no. 1, p. 3, Dec. 2015, doi: 10.1186/s40038-015-0007-5.
[113] M.-N. Su and B. Young, 'Material properties of normal and high strength aluminium alloys at elevated temperatures', *Thin-Walled Struct.*, vol. 137, pp. 463–471, Apr. 2019, doi: 10.1016/j.tws.2019.01.012.
[114] S. Bagherifard, N. Beretta, S. Monti, M. Riccio, M. Bandini, and M. Guagliano, 'On the fatigue strength enhancement of additive manufactured AlSi10Mg parts by mechanical and

thermal post-processing', *Mater. Des.*, vol. 145, pp. 28–41, May 2018, doi: 10.1016/j.matdes.2018.02.055.
[115] A. Salmi and E. Atzeni, 'Residual stress analysis of thin AlSi10Mg parts produced by Laser Powder Bed Fusion', *Virtual Phys. Prototyp.*, vol. 15, no. 1, pp. 49–61, Jan. 2020, doi: 10.1080/17452759.2019.1650237.
[116] G. S. Schajer and P. S. Whitehead, *Hole-Drilling Method for Measuring Residual Stresses*. Cham: Springer International Publishing, 2018. doi: 10.1007/978-3-031-79713-2.
[117] M. V. Gerov, E. Yu. Vladislavskaya, V. F. Terent'ev, D. V. Prosvirnin, O. S. Antonova, and A. G. Kolmakov, 'Fatigue Strength of an AlSi10Mg Alloy Fabricated by Selective Laser Melting', *Russ. Metall. Met.*, vol. 2019, no. 4, pp. 392–397, Apr. 2019, doi: 10.1134/S0036029519040098.
[118] G. Nicoletto, L. Gallina, and E. Riva, 'Influence of as-built surfaces on the fatigue behavior of AlSi10Mg parts obtained by laser powder bed fusion', *Procedia Struct. Integr.*, vol. 24, pp. 381–389, 2019, doi: 10.1016/j.prostr.2020.02.035.
[119] N. T. Aboulkhair, I. Maskery, C. Tuck, I. Ashcroft, and N. M. Everitt, 'Improving the fatigue behaviour of a selectively laser melted aluminium alloy: Influence of heat treatment and surface quality', *Mater. Des.*, vol. 104, pp. 174–182, Aug. 2016, doi: 10.1016/j.matdes.2016.05.041.
[120] G. P. Sendeckyj, 'Constant life diagrams — a historical review', *Int. J. Fatigue*, vol. 23, no. 4, pp. 347–353, Apr. 2001, doi: 10.1016/S0142-1123(00)00077-3.

List of Figures

Figure 1- Additive manufacturing-related patent application in the period time from 2000 to 2018 – Source European Patent Office 22

Figure 2 - Seven distinct categories of additive manufacturing technology acknowledged by ISO/ASTM standards (ISO/ASTM 52900) 23

Figure 3 – a) AMOS-17 command horn antenna BOEING; b) GE Aviation additively-produced fuel nozzle tips for the LEAP engine 25

Figure 4 –a) Bugatti 3D-printed brake caliper; b) view inside the engine bay of Czinger 21C. 26

Figure 5 –Pinarello's Bolide F HR 3D features an additively manufactured Scalmalloy frame 27

Figure 6 - Interaction between the source of energy and the powder material in the L-PBF process 28

Figure 7 – Four main factors that are responsible for the final quality of an L-PBF part and related properties 28

Figure 8 – L-PBF process: laser-material interaction and representation of a L-PBF fabrication system 29

Figure 9- Example of a qualitative representation of optimal processing map and list of undesirable printed features and defects 30

Figure 10 – View of surfaces after support removal according to different methods: a) reference condition due to manual support removal; b) support removal by jet-blasting; c)support removal by the electrochemical process 32

Figure 11 – a) Specimen orientation and denomination; b) Surface morphology and near-surface microstructure obtained observed on IN718 samples (the black arrows indicated the build direction) [48] 35

Figure 12-Different areas of the samples microsection shows peculiar feature caused by the specific orientation and build direction and the selected process parameters [61]. 36

Figure 13 – a) Microstructure of the L-PBF-densified sample showing pores in a view perpendicular to the build-up direction. [64], b) Annotated as-built material microstructure images [66] 37

Figure 14 - Effect of surface finishing on fatigue behavior L-PBF metals. a) Improvement of the fatigue strength of AlSi10Mg after machining [87]; b) Detrimental effect of as built L-PBF surface morphology on fatigue behavior of IN718[86]..... 41
Figure 15 - Workflow for design, production and qualification of an L-PBF component 48
Figure 16 – L-PBF Fabrication systems at the production plant of the company Beamit – Rubbiano (PR) Italy 49
Figure 17 – a) Configuration of the suspension lower control arm b) Example of the actual component with a connection point and bushings..... 50
Figure 18 – Geometry of the control arm after defeaturing, simplification of the constraints and geometrical resizing..... 53
Figure 19 – a) Size optimization, b) shape optimization c) Topology Optimization..... 54
Figure 20 – a) suspension arm with description of DS (red) and NDS (grey) prior to topology optimization using Inspire; b) suspension arm after topology optimization and reconstruction using Inspire Studio..... 55
Figure 21 – Build Job representation from Materialise Magics software interface 57
Figure 22 -a) Amphion process simulation software calibration specimen; b) Method of measuring the deflection of a calibration specimen 58
Figure 23 – Experimental test configurations (TC) of an optimized part. a) TC1 – cyclic 3-point-bending; b) TC2 - cyclic tensile load; c) TC3 – Cyclic tensile load with local contact 63
Figure 24 - a) Overall dimension of the miniature sample; b) cyclic plane bending testing of the miniature sample; c) Comparison between the mini-specimen and the standard hourglass specimens used for push-pull tests during experimental activities at ESA 65
Figure 25 - Elastic stress distribution in the miniature specimen under plane bending; a) FEA contour plot with indication of fatigue crack initiation location; b) distribution of the normalized stress along the minimum cross-section..... 66
Figure 26 – Miniature samples fabrication for determining the reference material properties of L-PBF AlSi10Mg..... 67
Figure 27 - Von-Mises stress under an applied load equal to 5000N 72
Figure 28- The topology optimization solutions show the design space and optimized redistributed volume, with the goal of maximizing stiffness. a) Configuration A – no symmetry; b) Configuration B – symmetry XY; c) Configuration C, symmetry XY, XZ. 73
Figure 29 – Final topology optimization solution remodeled using PolyNURBS..... 74
Figure 30 – Three component orientations evaluated during the process preparation to select the best configuration to minimize deformation during the process 76

Figure 31 – a) Orientation of the miniature witness samples produced along with the components in the build job. The black arrow represents the build direction; b) Miniature samples fabrication for determining the reference material properties of L-PBF AlSi10Mg 77

Figure 32 - Build job showing optimized suspension arms, miniature specimens, and software calibration specimens after fabrication and prior to separation from the build platform and support removal 79

Figure 33 – Views of the suspension arms printed according to the two orientations with respect to building direction also show the different distributions of supports.; a)orientation A; b)orientation B 79

Figure 34 – Flat surface of the miniature samples manufactured alongside the components to characterize the fatigue performance of the material 80

Figure 35 – Cantilever calibration sample manufactured to evaluate the deflection induced by the process after removal from the build plate and for the calibration simulation software .. 81

Figure 36 – Surface Hardness distribution along the length of the optimized arm in relation to the build direction. 83

Figure 37 – Hardness measurement location on the optimized sample 84

Figure 38 – Optimized bracket with the indication of the area where linear profile roughness was collected 84

Figure 39 - Optimized component prepared for fatigue testing with nylon bushing positioned inside the part..... 86

Figure 40 – First testing configuration: three-point bending. a) numerical simulation model with the definition of load and constraints; b) experimental setup for TC1 87

Figure 41 – Contour plot of the principal stress distribution for testing configuration 1 (TC1) the critical point in position M. a) contour plot of the tested components; b) detail of the contour plot with identification peak stress point. 87

Figure 42 – Second testing configuration with vertical tensile loading. a) numerical simulation model with the definition of load and constraints; b) experimental setup for TC2 ... 88

Figure 43 – Contour plot of the principal stress distribution for testing configuration 2. (TC2). The critical points are in positions S1 (a – b) and S2 (c-d). 89

Figure 44 - Third testing configuration with vertical tensile loading and contact between the component and the steel pin. a) numerical simulation model with the definition of load and constraints; b) experimental setup for TC3 89

Figure 45 - Contour plot of the principal stress distribution for testing configuration 3. (TC2). The critical points are in position U with distribution peak stress values on the external side (a – b) and on the internal side (c-d), but with limited differences. 90

Figure 46 – Optimized arm with the indication of the higher stressed point for each loading configuration and where the failure occurred..... 91

Figure 47 - Fatigue behavior of A and B components on the different testing configurations. 92

Figure 48- Component A1 tested at TC1 and identification of the failure location at M critical point and fracture surface..... 94

Figure 49 - Components tested at TC2, identification of the failure location, and optical observation of the fracture surface. a)Component A1 with failure location at S1 critical point; b)Component B1 with failure location at S2 critical point 94

Figure 50 - Component B1 tested at TC3 and identification of the failure location at U critical point and fracture surface..... 95

Figure 51 –Displacement of the components after production; a) Orientation A; b) Orientation B..... 96

Figure 52- Residual stress distribution evaluated on optimized component using process simulation software Amphion. The stress direction reported in the contour plot is Z parallel to the build direction. 98

Figure 53 - Fatigue behavior of as-built AlSi10Mg samples produced with SLM500, Nominal layer thickness 50µm. 102

Figure 54 – a) direction of the miniature samples evaluated for residual stress calculation with process simulation and the direction of evaluated stress indicated with red arrow..... 103

Figure 55 – Contour plot of the residual stress distribution evaluated using the software simulation software AMPHYON. a) A; b) B, c) C. 104

Figure 56 – Residual stress distribution on cross section of the miniature samples, the dashed line indicates the top surface line where the residual stress was evaluated for each orientation. 104

Figure 57 - AlSi10Mg fatigue test comparison performed on as-built samples R=0,1 .. 107

Figure 58 – Integrated design workflow for design, produce, and testing of L-PBF components. 108

Figure 59 – Integrated procedure for the design of structural L-PBF part from reference fatigue properties..... 115

Figure 60 - Experimental fatigue behavior of directional miniatures specimens and optimized parts made of L-PBF AlSi10Mg 116

Figure 61- Fatigue strength of miniature samples in converted fully reverse loading condition considering the effect of residual stress. 118

Figure 62 - Fatigue strength of A and B components after considering the effect of residual stress. 122

Figure 63 – S-N plot comparing the fatigue strength of components and vertical miniature sample at full reverse loading condition..... 123

Figure 64 – Components comparison between experimental values and estimated values forecasted from fatigue vertical miniature samples. 124

List of Tables

Table 1 - AlSi10Mg material composition 51
Table 2 – Technical specification of SLM500 60
Table 3 - Process parameters for the realization of components and specimens 60
Table 4 – Material properties of Aluminum alloy selected to perform the numerical simulation. 71
Table 5 – Results of the topology optimization of the suspension arm with different symmetry conditions with the goal of maximizing stiffness. 74
Table 6 – Result of the preliminary simulation to select the best building direction using Amphion simulation software 76
Table 7 – Summary of the number of parts and samples produced in the build job. 78
Table 8 - Mechanical properties of AlSi10Mg after direct aging heat treatment (Beamit AlSi10Mg datasheet) 78
Table 9 – Linear surface roughness parameters measured on the parts. 85
Table 10 – Position of the peak stress related to the relative testing configuration and principal stress value determined by an applied load of 3000N evaluated with FEA 91
Table 11 - S-N power law coefficients and exponents experimental fatigue strength at 2 10^6 cycles 92
Table 12 – Summary of the fatigue test performed on the optimized component at R=0,1 93
Table 13 – Residual stress distribution on critical location for Component A and B evaluated from process simulation. 97
Table 14 - Roughness measurements on differently oriented surfaces and an indication of the direction of measurement(a) 100
Table 15 – Hardness measurement position and results. 101
Table 16 - S-N power law coefficients and exponents. Fatigue strength at 2 10^6 cycles is estimated for different specimen orientations. 102
Table 17 – Reference residual stress values measured on the top profile of the cross-sectional area of the fatigue miniature sample 105
Table 18 – Representative properties of AlSi10Mg miniature samples 116
Table 19 - S-N power law coefficients and exponents and fatigue strength at 2 10^6 cycles is estimated for different specimen orientations in the condition of fully reverse loading. 119

Table 20 – Fatigue test results of the directional miniature specimens corrected for the presence of residual stresses..... 120
Table 21 – Nominal and effective experimental results of fatigue test on L-PBF components and local residual stresses 121
Table 22 - S-N power law coefficients and exponents for components fatigue behavior at full reverse loading..... 122